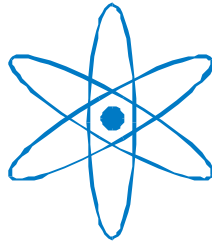


PHYSIK-DEPARTMENT



**Photovoltage phenomena
in nanoscale materials**

Dissertation
von

Volodymyr Duzhko



TECHNISCHE UNIVERSITÄT
MÜNCHEN

Technische Universität München
Fakultät für Physik E16

Photovoltage phenomena in nanoscale materials

Volodymyr Duzhko

Vollständiger Abdruck der von der Fakultät für Physik der Technischen
Universität München zur Erlangung des akademischen Grades eines

Doktors der Naturwissenschaften (Dr.rer.nat.)

genehmigten Dissertation.

Vorsitzender: Univ.- Prof. Dr. M. Stutzmann

Prüfer der Dissertation: 1. Univ.- Prof. F. Koch, Ph.D.

2. Univ.- Prof. Dr. M. Kleber

Die Dissertation wurde am 7.05.2002 bei der Technischen Universität München eingereicht
und durch die Fakultät für Physik am 24.06.2002 angenommen.

*Разумные люди приспосабливаются к окружающему миру.
Неразумные люди приспосабливают мир к себе.
Вот почему прогресс определяется действиями неразумных людей.*

Джордж Бернард Шоу

моїм батькам

angefertigt September 1999 – April 2002

am Physik Department E16 (Prof. F. Koch, Ph.D.)

Technische Universität München

85747 Garching b. München, Deutschland

Table of Contents

Introduction	1
CHAPTER 1 Concepts of spatial separation of light induced charge carriers	6
1.1 Introduction	6
1.2 Charge carrier separation in the electric field of the surface space charge region	10
1.2.1 General consideration	10
1.2.2 Inter-band gap illumination	11
1.2.3 Sub-band gap illumination	17
1.3 Diffusion of light induced charge carriers	22
1.3.1 General case	22
1.3.2 Dember effect, steady-state case	25
1.3.3 Maxwell relaxation time	27
1.3.4 Diffusion photovoltage model, non-steady state case	28
1.4 Model of photovoltage in thin metal oxide layers with trap states	33
1.4.1 Photovoltage in thin films, heterostructures, superlattices	33
1.4.2 Formation of the photovoltage at metal oxide/metal interfaces	34
1.4.3 Role of tunneling for the photovoltage decay	36
1.4.4 Role of thermal emission for the photovoltage decay	39
CHAPTER 2 Experimental methods and materials	41
2.1 Experimental methods	41
2.1.1 Principle of photovoltage measurements	42
2.1.2 Equivalent circuit of the photovoltage cell	43
2.1.3 Voltage response measurements	44
2.1.4 Chopped signal control	45
2.1.5 Vacuum and gas ambience, control of temperature	47
2.1.6 Subsidiary methods	49
2.2 Nanoscale materials	50
2.2.1 Porous Silicon	50
2.2.2 Poly(p-phenylene vinylene)	51
2.2.3 Metal oxide layers (TiO ₂ , Cu ₂ O, ZnO)	52
2.2.4 Sintered porous TiO ₂ layers	53
2.2.5 Geometry of the samples	55

CHAPTER 3 Drift and diffusion of light induced charge carriers in porous silicon	58
3.1 Separation of charge carriers in the electric field of the surface space charge region	61
3.2 Surface potential and free carrier concentration in mesoporous Si	62
3.3 Oxidation and surface states	65
3.4 Role of characteristic dimensions of the nanoparticles	70
3.5 Role of the Maxwell (dielectric) relaxation time for the charge carrier separation	73
3.6 Conclusion of chapter 3	76
CHAPTER 4 Diffusion photovoltage in poly(p-phenylene vinylene) ...	78
4.1 Gradient of concentration as a driving force of photovoltage in a thick film	81
4.2 Role of the PPV/ITO interface in thin film	82
4.3 Dependence of the spectral photovoltage on the layer thickness ...	85
4.4 Estimation of the diffusion coefficients	85
4.5 Dependence of the diffusion photovoltage on bias illumination	88
4.6 Thermal activation of the diffusion photovoltage	89
4.7 Conclusion of chapter 4	91
CHAPTER 5 Trap-limited photovoltage in ultrathin metal oxide layers	93
5.1 Formation of the photovoltage	95
5.1.1 Preferential trapping of electrons or holes	95
5.1.2 Limitation of the photovoltage amplitude	97
5.1.3 States in the forbidden gap	99
5.2 Relaxation of the photovoltage	101
5.2.1 Recombination of spatially separated charge carriers	101
5.2.2 Role of thermal emission at higher temperatures	102
5.3 Electron traps in ultrathin TiO ₂ layers	105
5.4 Transition from the trap-limited photovoltage to diffusion photovoltage	106
5.5 Conclusion of chapter 5	108

CHAPTER 6 Photovoltage in porous TiO₂	110
6.1 Transient photovoltage in well-passivated porous TiO ₂	113
6.2 Spectral photovoltage in well-passivated porous TiO ₂	115
6.3 Formation of gap states in vacuum	118
6.4 Screening of gap states by water	122
6.5 Transient photovoltage in porous TiO ₂ with gap states	124
6.6 Nature of the photovoltage maximum	126
6.7 Conclusion of chapter 6	128
SUMMARY	130
Appendix A	134
References	136
Acknowledgements	143
Curriculum Vitae	144
List of publications in refereed journals	145
Conference participations	146

Introduction

Among the problems of modern physics two challenges to the semiconductor physics can be emphasized. The first one is related to the continuous miniaturization of the operational scale of semiconductor devices and the second one to the development of low-cost energy sources. The amount of stored information, the access time and the velocity of its transmission determine the level of modern information society. The improvement of these characteristics requires a decrease in the characteristic dimensions of devices. The nanometer scale is the state-of-the-art of modern semiconductor technology. New physical phenomena which appear on this scale are of essential fundamental interest. Semiconductor solar cells are efficient solar energy converters. However, their efficiency is already close to the theoretical limit and minor additional improvements of their characteristics demands an enormous increase of technological expense.

The wide range of novel solar energy converters with unique properties is based on the physical ideas on the nanometer scale as well as on the use of novel materials. Among novel photonic devices one can select, for example, organic light-emitting diodes ¹ or dye-sensitized solar cells.² They are based on materials, like the organic polymer poly(p-phenylene vinylene) (PPV), porous Si, or porous TiO₂. The extremely high radiative recombination efficiency of organic materials is combined with the poor transport properties of disordered polymer

2 Introduction

chains in the organic light emitting diodes.³ The surface-to-volume ratio increases with decreasing size of nanoparticles in the porous materials. The huge surface area of a porous matrix⁴ enlarges the illumination area and, therefore, the efficiency of dye-sensitized solar cells.² At the same time, the propagation of charge carriers through the porous matrix is the limiting factor for their performance. In order to improve the efficiency of the devices, one has to understand transport properties of the materials which contain characteristic structural units in the nanometer range.

A high localization of the mean free path of charge carriers via scattering on the intrinsic defects or grain boundaries takes place in disordered nanoporous materials.⁵ The decrease of the uncertainty of the carrier position (time) leads to the increase of the uncertainty of the momentum (energy). For example, the energy uncertainty (DE) is 0.1 eV for a charge carrier mobility (m) of 0.1 cm²/Vs (if using $m = et/m_0$ and $DE \approx \hbar/2p$, where t , e , m_0 and h are the average scattering time, elementary charge, mass of the free electron and Planck constant, respectively). The value of m is of the order of 10⁻⁶ cm²/Vs in porous TiO₂,⁶ ranges between 10⁻¹ and 10⁻³ cm²/Vs in porous Si depending on the porosity,⁷ and 10⁻⁵ cm²/Vs in PPV,³ which is several orders of magnitude smaller than is used for the estimation above. The modification of electronic properties due to spatial confinement of the electron wave function is well known for conventional semiconductor nanostructures (quantum confinement effect).⁸ The modified electronic properties change the transport properties of nanoscale materials in comparison to the bulk precursors.

The huge surface area of some nanoscale materials is the other specific feature which determines the transport properties. Even for large crystals, the trapping of charge carriers on the surface states which are situated within a few monolayers in the vicinity of the surface changes the electronic properties of the much thicker surface space charge region in comparison to the remaining bulk. The role of the surface states is dramatic for porous materials due to the large surface area and huge surface-to-volume ratio.⁴

Additionally, the transport properties within one nanoparticle (*intra-particle transport*) and between the nanoparticles (*inter-particle transport*) differ dramatically due to, for example, the energy barriers between the nanoparticles or absence of far order in the network of the polymer chains and porous materials.

A photovoltage (PV) arises whenever light induced excess charge carriers are separated in space. Therefore, the formation of a PV signal is determined by the fundamental properties of light absorption and transport of excess carriers in a semiconducting material. The photovoltage techniques were numerous used for the investigation of crystalline semiconductors.⁹ The value of surface potential,¹⁰ lifetime¹¹ and diffusion length¹² of minority carriers, parameters of surface states (energy position, density, occupancy, capture cross-section for electrons and photons),¹³⁻¹⁷ etc. were determined from the transient and spectral PV measurements.

The contactless approach is the main advantage of the photovoltage technique for the investigation of transport properties of porous materials. For example, the electrical conductivity is very sensitive to the storage in air due to oxidation¹⁸ in porous Si and depends on the partial pressure of oxygen and water¹⁹ in porous TiO₂. The possibility of control the ambient under *in-situ* measurements is the crucial requirement for the investigation of transport properties for nanoporous materials. The biocompatibility of porous TiO₂ and porous Si and the comparable size of characteristic dimensions allow to combine porous semiconductors with biomolecular and biological objects and apply the PV technique to the investigation of the charge carrier generation and their spatial separation in these systems. Therefore, the PV is a promising method for interdisciplinary research.

Despite of a large amount of work devoted to the PV phenomena in crystalline semiconductors, to our best knowledge, only a few consider the PV phenomena in nanoscale materials (like quantum dots, organic polymers, porous semiconductors, etc.).⁹ The task of this thesis is the development of the interpretation methodology for the transient and spectral photovoltage techniques and its application to the investigation of transport properties and electronic states distribution in nanoscale materials.

The question about the mechanism of the PV signal formation in nanoscale materials is closely related to the ratio between absorption length of the light, width of the surface space charge region, size of nanoparticles and thickness of a sample. Three reasons can be considered for the separation of light induced charge carriers in nanoscale materials (Figure I.1): (i) macroscopic (over many nanoparticles) built-in electric field of the surface space charge region under homogeneous excess charge carrier generation;

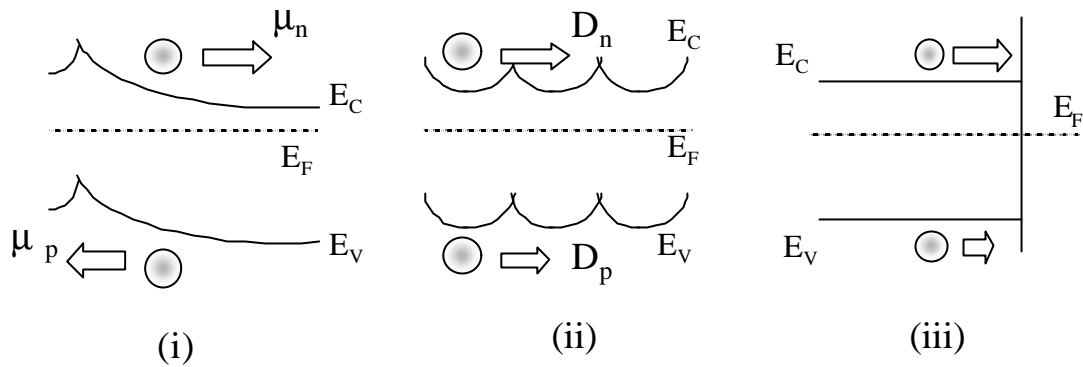


FIG.I.1 Concepts of charge carrier separation in nanoscale materials: drift in the built-in electric field (i), diffusion under concentration gradients (ii), separation at the interface (iii)

(ii) concentration gradients under non-homogeneous excess charge carriers generation or surface recombination in the case of negligible macroscopic built-in electric field; (iii) potential differences due to interfaces (contacts, grain boundaries, etc.) and internal surface states (microscopic electric field, within the nanoparticle). Chapter 1 of the following thesis describes the main theoretical concepts of the PV formation. Charge carrier separation in the built-in electric field of the surface space charge region is the typical mechanism of the PV formation in crystalline semiconductors. A review of the surface PV in crystalline semiconductors is given in the first part of Chapter 1 for inter-band gap and sub-band gap illumination. The second part of Chapter 1 describes the Demer PV for steady-state case and proposes the concept of the non-steady state case of the *diffusion PV* for materials with large *Maxwell (dielectric) relaxation time*. The specific features of the PV in thin films, buried interfaces and superlattices are discussed in the third part of Chapter 1. The model of the *trap-limited PV* in ultrathin metal oxide layers with traps is proposed.

Chapter 2 describes the experimental methods and basic properties of the samples. The principle of transient and spectral PV techniques, the equivalent circuit of the elementary cell, the equipment for the in-situ measurements with control of ambience and temperature are discussed in details. Some additional experimental techniques which were also used to get information about the size of nanoparticles, crystalline phase of the material, chemical bonds on the surface, electrical conductivity, optical transmission are also described in the Chapter 2. The similarity

and differences in the properties of the investigated *nanoscale materials* (porous Si, PPV, porous TiO₂, ultrathin TiO₂ layers) are given in this chapter as well as in the introductions to the Chapters 3 - 6.

Porous Si is known as a material where the size of nanoparticles can be easily changed in a wide range by choosing the preparation conditions. Chapter 3 shows the transition from the *surface PV* (dominating role of the electric field of the surface space charge region for the spatial separation of the light induced charge carriers) in the porous Si with nanoparticles of a large size to the *diffusion PV* (with concentration gradients as the dominating reason for the spatial separation of light induced charge carriers) in the porous Si with nanoparticles of a small size. The surface potential, free charge carrier concentration, change of the type of surface states with oxidation are discussed for porous Si. The method for the contactless determination of the conductivity is developed.

Chapter 4 shows the “pure” diffusion PV case on example of the organic polymer PPV which is characterized by a very large *Maxwell relaxation time*. The shapes of the measured and simulated by the diffusion PV model PV transients are compared. Thermal activation of the diffusion PV is shown. The method for the estimation of the diffusion coefficient of electrons and holes is developed for the materials with a large Maxwell relaxation time.

In Chapter 5, ultrathin anodic TiO₂ layers are used as a model system of a nanoparticle for investigation of the trap distribution and charge carrier separation. The model of the trap-limited PV is applied to explain the formation and relaxation of the PV in the ultrathin anodic TiO₂ layers. Recombination of the spatially separated charge carriers and thermal emission of the trapped charge carriers are discussed for the decay of the PV. The generality of the interface PV in the metal oxide layers with traps are shown on the examples of ultrathin Cu₂O and ZnO layers.

The developed concept of the diffusion PV and trap-limited PV are applied to the investigation of the transport properties and electronic state distribution in the sintered nanoporous TiO₂ layers in Chapter 6. Creation and screening of the electronic states on the surface of the nanoparticles by different ambiances (air, vacuum, oxygen, water) are shown. The kinetics of the charge carrier separation within one nanoparticle in ultrathin anodic TiO₂ layers and between nanoparticles in the sintered nanoporous TiO₂ layers are compared.

CHAPTER 1 Concepts of spatial separation of light induced charge carriers

1.1 Introduction

Transport properties of semiconductors play an important role in many applications as, for example, light emitting diodes, photodiodes and others. Spatial separation of photoinduced charge carriers leads to the formation of a photovoltage in semiconductors. Transient and spectral dependent photovoltage methods can be used as tools for the investigation of transport properties and electronic states in different materials. Several mechanisms of the spatial charge separation under illumination lead to the formation of a photovoltage. The separation of different transport mechanisms can be made on the analysis of the photovoltage transients. The typical photovoltage transients for crystalline semiconductors under short pulse illumination are shown on the examples of highly doped n-type and p-type Si in Figure 1.1. The characteristic feature of the photovoltage is the immediate appearance of the signal and the maximum within the duration of the illumination pulse. The fast formation of photovoltage in usual semiconductors is

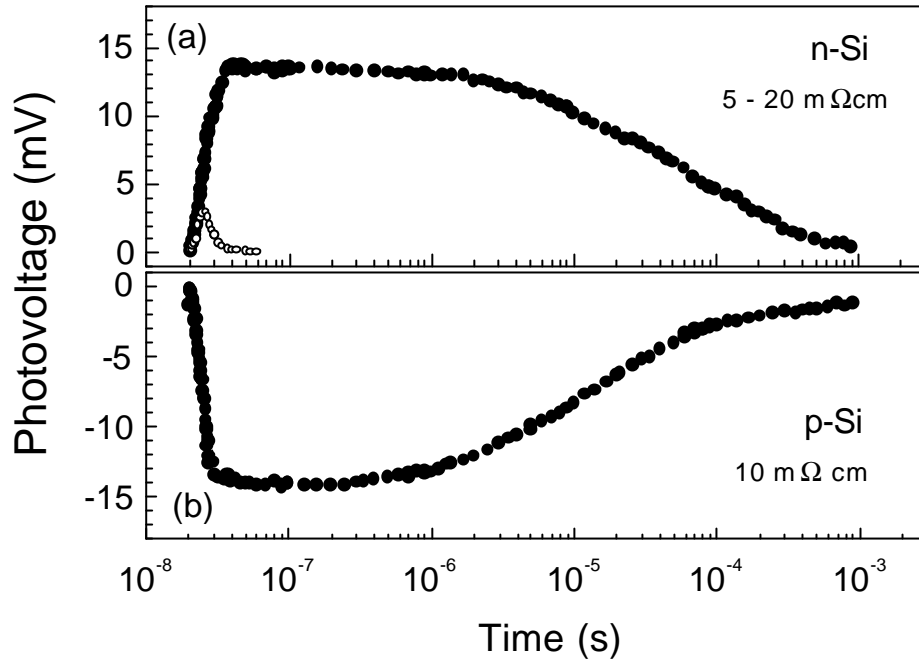


FIG.1.1: Typical photovoltage transients for n-type (a) and p-type (b) Si under short pulse illumination.

associated with the charge separation in the electric field of the surface space charge region. The non - steady state process of photovoltage formation was not observed before for this kind of photovoltage.

In the first part of this chapter we discuss the physical picture of the surface space charge region and the steady state theory of the photovoltage under CW illumination. A brief description of its applications to the investigation of surface properties of crystalline materials will be also given. In some specific cases, the slow increase of the photovoltage under sub-bandgap CW illumination is possible if the occupation of surface states changes with time. This case will be discussed separately. Usually several photovoltage phenomena act simultaneously. Despite of the fact that the photovoltage and separation of charge in the surface space charge region is determined mainly by the surface properties and contains no information about the transport properties of materials itself, we will give main features of all possible photovoltage effects related to the surface in order to make possible the separation of one mechanism from another. The first part of the chapter will serve as an introduction to the basic concepts of photovoltage phenomena in crystalline semiconductors, introduce definitions and equations for the subsequent sections.

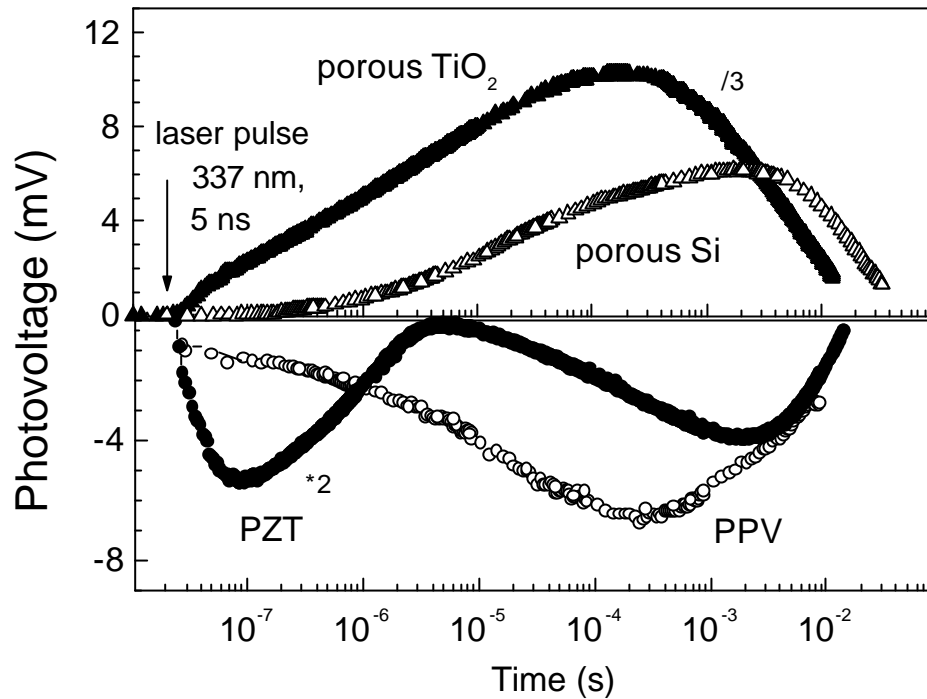


FIG.1.2: Some photovoltage transients for porous TiO_2 , porous Si, PPV and PZT* under short pulse illumination.

Different kinetics of photovoltage were recently observed by Duzhko *et al.* for a wide class of materials. Examples of photovoltage transients for porous TiO_2 , porous Si, PPV and $\text{Pb}(\text{Zr}_x\text{Ti}_{1-x}\text{O}_3)$ (PZT) are shown in Fig.1.2. These transients are characterized by the presence of a very slow retardation of the photovoltage with respect to the laser pulse. The photovoltage is almost zero or very small during the laser pulse and reaches its maximum after 5 - 6 orders of magnitude in time. The retarded transients were observed for a wide class of materials with different properties, which shows the generality of the phenomenon of retarded photovoltage. Such kinetics of photovoltage implement a minor role of the electric field for charge separation. In the second part of this chapter we will concentrate on the retarded transient photovoltage and discuss the specific features of these materials which determine the photovoltage in these materials. The diffusion of charge carriers with different diffusion coefficients will be proposed as the dominant process of charge carrier separation and the model of diffusion photovoltage will be proposed for the explanation of experimental data in a wide class of nanoscale materials. The difference and similarity to the well known Dember effect will be discussed.

*for PZT: B. Li, Th. Dittrich, F. Koch, unpublished data

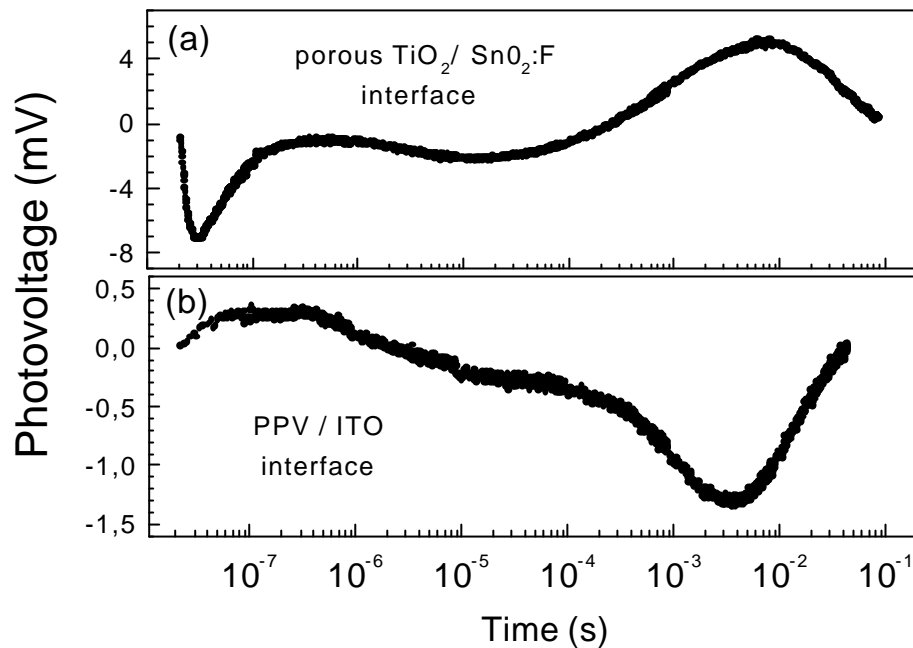


FIG.1.3: Typical photovoltage transients for porous $\text{TiO}_2/\text{SnO}_2:\text{F}$ and PPV/ITO interfaces under short pulse illumination.

Nanoscale materials contain basic spatial elements with typical dimensions in the nanometer scale. The transport properties of these materials depend on the intra - and inter- particle transport. In some specific cases, which will be discussed later, ultrathin layers can serve as a model of a nano-unit of the materials. The properties of the interface with the substrate play an important role for charge separation in such systems and separation of one from another is important. Examples of typical photovoltage transients for $\text{TiO}_2/\text{SnO}_2:\text{F}$ and PPV/ITO interfaces are shown in Fig.1.3. The situation becomes more complicated when the interface and bulk properties are involved. Fast components of photovoltage as well as retarded one are present in these pictures and the photovoltage can change the sign with time. This shows that bulk properties as well as separation of charge carriers at the interface are involved in these cases. In the third part of the chapter we discuss separation of charge on the nanoscale and propose a model of the trap-limited photovoltage for the semiconductor/metal interface. We will also give a brief review of interface phenomena in bulk semiconductors, describe specific features of photovoltage in the thin films, buried interfaces, and superlattices.

1.2 Separation of light induced charge carriers in the electric field of surface space charge region

The question about the mechanism of the PV formation in nanoscale materials is closely related to the ratio between absorption length of the light, width of the surface space charge region, size of nanoparticles and thickness of a sample. In nanoparticles of a large size (condition will be introduced later), an essential built-in electric field can exist due to the trapped charge at the geometrical surface or at the internal surface. The drift of light induced charge carriers will lead to the formation of the PV signal. This case is similar to the crystalline material where the electric field of the surface space charge region (SCR) is the main reason for the spatial separation of charge carriers under homogeneous excess charge carrier distribution. We will briefly discuss this mechanism of the PV formation (surface PV, SPV) related to the surface SCR.

1.2.1 General consideration

The periodic structure of an ideal crystalline semiconductor results in the appearance of allowed energy bands separated by the forbidden gap (bandgap). Termination of ideal periodic structure at the surface as well as dangling bonds, surface reconstruction or relaxation, point and plane defects, adsorbed impurities can form localized states in the forbidden energy gap. Let us consider, for example, the surface of a p-type semiconductor (Figure 1.4). Holes from the valence band tend to fill up the surface states above the Fermi-level in order to establish thermal equilibrium. While the positive charge on the surface states Q_{SS} is supplied by the underlying bulk, the non-equilibrium negative charge Q_{SCR} is formed within the near-surface volume, which is defined as the surface SCR. The charge conservation rule is:

$$Q_{SS} = - Q_{SCR} \quad (1.2.1)$$

The result of the charge separation will be an electric field to oppose the further flow of more holes into the surface states. The energy of the surface is descended with respect to its bulk value, as shown in Fig.1.4. If the amount, by which the conduction and valence bands are descended at the surface, is denoted by $e\mathbf{j}_s$, then \mathbf{j}_s is called the *surface potential*. By definition \mathbf{j}_s is positive when the bands are bent downward.

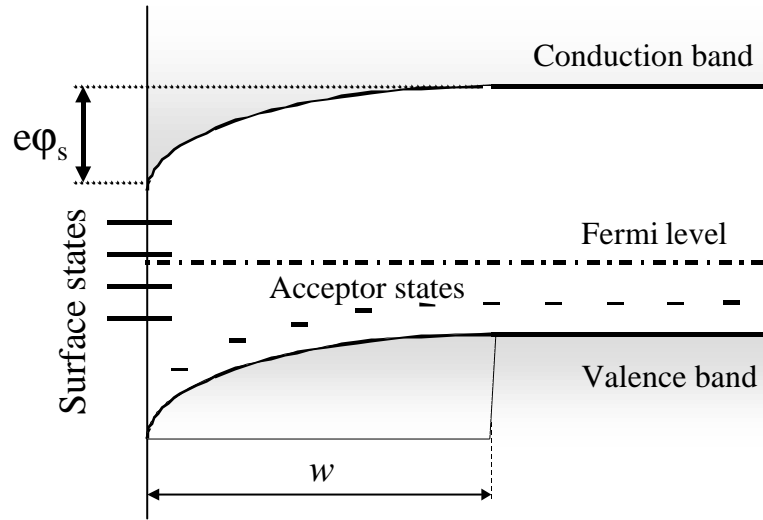


FIG. 1.4: Effect of surface states on the surface of a p-type semiconductor

Let N_s represents the number of surface states, per unit area, with energy position E_t above the Fermi-level E_F . The Fermi - Dirac statistics can be applied to the electrons as particles with a spin $\frac{1}{2}$ and the surface charge in equilibrium conditions can be written as:

$$Q_{SS} = e \frac{N_s}{1 + \exp\left(-\frac{E_t - E_F - e\mathbf{j}_s}{kT}\right)} \quad (1.2.2)$$

where e , k , and T are the electron charge, Boltzmann's constant and absolute temperature, respectively.

1.2.2 Inter-band gap illumination

The absorption of light with a photon energy $h\nu \geq E_G$ leads to the generation of electron - hole pairs via band-to-band transition in the semiconductor. The excess charge tends to be redistributed under the electric field of surface SCR or to be transferred to the surface states from the bulk (or vice versa). The electric potential and the charge distribution are related to each other through the Poisson equation. The potential drops across the surface SCR and, therefore, the surface potential changes. The theoretical treatment of the surface SCR as well as of the photovoltaic effect was given by Garrett and Brattain.²⁰ Later

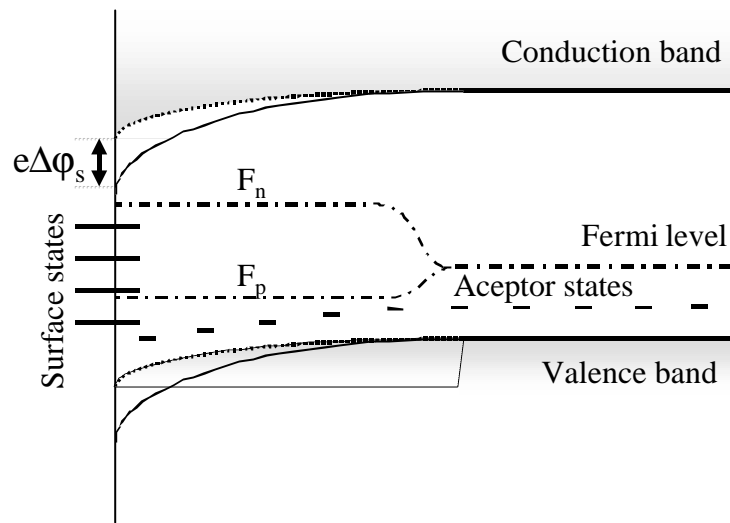


FIG.1.5: Surface of a p-type semiconductor under illumination

Johnson¹⁰ has shown that the experimental value of the photovoltage coincides with the change of the surface potential under illumination. Based mainly on these works, we will analyze the relation between the change of surface potential, e.g. photovoltage, and the excess carrier concentration for steady-state condition.

Under non-equilibrium condition of illumination, the concept of quasi-Fermi-levels can be used. One has to consider separately the quasi-Fermi levels for electrons F_n and for holes F_p which depart from the equilibrium Fermi-level in the area of essential light absorption and diffusion length (Figure 1.5).

A relatively simple mathematical treatment of the problem can be made if one considers the constant quasi-Fermi levels F_n and F_p within the surface SCR (FQL approximation). This approximation is valid under the following conditions: (i) homogeneous illumination of the surface SCR, when the absorption length of the light α^{-1} is comparable with the width of surface space charge region w and (ii) diffusion length of charge carriers L_D is much larger than w . Both conditions implement the absence of concentration gradients of excess charge carriers due to generation by light absorption or due to recombination. We will also neglect the change in the quasi-Fermi levels in the vicinity of the surface due to the increased recombination through surface states. The above approximation describes the usual experimental case while the deviation

from this approximation is numerically considered by Many et al.⁴ Under the FQL approximation the Boltzmann relations are still valid even for non - equilibrium concentrations:

$$n^*(x) = n_0^* \exp\left(\frac{e\mathbf{j}}{kT}\right) \quad p^*(x) = p_0^* \exp\left(-\frac{e\mathbf{j}}{kT}\right) \quad (1.2.3)$$

where n^* , p^* are the non-equilibrium electron and hole concentrations in the surface SCR, respectively, and n_0^* , p_0^* are the non-equilibrium electron and hole concentration at the edge of the SCR.

The dependence of Q_{SCR} on the surface potential can be obtained from the one - dimensional Poisson equation:

$$\mathbf{e} \frac{d^2\mathbf{j}}{dx^2} = -\mathbf{r}(x) \quad (1.2.4)$$

where $x=0$ at the surface and directed toward the bulk of the semiconductor, \mathbf{e} is the permittivity of the semiconductor and $\mathbf{r}(x)$ is the total space-charge density given by

$$\mathbf{r}(x) = e(N_D^+ - N_A^- + p^* - n^*) \quad (1.2.5)$$

where N_D^+ , N_A^- are the concentrations of the ionized donors and acceptors, respectively.

Combining expressions (1.2.3) – (1.2.5) we obtain:

$$\frac{d^2\mathbf{j}}{dx^2} = -\frac{e}{\mathbf{e}} \left[p_0 - n_0 + p_0^* \exp\left(-\frac{e\mathbf{j}}{kT}\right) - n_0^* \exp\left(\frac{e\mathbf{j}}{kT}\right) \right] \quad (1.2.6)$$

The semiconductor is quasi – neutral at infinity, the electric field E , which is by definition $-d\mathbf{j}/dx$, is zero there.

The electric field at the surface E_s is found from the integration of (1.2.6) and substitution $\mathbf{j} = \mathbf{j}_s$. The expression for Q_{SCR} , which follows from the Gauss theorem $Q_{SCR} = -\mathbf{e} E_s$, is given by

$$Q_{SCR} = (2\mathbf{e}kTp_0)^{\frac{1}{2}} F^* \left(\frac{e\mathbf{j}^*}{kT}, \frac{n_0}{p_0}, \Delta_n \right) \quad (1.2.7)$$

where

$$F^* \left(\frac{e\mathbf{j}^*}{kT}, \frac{n_0}{p_0}, \Delta_n \right) = \left[F^2 \left(\frac{e\mathbf{j}^*}{kT}, \frac{n_0}{p_0} \right) + \frac{n_0}{p_0} \Delta_n \left(\exp \left(-\frac{e\mathbf{j}^*}{kT} \right) + \exp \left(\frac{e\mathbf{j}^*}{kT} \right) - 2 \right) \right]^{\frac{1}{2}} \quad (1.2.8)$$

and the fractional carrier increase:

$$\Delta_n = \frac{n_0^* - n_0}{n_0} \quad (1.2.9)$$

where we define:

$$F \left(\frac{e\mathbf{j}}{kT}, \frac{n_0}{p_0} \right) = \left[\left(\exp \left(-\frac{e\mathbf{j}}{kT} \right) + \frac{e\mathbf{j}}{kT} - 1 \right) + \frac{n_0}{p_0} \left(\exp \left(\frac{e\mathbf{j}}{kT} \right) - \frac{e\mathbf{j}}{kT} - 1 \right) \right]^{\frac{1}{2}} \quad (1.2.10)$$

The value of \mathbf{j}_s can be obtained from the transcendent Eq. (1.2.1) with left hand side (1.2.2) and right hand side (1.2.7). The analysis of physical picture is usually based on the graphical approach.¹⁰

The analysis of $D\mathbf{j}_s(D_n)$ depends on the dynamics of the thermal capture (emission) of charge carriers on (from) the surface states. The time necessary to reach the steady-state distribution depends on the thermal cross-section of the involved surface states. Charge exchange with the bulk of “slow states” occurs slowly, with the time constant of the order of seconds, what is essentially larger than the semi-period of the experimentally used light pulses under CW illumination or much longer than the time of measurements under laser excitation. Therefore, the population of “slow states” can be considered as equal to the equilibrium value prior to illumination and as remaining constant under illumination. The charge exchange between “fast states” and the bulk occurs with a time constant of the order of nanoseconds, what is usually much faster than the mentioned above characteristic times of measurements. These states are in thermal equilibrium with bulk and their occupancy is determined by the quasi-Fermi levels. At first, we will consider only the slow states and than extend to the presence of the fast states. The intermediate case will be considered in the next sub-section.

In a simple case, when the population of surface states does not change under illumination, the consideration is essentially simplified. The constant $Q_{SCR}(D_n)$ implies the equal right hand parts of Eq. (1.2.7) with F

and F^* taken from (1.2.10) and (1.2.8), respectively and gives the dependence $Dj_s(D_n)$:

$$\Delta_n = \frac{F^2\left(\frac{ej}{kT}, \frac{n_0}{p_0}\right) - F^2\left(\frac{ej^*}{kT}, \frac{n_0}{p_0}\right)}{\frac{n_0}{p_0}\left(\exp\left(-\frac{ej^*}{kT}\right) + \exp\left(\frac{ej^*}{kT}\right) - 2\right)} \quad (1.2.11)$$

Since $F^* > F$ and both are the monotonous functions of j , in the absence of change in the surface charge, illumination always tends to decrease the band bending. Physically, the photo induced carriers partially screen the fixed surface state charge, thereby reducing the surface band bending. The relation between photovoltage and the fractional carrier increase is a linear one if the photovoltage is less than about $0.05kT/e$.¹¹ The band bending approaches zero for a large enough excess carrier concentration. The saturation of the intensity dependence of the photovoltage allows to determine the equilibrium value of the surface potential. If the bands are flat in equilibrium, they remain flat under illumination.

The SPV is most sensitive to the depleted surface, while the excess carrier concentration necessary to screen the surface charge is much smaller in comparison to the strong inversion case. The smallest sensitivity appears in accumulation when the minority carriers are swept into the bulk, where the recombination probability is very high contrary to the two previous cases where minority carriers are concentrated near the surface with a lack of majority carriers. The SPV method is more sensitive to the wide band gap semiconductors at low temperatures, while the change of the surface potential depends on the ratio between the concentrations of optically induced and intrinsic charge carrier.

The change of the free carrier concentration and the shift of the quasi-Fermi-levels under illumination may cause a transfer of excess charge to/from the surface states from/to the bulk and the total surface charge may change. The population of the “fast states” is determined by the quasi Fermi-level position under illumination due to the Fermi-Dirac statistics (1.2.2).

Therefore, the effect of fast states is essential for the photovoltage if:

- the fast states are present within the range of the quasi-Fermi level

shift (they can be completely empty or completely full and do not change their occupancy in opposite case).

- the change of the surface potential due to fast states population should have the same sign as the charge redistribution
- the change in concentration of fast surface states should be comparable with the concentration of the already filled states (comparable with the charge of the SCR).

The effect of surface charge trapping on the photovoltage may be understood by considering Johnson's graphical method for the calculation of the SPV. In this method, Q_{SCR} and Q_{SS} curves are plotted for each excess carrier concentration, allowing for a calculation of SPV as a function of D_n . Johnson performed comprehensive set of such calculations for Ge and found that the dependence of the SPV on the injection factor was monotonous and that surface states usually did not change the qualitative shape of this dependence. The discussed above requirements are very strict for Ge and no essential deviation from the case of constant surface state concentration was found experimentally. A comprehensive analysis of the influence of surface states is given in the review by Apek et al.²¹ Their theory shows that surface states can essentially change the monotonous dependence of SPV on the excess carrier concentration and even lead to a decrease of the SPV signal. But these results demand extremely large excess carrier concentration and a large surface state density.

So far, we discussed only the steady - state theory of the SPV and time characteristics were taken into account by consideration of "fast" and "slow" states. No general theory which describes the time-resolved increase of the SPV was given. Some analytical attempts were made for modulated illumination in the assumption of the low-signal case.^{22,23} However, they are limited to a very narrow range of cases and can not be applied to the interpretations of the experimental data given in this thesis. A first analysis of the time-resolved PV transients was made by Johnson.¹¹ The relaxation of the PV was described by the recombination of minority carriers and the lifetime of minority carriers was measured. An increase time of the SPV signal in crystalline semiconductors under pulse illumination is always much faster, than the duration of the light pulse and a non-steady state increase of the PV transients was not observed for inter-band gap illumination after illumination. The examples of the PV transients for crystalline Si are given in Figure 1.1

and the theoretical background for the non-steady state PV increase will be discussed below (sub-section 1.3.3).

An estimation of the SCR width can be made for depletion approximation. The approximation assumes that the region where the mobile carriers are negligible terminates abruptly at a distance w from the surface:

$$\hat{e}Q_{SCR} \epsilon = e \epsilon (N_A - N_D) w \quad (1.2.12)$$

Replacing Q_{SCR} from (1.2.7) for appropriate depletion regime one obtains:

$$w = \sqrt{\frac{2e j_s}{e |N_A - N_D|}} \quad (1.2.13)$$

For a reasonable set of parameter: $j_s = 0.5 \text{ V}$, $e/e_0 = 10$, $N_A = 5 \cdot 10^{14} \text{ cm}^{-3}$ the value of w is $1 \mu\text{m}$. The surface states which are located within a few monolayers on the semiconductor surface influence thousands monolayers away from the surface. This property allows to use surface SCR as a probe to investigate surface states as well as bulk properties of semiconductors by several modifications of the photovoltage technique.^{24,25}

Our work is concentrated on materials with characteristic dimensions in the nanometer range. Therefore, if not considering highly doped semiconductors, the nanoparticle is completely depleted due to the intrinsic surface states and the surface SCR due to the geometrical surface is extended over many nanoparticles.

1.2.3 Sub-band gap illumination

The shape of a photovoltage transient depends essentially on the dynamics of the surface state population/depopulation. The change of the occupation is essential under the sub-band gap illumination. This question has been experimentally and theoretically studied by Gatos et al.¹³⁻¹⁷ To define the situation, let us consider the surface of n-type semiconductor with surface states E_t filled by electrons (Fig.1.6(a)). Incident photons with an energy $E_c - E_t < h\nu < E_G$ release electrons from the surface states and the electric field of surface SCR sweeps them

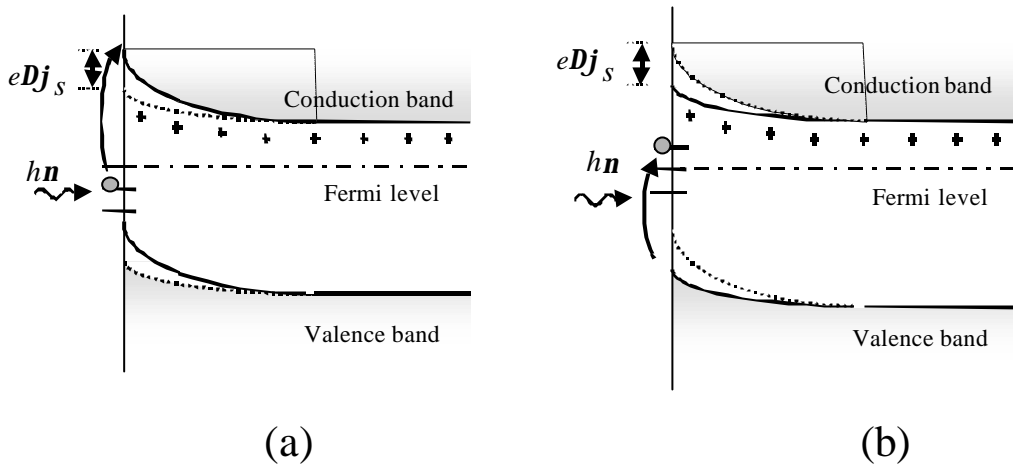


FIG.1.6: Surface state depopulation (a), and population (b) in an n-type semiconductor under sub-band gap illumination.

into the bulk. The surface potential decreases in this case. The complementary process is shown in Fig.1.6(b). If the semiconductor surface contains unoccupied surface states with energy E_t , photons with an energy $E_V - E_t < h\nu < E_G$ excite electrons from the valence band into surface states (Fig.1.6(b)). The net negative charge located at the surface increases. The free holes created in the valence band recombine in the bulk within the minority carrier lifetime. Conservation of charge requires the corresponding increase of the barrier height. Accordingly, a decrease of the surface conductivity is expected, which was indeed experimentally observed.¹⁴ Movement of excess holes from the surface is also possible due to the gradient of concentration at high excitation level.

The properties of the surface states as well as bulk states are usually described by a set of phenomenological parameters of the Shockley-Read-Hall (SRH) statistics. The basic electronic transitions between bands and trap states are shown in Figure 1.7. Due to thermal excitation, electrons may be excited from the surface state into the conduction band at a rate of g_n^{th} and holes into the valence band at a rate of g_p^{th} . Conduction band electrons may be captured in the surface state at a rate of r_n^{th} and valence band holes at a rate of r_p^{th} . If the semiconductor is illuminated, absorbed photons may excite electrons from the surface state to the conduction band at a rate of g_n^{opt} , holes to the valence band at a rate of g_p^{opt} . All rates are per unit volume.

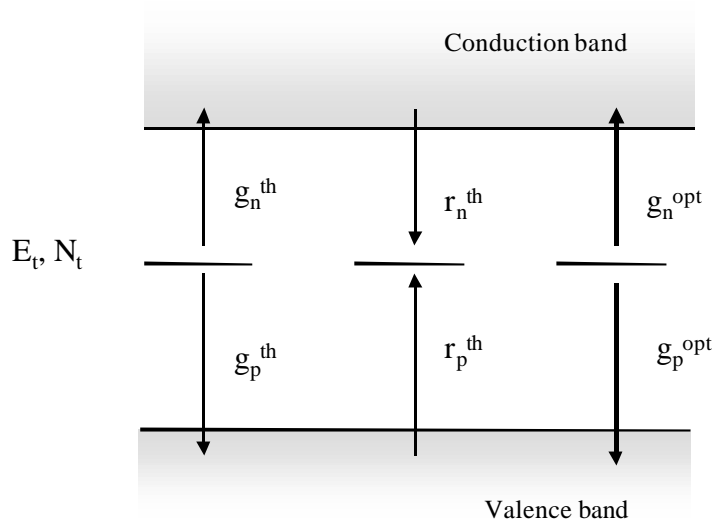


FIG.1.7: Elementary band – trap – band transitions

All of the above transition rates may be expressed in terms of more fundamental quantities. The surface state concentration per unit area is N_t , the electron occupation is n_t , and the surface state energy is E_t . These three quantities are related via standard Fermi-Dirac statistics:

$$n_t = \frac{N_t}{1 + \exp\left(-\frac{E_t - E_F}{kT}\right)} \quad (1.2.14)$$

The electron capture rate r_n^{th} is proportional to the concentration of electrons in the conduction band n and to the concentration of empty states ($N_t - n_t$):

$$r_n^{th} = \mathbf{s}_n v_{th} n (N_t - n_t) \quad (1.2.15)$$

where by definition the capture coefficient of electrons is $\sigma_n v_{th}$. The effective cross-section of trap for electrons \mathbf{s}_n depends on the nature of trap and temperature, v_{th} is the thermal velocity of electrons.

The electron thermal emission rate for non-degenerate semiconductor is proportional to the concentration of electrons in the surface states n_t :

$$g_n^{th} = \mathbf{s}_n v_{th} n_1 n_t \quad (1.2.16)$$

where the constant n_1 is given by

$$n_1 = N_C \exp\left(-\frac{E_C - E_t}{kT}\right) \quad (1.2.17)$$

where N_C is the effective density of states in the conduction band.

The optical generation rate must be proportional to n_t and to the incident photon flux I :

$$g_n^{opt} = S^{opt} I n_t \quad (1.2.18)$$

where the proportionality constant σ_{opt} is the optical cross-section of the traps. Similar expressions can be written for transition rates of holes.

The quantitative analysis of the photovoltage is based on the finding of the surface potential under illumination. Let's assume that the thermal cross-section for holes is very small, the filled states are situated in the upper part of the band gap and photon energy of illumination $h\nu < E_G/2$. In this case, all transitions involving minority carriers can be neglected and the rate equation for the surface state concentration can be written as:

$$\frac{dn_t}{dt} = -S^{opt} I n_t - S_n v_{th} n_1 n_t + S_n v_{th} (N_t - n_t) n \quad (1.2.19)$$

Under steady state condition the surface state charge is:

$$Q_{SS} = -en_t = \frac{e S_n v_{th} n N_t}{S^{opt} I + S_n v_{th} (n_1 + n)} \quad (1.2.20)$$

with the electron concentration at the surface

$$n = n_0 \exp\left(-\frac{e\phi_s}{kT}\right) \quad (1.2.21)$$

The expressions (1.2.7) and (1.2.20) give the value of surface potential. A theoretical study of the photovoltage was made by Szaro.²⁶ The photovoltage signal increases with increasing surface state concentration (more electron transitions are induced for the same photon flux), decreasing bulk electron concentration (the screening of the surface disturbance from equilibrium is more difficult and finally larger SPV is

needed to change the bulk charge distribution) and decreasing temperature (the thermal transitions are suppressed). The sub-bandgap SPV is also expected to decrease with increasing semiconductor bandgap.

The transient response of the PV can be obtained by solution of (1.2.20) and the Poisson equation. The time necessary to reach the steady-state distribution depends on the thermal cross-section of surface states, which vary over many orders of magnitude. An analysis of photovoltage transients was performed by Gatos. An essential photovoltage is only possible if there is no thermal equilibrium of minority carriers and if the number of thermally activated transitions from the valence band is negligible. Wide bandgap semiconductors with deep states (CdS, CdSe) are typical examples. The spectral distribution of photovoltage gives directly the energy position of surface states. Transient photovoltage measurements give information on the surface state concentration, thermal and optical cross-sections, occupancy. The procedure of extraction of these parameters from the photovoltage transients under CW illumination is described in Ref. 27.

Similar processes of population/depopulation of trap states under sub-bandgap illumination are also possible for the states of the semiconductor situated within the surface SCR.^{28,29} One can distinguish between surface and bulk states by using additionally spectral photoconductivity measurements, while the photoconductivity is not sensitive to the surface states.

The artificial creation of surface states by deposition of metals on semiconductor surfaces and formation of Schottky barriers for thick enough metal layers was investigated by Brillson.^{30,31} Band diagrams of metal-semiconductor interfaces were constructed from photovoltage measurements.

Thin porous Si layers on the Si substrate were investigated by Dittrich, Timoshenko.^{32,33} The surface space charge region of the crystalline Si was used as a probe for the stored charge in porous Silicon by trapping/detrapping processes. Trapping/detrapping of charge carriers on/from the states of porous silicon leads to the decrease/increase of photovoltage.

An extended review of theory, experimental tools, and applications of the SPV phenomena in crystalline materials can be found in Ref. 9.

1.3 Diffusion of light induced charge carriers

1.3.1 General case

Diffusion of light induced charge carriers will be discussed for thin films of some porous materials and organic polymers. The surface states on the surface of nanoparticles are extended over the all volume of porous materials. The absence of far order in the lattice of polymers diminishes the role of the surface states on the geometrical surface for the potential perturbation inside the bulk. The intrinsic charge carrier concentration is usually very small in the materials of both types. Therefore, the electric field is negligible and the width is larger than the thickness of the films for the surface space charge region in these cases. The spatial separation of the light induced charge carriers under both, the inter- and sub-band gap illumination, is caused by the electric field of the surface space charge region for crystalline semiconductors. The built-in electric field loses its dominating role for the separation of the light induced charge carriers in nanoporous materials and organic polymers and other reasons should be considered. The flat band condition over the macroscopic range (several nanoparticles) can be discussed for the nanoporous semiconductors and organic polymers. It is also the case for a crystalline semiconductor under inter-bandgap illumination of large intensity, when the excess charge carriers of comparable or larger than the doping level concentration screen the charge trapped on the surface states.

Let us consider a semi - infinite homogeneous semiconductor under illumination with photons of $h\nu \gg E_g$. The concentrations of excess electrons n and holes p are steep functions of the spatial coordinates in the case of strong light absorption. Figure 1.8(a,b) shows the concentrations of the excess electrons $n(x)$ and holes $p(x)$ (a) and non-equilibrium charge distribution $p(x) - n(x)$ as functions of the spatial coordinate x in the one - dimensional case (particular case of \mathbf{d} - excitation in time). The axis is perpendicular to the free surface, directed toward the bulk, and its zero point is at the free surface of the semiconductor. The profile of the concentrations $p(x)$, $n(x)$ at the initial moment of time $t_0=0$ is determined by the absorption coefficient of the light. The condition of thermo - dynamic equilibrium demands a Fermi - level constant in space. The gradient of the concentration is the driving force for the diffusion flux. Figure 1.8 (c, d) illustrates $n(x)$, $p(x)$ and

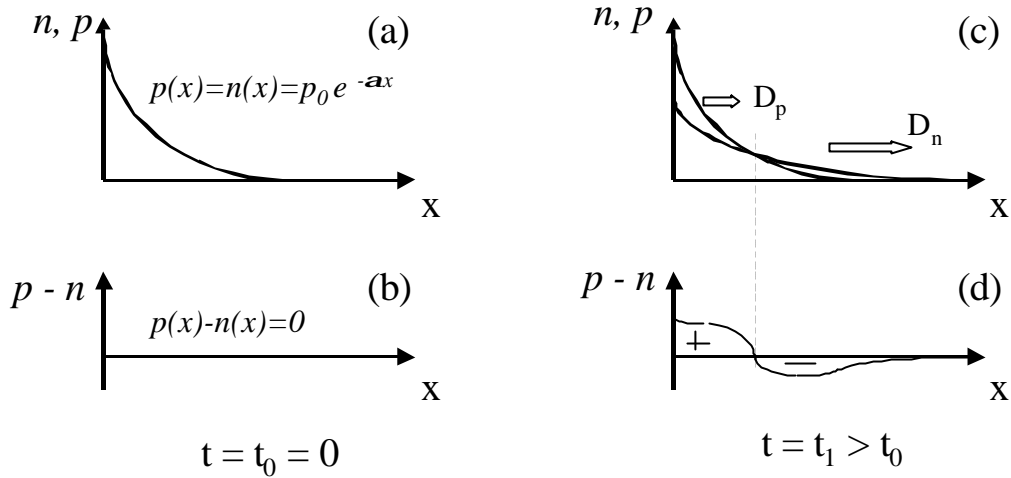


FIG.1.8: Concentration gradients of excess electrons $n(x)$ and holes $p(x)$ (a,c) and non-equilibrium space charge distribution $p(x) - n(x)$ (b,d) under δ -pulse of light excitation with $h\nu \gg E_G$ for initial moment of time $t_0 = 0$ (a,b) and after some finite span $t_1 > t_0$ (c,d).

$p(x) - n(x)$ after some finite time t_1 after d - excitation. The electric field $E(x)$ between charge carriers of opposite sign and field currents appear to compensate the flow of diffusion currents. The electron and hole current densities j_n, j_p in terms of drift - diffusion approximation are³⁴:

$$j_n = e m_n n E + e D_n \frac{\partial n}{\partial x} \tag{1.3.1a}$$

$$j_p = e m_p p E - e D_p \frac{\partial p}{\partial x} \tag{1.3.1b}$$

where e is the elementary charge, $m_n, (m_p)$ is the effective electron (hole) mobility, $D_n, (D_p)$ is the effective electron (hole) diffusion coefficient. By using effective coefficients we take into account a microscopic transport picture (trapping/detrapping processes, thermal overcoming or tunneling through grain boundaries and so on) without consideration of the transport mechanism.

The equation of continuity in the theory of electric current flow expresses the condition that there is no accumulation of charge. It is generally written for electrons and holes in the form:

$$\frac{\partial n}{\partial t} = G_n - R_n + \frac{1}{e} \frac{\partial J_n}{\partial x} \quad (1.3.2a)$$

$$\frac{\partial p}{\partial t} = G_p - R_p - \frac{1}{e} \frac{\partial J_p}{\partial x} \quad (1.3.2b)$$

where G_n (G_p) and R_n (R_p) are the generation and recombination rates, respectively of electrons (holes) per unit volume.

The electric field of separated charge carriers is given by the Poisson equation:

$$\frac{\partial E}{\partial x} = -\frac{e(p-n)}{\epsilon \epsilon_0} \quad (1.3.3)$$

The parameter ϵ is the dielectric constant of the material, $\epsilon_0 = 8.85 \times 10^{-14}$ F/cm. The set of the differential equations (1.3.1) - (1.3.3) is coupled by three variables: $n(x)$, $p(x)$, $E(x)$. Any particular solution of this system demands the specification of generation and recombination terms, initial and boundary conditions. However, the physical picture of the involved processes can be shown after some manipulations with the considered equations.

Substitution of (1.3.1) and (1.3.3) into (1.3.2) produces the final equations for concentrations:

$$\frac{\partial n}{\partial t} = G_n - R_n - en\mathbf{m}_e \frac{p-n}{\epsilon \epsilon_0} + E\mathbf{m}_e \frac{\partial n}{\partial x} + D_e \frac{\partial^2 n}{\partial x^2} \quad (1.3.4a)$$

$$\frac{\partial p}{\partial t} = G_p - R_p + ep\mathbf{m}_h \frac{p-n}{\epsilon \epsilon_0} - E\mathbf{m}_h \frac{\partial p}{\partial x} + D_h \frac{\partial^2 p}{\partial x^2} \quad (1.3.4b)$$

Multiplication of (1.3.4a) and (1.3.4b) (without consideration of generation-recombination terms) with $en\mathbf{m}_e$ and $ep\mathbf{m}_h$, respectively, addition of them and assumption of $p = n$ (its validity for the discussed procedure one can find in Ref. 34; however, this assumption is not true in general case and the electric field between separated charge is given by (1.3.3)) will produce:

$$\frac{\partial p}{\partial t} = D \frac{\partial^2 p}{\partial x^2} - \mathbf{mE} \frac{\partial p}{\partial x} \quad (1.3.5)$$

where if taking into account Einstein equations $D_{e,h} = kT/e \mathbf{m}_{e,h}$ the effective diffusion coefficient and mobility are:

$$D = \frac{p+n}{\frac{n}{D_h} + \frac{p}{D_e}} \quad \mathbf{m} = \frac{n-p}{\frac{n}{\mathbf{m}_h} + \frac{p}{\mathbf{m}_e}} \quad (1.3.6)$$

The physics of the involved processes can be understood now. Under gradients of concentration (due to non-homogeneous light adsorption) the excess charge carriers diffuse with different diffusion coefficients for electrons D_e and holes D_h . Separation of the excess electrons and holes leads to the appearance of the electric field which tends to slow down faster charge carriers and accelerate the slower charge carriers up to complete compensation of the diffusion fluxes by the drift fluxes. The expression (1.3.5) describes the ambipolar diffusion of the coupled electron and hole clouds with effective diffusion coefficient and mobility (1.3.6).

Solution of equations (1.3.4), substitution of the excess concentrations $p(x)$, $n(x)$ into the Poisson equation and integration of the electric field $E(x,t)$ over the thickness of the sample L will produce the transient photovoltage $U_{pv}(t)$:

$$U_{PV}(t) = \int_0^L E(x,t) dx \quad (1.3.7)$$

However, equations (1.3.4) can not be analitically solved even for simplest boundary conditions. Further consideration demands reasonable physical simplifications which will be discussed below.

1.3.2 Dember effect, steady state case

A simple analytical model can be obtained in the steady – state case. The electric field across the sample induced by a steady-state illumination may be calculated from the requirements of zero the total current $j_n + j_p = 0$.

If expressing the currents in the form (1.3.1) and assuming $n(x) = p(x)$ the electric field is given by

$$E(x) = \frac{D_p - D_n}{e(n_0 \mathbf{m}_n + p_0 \mathbf{m}_p) + e(\mathbf{m}_n + \mathbf{m}_p)n} \frac{\partial n}{\partial x} \quad (1.3.8)$$

where n_0, p_0 are the equilibrium concentrations of electrons and hole, respectively. The photovoltage U_{pv} , which got the name of Dember PV²⁰ for these conditions, can be obtained by integration of the electrical field $E(x)$ over the thickness:

$$U_{PV} = \frac{kT}{e} \frac{\mathbf{m}_n - \mathbf{m}_p}{\mathbf{m}_n + \mathbf{m}_p} \ln \left[1 + \frac{e(\mathbf{m}_n + \mathbf{m}_p)n}{e(n_0 \mathbf{m}_n + p_0 \mathbf{m}_p)} \right] \quad (1.3.9)$$

The typical value of the Dember PV can be estimated, for example, for a p - type crystalline Si with excitation level 10^{-2} as 1.7 mV. This value is much smaller than the typical surface PV of about several 100 mV which is related to the surface space charge region. The sign of the Dember PV is positive if electrons have larger mobility and negative in the opposite case. Additionally, the Dember PV is larger for the semiconductor with larger difference between mobility of electrons and of holes and vanishes to zero for equal mobilities.

The Dember PV increases logarithmically with increasing excess carrier concentration and, at high enough excitation levels, it can prevail over the surface PV which saturates at the value of the surface potential for high excitation levels. This fact allows to observe Dember PV experimentally at higher excitation levels. However, the value of surface PV can be suppressed in the case of good electronic passivation of surface states of the semiconductor. In this case, the concentration of the trapped charge is very small and the deviation of the surface potential from the potential in the bulk of the semiconductor is small. The pure logarithmic dependence of the PV on the intensity was observed for crystalline Si where special attention was paid to the surface passivation by Dittrich et al.³⁵ While preferentially surface properties were characterized by the surface PV,⁹ the Dember PV contains information on the bulk properties of the semiconductor, like doping level, mobility.

1.3.3 Maxwell (dielectric) relaxation time

When the non - equilibrium space charge appears in the semiconductor due to external perturbations (light, injection, etc.), diffusion - drift fluxes tend to vanish this perturbation charge in the homogeneous semiconductor. The characteristic time after which the drift - diffusion equilibrium is reached can be introduced.

If the non - equilibrium space charge of density ρ appears in the semiconductor, the electric field \vec{E} between charge carriers of opposite sign can be found from the Poisson equation:

$$\text{div } \vec{E} = \frac{\mathbf{r}}{\mathbf{e} \mathbf{e}_0} \quad (1.3.10)$$

The drift - diffusion fluxes which tend to compensate the electric field are continuous in space (conservation of charge). This fact is described by the continuity equation:

$$\text{div } \vec{j} = - \frac{\partial \mathbf{r}}{\partial t} \quad (1.3.11)$$

where the current can be present as $\vec{j} = \mathbf{s} \vec{E}$ and in the case of homogeneous semiconductor combination of the (1.3.10)–(1.3.11) produces the time relaxation of the space charge

$$\mathbf{r} = \mathbf{r}_0 \exp\left(-\frac{\mathbf{s}}{\mathbf{e} \mathbf{e}_0} t\right) \quad (1.3.12)$$

Therefore, the non-equilibrium charge disappears within the time constant, by definition, the Maxwell (dielectric) relaxation time:

$$\mathbf{t}_M = \frac{\mathbf{e} \mathbf{e}_0}{\mathbf{s}} \quad (1.3.13)$$

An estimation of the Maxwell relaxation time for typical crystalline semiconductors, for example Si with $\mathbf{s} = 1 \text{ } \Omega\text{cm}$, $\mathbf{e} = 12$, $\mathbf{e}_0 = 10^{-13} \text{ F/cm}^{-1}$ gives a value of $\mathbf{t}_M = 10^{-12} \text{ s}$. The situation is more complicated if considering the large excitation level with concentration gradients. The

conductivity is a function of the spatial coordinates as well as t_M should be considered as a differential quantity.

1.3.4 Diffusion PV model, non-steady state case

While the formation of the PV in semiconductors is related to the spatial separation of the light induced charge carriers (drift - diffusion fluxes), the Maxwell relaxation time can be considered as the time, necessary to reach the steady - state case. Our experimental data show no retardation of the PV in the crystalline semiconductors with respect to the laser pulse duration (compare duration of the laser pulse of the order of 10^{-9} s and Maxwell relaxation of the order of 10^{-12} s). However this is not the case of some porous semiconductors and polymers where the Maxwell relaxation time can be of the order of 10^3 s. The non-steady state case should be considered in equations (1.3.1) – (1.3.3) for these semiconductors up to times of the Maxwell relaxation time and transient PV can be obtained from the integration of the electric field over the thickness of the samples (1.3.7).

The non-steady state PV will be excited by short laser pulse while the characteristic features of the transients will appear after several orders of magnitude in time later. In this case, a δ -function is a good approximation for the time dependence of the light pulse. In the case of illumination with absorption coefficient \mathbf{a} , the generation rates can be written as:

$$G_n(x,t=0) = G_p(x,t=0) = \mathbf{a} n_0 e^{-\mathbf{a}x} \quad (1.3.14)$$

where n_0 (p_0) is the initial concentration of electrons (holes) at the surface ($x=0$).

Let's discuss the specifics of the recombination terms for the considered class of materials. The present model will be applied to wide band gap semiconductors with a very small intrinsic carrier concentration which can be neglected in comparison to the excess electron and hole concentrations. Therefore, the recombination rates for electrons and holes are proportional to the both excess charge carrier concentrations:

$$R_{n,p} = \mathbf{g} n p \quad (1.3.15)$$

where \mathbf{g} is the coefficient of recombination.

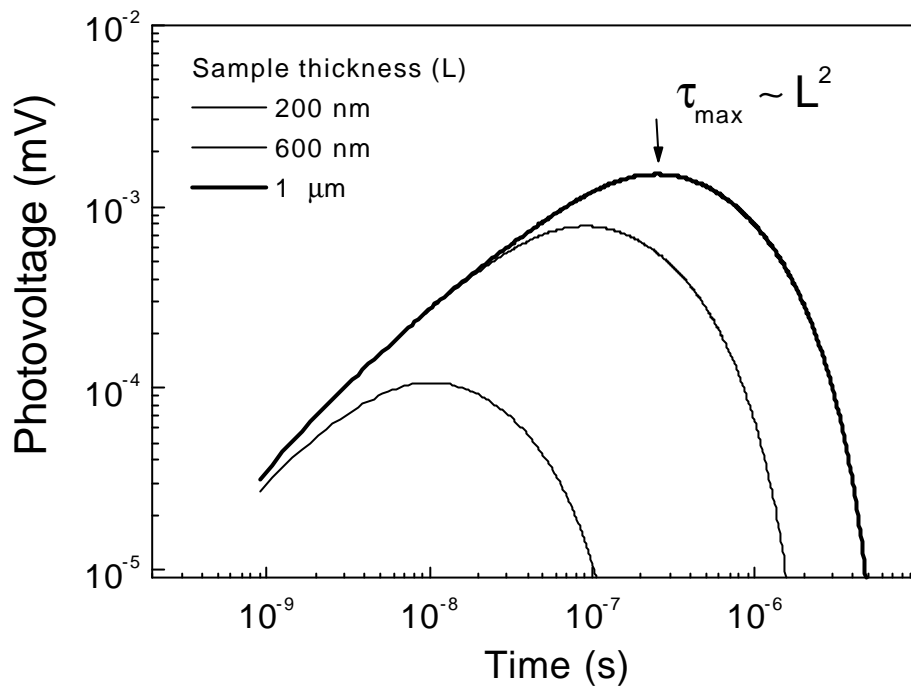


FIG. 1.9: Simulated PV transients for different thickness of the film. Parameters of the simulation are: $D_n = 10^{-2} \text{ cm}^2/\text{s}$, $D_n/D_p=10$, $\mathbf{a} = 3 \cdot 10^4 \text{ cm}^{-1}$, $n_0 = 3 \cdot 10^{10} \text{ cm}^{-3}$, $\mathbf{e} = 10$. The electric field between separated charge is neglected.

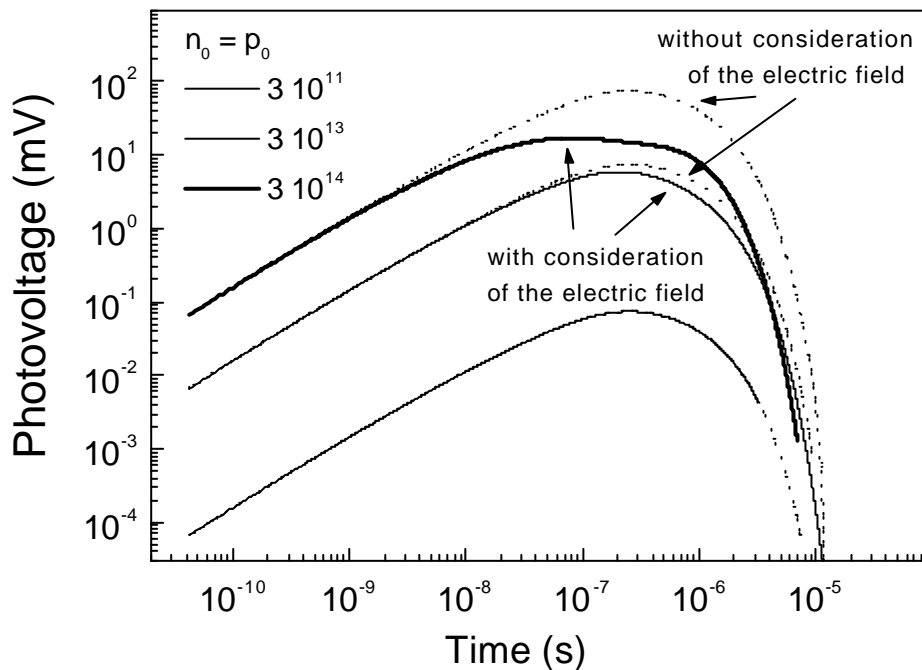


FIG. 1.10: Comparison of the simulated PV transients for different excitation levels ($n_0=p_0$) with (solid lines) and without (dash lines) consideration of the electric field between separated charge. Parameters of the simulation are: $D_n = 10^{-2} \text{ cm}^2/\text{s}$, $D_n/D_p=10$, $\mathbf{a} = 3 \cdot 10^4 \text{ cm}^{-1}$, $L = 1 \text{ μm}$, $\mathbf{e} = 10$.

The recombination is increased in space by the large overlap of the excess concentrations and suppressed in the space where only one type of charge carriers dominates.

A complete task of the simulation of the PV transients consists of the simultaneous solution of the completed non-steady state system of Eqs. (1.3.1) – (1.3.3) with the generation (1.3.14) and recombination terms (1.3.15).

The solution of the non-steady state equations can be found only by numerical simulation. The program of numerical simulations was written in Microsoft Delphi. The results of simulations are shown in Figures 1.9 – 1.12 for different set of parameters: D_n , D_p , \mathbf{a} , L , \mathbf{e} , $n_0=p_0$, \mathbf{g}

Figure 1.9 shows simulated PV transients for different thickness of the films (L). Other parameters of the simulations are: $D_n = 10^{-2} \text{ cm}^2/\text{s}$, $D_n/D_p=10$, $\mathbf{a} = 3 \cdot 10^4 \text{ cm}^{-1}$, $n_0 = 3 \cdot 10^{10} \text{ cm}^{-3}$. The drift terms in Eqs. (1.3.4) are neglected and “diffusion case” can be considered. The neglect of the drift term in comparison to the diffusion term is possible for semiconductors on the time scale before the Maxwell relaxation time is reached. The generation term of excess charge carriers in time is a δ - function, gradient of concentration of excess electrons and holes exists. As shown, diffusion of electrons with 10 times larger diffusion coefficient leads to the charge separation, formation of the electric field (which can be neglected in the continuity equations, but not in the Poisson equation) and photovoltage. An increase of the PV is caused by an increase of the distance of separation between charge of opposite sign. The maximal distance of the charge carrier separation is the thickness of the film for thin films. The transit time of charge carriers over the sample $t_{max} = L^2/D_n$ can be considered. The maximum of the PV transient is in good agreement with the transit time.

Figure 1.10 compares the simulated PV transients without and with consideration of drift terms in Eqs. (1.3.4) for different excitation levels ($n_0 = p_0$). Parameters of the simulation are: $D_n = 10^{-2} \text{ cm}^2/\text{s}$, $D_n/D_p=10$, $\mathbf{a} = 3 \cdot 10^4 \text{ cm}^{-1}$, $L = 1 \text{ }\mu\text{m}$, $\mathbf{e} = 10$. The electric field slows down the diffusion of faster charge carriers (electrons) and accelerates the slower charge carriers (holes). The smaller value of the PV for the case of intermediate excitation level ($n_0=3 \cdot 10^{13} \text{ cm}^{-3}$) describes this process if taking into account the electric field between separated charge. An almost saturated value of the PV (between 10^{-8} s and 10^{-6} s the simulated PV signal is practically constant) for a large excitation level ($n_0=3 \cdot 10^{14} \text{ cm}^{-3}$) illustrates the joint movement of electron - hole cloud and the

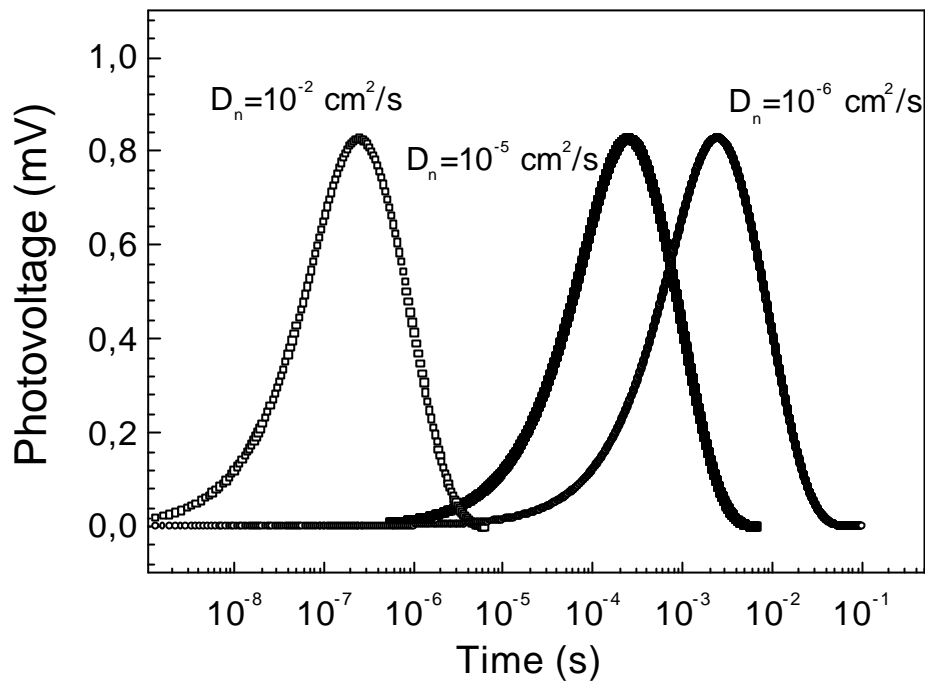


FIG. 1.11: Simulated PV transients for different diffusion coefficients of electrons D_n . Other parameters of the simulation are: $D_n/D_p=10$, $L = 1 \mu\text{m}$, $\mathbf{a} = 3 \cdot 10^4 \text{ cm}^{-1}$, $n_0 = 3 \cdot 10^{12} \text{ cm}^{-3}$, $\mathbf{e} = 10$.

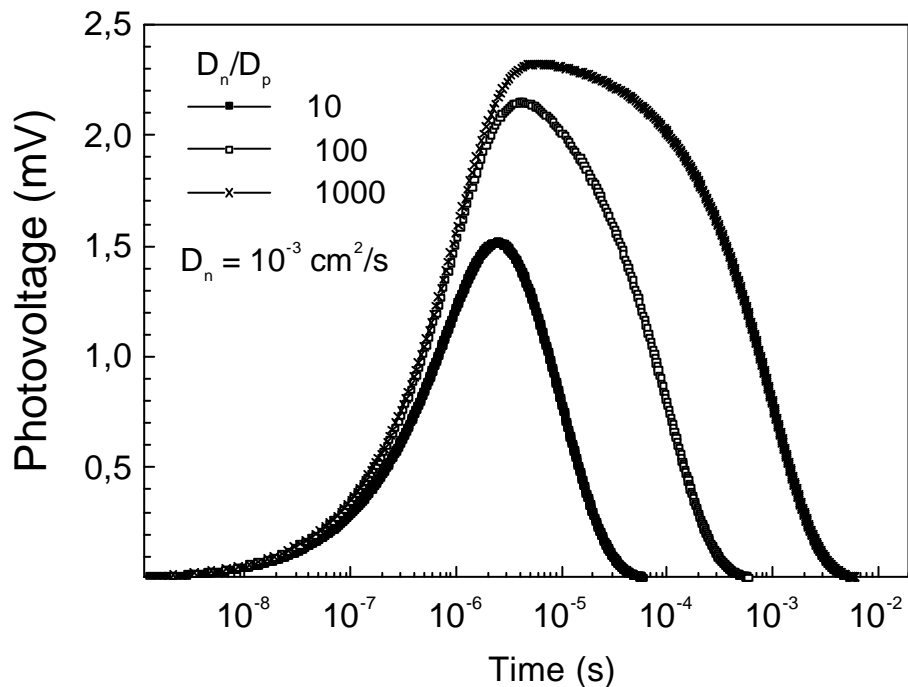


FIG. 1.12: Simulated PV transients for different ratios between diffusion coefficients of electrons and holes D_n/D_p . Parameters of the simulation are: $D_n = 10^{-3} \text{ cm}^2/\text{s}$, $L = 1 \mu\text{m}$, $\mathbf{a} = 3 \cdot 10^4 \text{ cm}^{-1}$, $n_0 = 3 \cdot 10^{12} \text{ cm}^{-3}$, $\mathbf{e} = 10$.

tendency to the steady – state case. The maximum of the PV means compensation of the separation due to diffusion gradients by the attraction due to drift. The decay of the PV is determined by the recombination of excess charge carriers in this case. The time of maximum of PV transient is shifted toward shorter times with increasing excitation level (solid lines) and therefore, the Maxwell relaxation time. The value of t_{peak} is independent on the excitation level for “diffusion case” (dash lines).

Figure 1.11 shows simulated PV transients for different diffusion coefficients of electrons D_n . Other parameters of the simulation are: $D_n/D_p=10$, $L = 1 \mu\text{m}$, $\mathbf{a} = 3 \cdot 10^4 \text{ cm}^{-1}$, $n_0 = 3 \cdot 10^{12} \text{ cm}^{-3}$, $\mathbf{e} = 10$. The maximum of the PV is determined by the diffusion coefficient of faster charge carriers. The ratio between the diffusion coefficients of electrons and holes determines the “width” of the PV transient (Figure1.12). The decay of the PV is related to the decrease of the separation distance due to movement of the slower charge carriers. The amplitude of the PV slightly increases with the increasing ratio D_n/D_p because of the increase of the possible distance of separation, for times when the faster charge carriers reach the back surface, the cloud of slower charge carriers is situated closer to the free surface if their diffusion coefficient is smaller.

1.4 Model of Interface PV in metal oxide layer with trap states

1.4.1 Photovoltage in thin films, heterostructures, and superlattices

The previous consideration of the photovoltage phenomena assumes the semi-infinite uniform sample, when the thickness of the sample is much larger than (i) the absorption length of the light and (ii) the diffusion length of excess charge carriers. In this case, the equilibrium Fermi-level is far away from the illuminated surface and does not change under illumination. The previous consideration fails when these conditions are not satisfied and the excess charge carriers are present near the back surface. Additional effects should be taken into account in this case. Lets consider the case of a thin semiconductor film on the metal substrate. Two surface SCRs are present here: at the free surface of the semiconductor film and at the semiconductor/metal interface. If the metal does not change the sign of surface potential at the back contact (respective relation between workfunctions of semiconductor and metal or Fermi-level of semiconductor is pinned by the own surface states introducing interface dipole) under illumination both the surface SCR and interface SCR are active and may compensate the photovoltage from each other. If the SCRs have opposite sign of band bending, the photovoltage may be increased. If the sample is not uniform, i.e. contains the buried interfaces (heterostructures, superlattices) the input of all surface space charge regions should be taken into account, where the excess charge is present due to generation or diffusion. Special attention should be paid to the analysis of the spectral dependent photovoltage, when the wavelength of illumination and, therefore, the absorption length of the light are changed in a wide range and the ratio between different interfaces changes dramatically.

The sensitivity of the photovoltage to the buried interfaces was numerously used for the spectroscopy of multilayer structures, construction of band diagrams of homostructures, heterostructures, and superlattices. The review on this phenomena can be found in the review by Kronik et al.⁹

1.4.2 Formation of the PV at metal oxide/metal interface

Metal oxides are usually large band gap semiconductors with a very low intrinsic carrier concentration. The small thickness of ultrathin layers diminishes the role of the built-in electric field (at the free surface or interface) or concentration gradients of excess charge carriers for the charge separation and formation of the PV inside the layer. At the same time, a band discontinuity at the interface with the metal substrate may lead to a charge separation.

The behaviours of the increase and of the decay of the PV transients contains information about the formation and relaxation mechanism of the PV signal. The role of diffusion and drift processes for the separation of excess charge carriers is discussed on the base of the PV increase above. An exponential decay of the PV, for example, suggests recombination of charge carriers with a single lifetime,¹¹ time - extended exponential law assumes spatial or energy dispersion.^{36,37} Logarithmic decays of the photoconductivity are known for persistent photocurrents.³⁸ The present model is developed to explain the mechanism of formation of the PV and the particular decay of the experimental PV transients (see Chapter 4.2 for experimental data) in ultrathin metal oxide layers with trap states.

Let us consider an ultrathin metal oxide layer on the surface of a metal substrate under illumination with a photon energy $h\nu$. The band energy diagram of the heterostructure (MeO_x/Me) is shown in Fig.1.12 (a). The values of E_c , E_v , and E_F are the edge of the conductive and valence band, and Fermi-level, respectively. A metal oxide contains electronic states (energy E_t) in the band gap which act as deep traps (large detrapping time) for one type of charge carriers (holes, for definiteness). "Ultrathin" thickness of the metal oxide layer (d) means a small thickness in comparison to the reciprocal absorption length of the light (α^{-1}) and to the width of surface or interface space charge region (W). The illumination with a photon energy $h\nu > E_G$ and $\alpha^{-1} \approx d, W$ excites the charge carriers homogeneously over the thickness of the metal oxide layer (Fig.1.12 (b)). The electrons escape from the metal oxide and occupy the states with lower energy in the metal, while holes are trapped on the traps inside the metal oxide layer (Fig.1.12(c)). The charge distribution after the separation is shown in Fig.1.12(d). The initial concentration of trapped holes $p(x, t=0)$ is determined by the

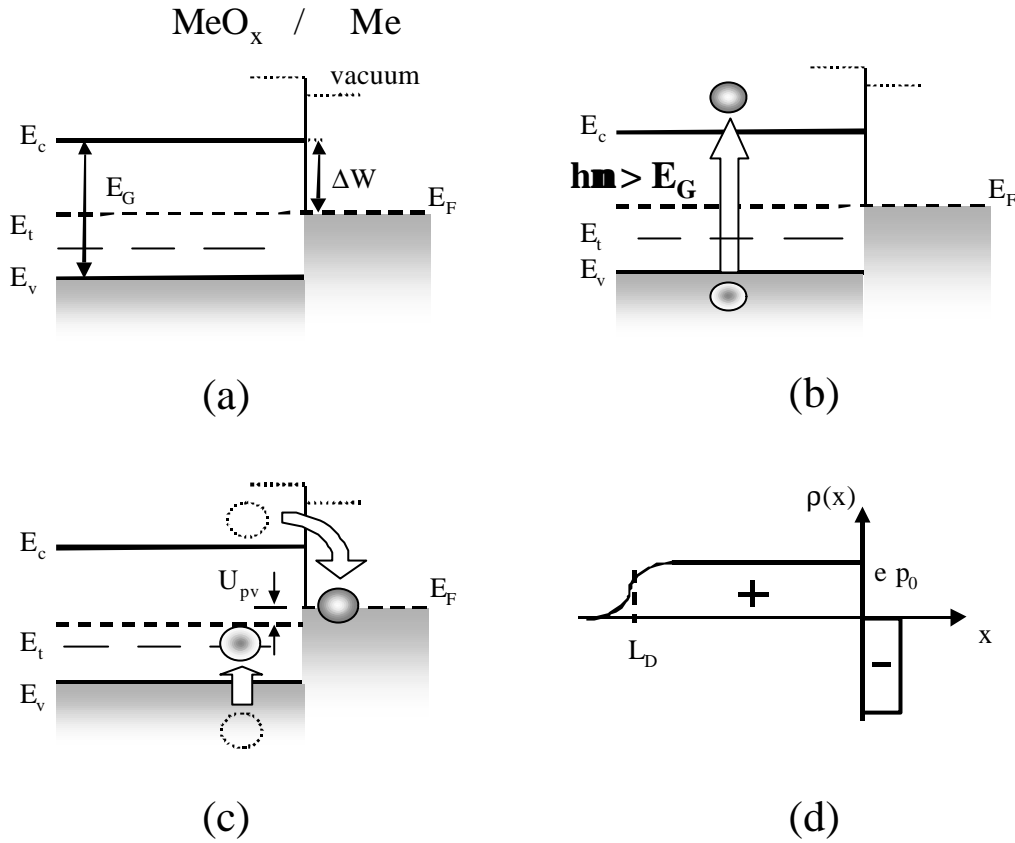


FIG. 1.12: Band energy diagram of MeO_x/Me interface in equilibrium (a), under illumination with photon energy $h\nu > E_G$ (b), separation of excess charge carriers by electron injection into the Me and hole trapping on the E_t inside MeO_x (c), spatial distribution of non-equilibrium charge $\rho(x)$ (d).

concentration of photo - excited holes p_0 for small excitation levels, by the concentration of hole traps N_t for the case of saturated traps ($p_0 \gg N_t$) and by the diffusion length of electrons (L_d). The excess electrons are able to escape to the metal substrate only from the distance comparable with their diffusion length inside the metal oxide layer. Therefore, for the ultrathin layer, the initial distribution of trapped holes in the case of homogeneous illumination, small excitation level, homogeneous distribution of traps can be described by:

$$p(x, t = 0) = \frac{p_0}{1 + \exp\left(\frac{x}{L_d}\right)} \quad (1.4.1)$$

The thickness of the space charge region in the metal is negligible due to the high concentration of charge carriers there.

As a result of the spatial separation of excess charge carriers, a light induced electric field arises between the separated charge and the respective potential difference is the photovoltage appearing between the free surface of the metal oxide and metal substrate (positive trapped charge and negative mirror charge). The value of the photovoltage can be found by the double integration of the Poisson equation:

$$U(t) = \frac{e}{\epsilon\epsilon_0} \int_0^d dx \int_0^x p(y,t) dy \quad (1.4.2)$$

where $\epsilon_0 = 8.85 \cdot 10^{-12}$ F/m, and e , ϵ are the elementary charge and dielectric constant of the metal oxide layer, respectively.

1.4.3 Role of tunnelling for the PV decay

Only deep traps ($E_t \gg kT_0$, where k – Boltzmann constant, T_0 – room temperature) are considered in the model. Detrapping (emission) of the trapped holes can be neglected for the deep traps at low temperatures. Taking into account, that the band offset at the metal oxide/metal interface $\Delta W \gg kT_0$, the thermal surmounting of the interface barrier by electrons can also be neglected. Therefore, the distance between separated trapped holes and electrons in the metal is fixed. The decay of the PV signal for unchangeable distance between a fixed charge occurs due to the decrease of the excess charge carrier concentration $p(x,t)$ in time. The relaxation of the PV due to the recombination of spatially separated charge carriers (spatially dependent recombination) can be discussed in this case. The recombination of spatially separated charge carriers is a well known mechanism of recombination in the presence of macroscopic barriers between charge carriers. Whenever spatially dependent recombination of excess charge carriers takes place, for example, distance-dependent donor-acceptor recombination³⁹ or recombination between the free electrons and localized centers by means of tunneling,⁴⁰ the overlap of the electron and hole wavefunctions (Fig.1.13) determines the recombination rate:

$$\frac{dp(x,t)}{dt} = -\frac{p(x,t)}{\tau} \exp\left(-\frac{2x}{a}\right) \quad (1.4.3)$$

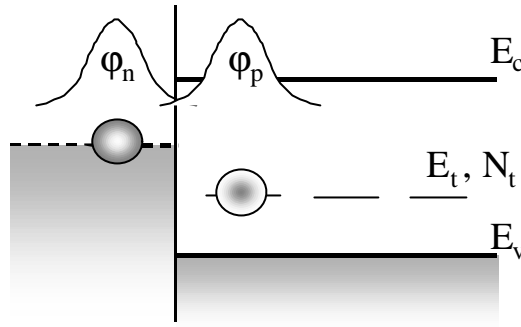


FIG.1.13: The overlap of the wavefunctions of excess electron located in the metal and hole trapped in the metal oxide in spatially dependent recombination.

where $p(x,t)$, τ and a are the excess hole concentration, lifetime without spatial separation and Bohr radius of the trapped holes. The initial condition $p(x,t=0) = p_0$, where p_0 is a constant, will be used in the range $0 < x < d$ if assuming for the ultrathin samples that $d < L_d$.

The time dependent photovoltage signal can be found by substitution of the solution of (1.4.3) into (1.4.2) and integrating twice the Poisson equation:

$$U(t) = \frac{e}{2\epsilon\epsilon_0} \int_0^d dx \int_0^x p(y,t) \exp\left[-\left(\frac{\tau}{t}\right) \exp\left(-\frac{2x}{a}\right)\right] dy \quad (1.4.4)$$

This expression can be analytically integrated in the case of $t \gg \tau$ (so-called sharp-front approximation,³⁸ the detailed integration procedure is described in Appendix A) and the PV transient is given by

$$U_{pv}(t) = \frac{e}{2\epsilon\epsilon_0} p_0 d^2 \left[1 - \left(\frac{a}{2d}\right)^2 \ln^2\left(1 + \frac{\tau}{t}\right) \right] \quad (1.4.5)$$

Therefore, the PV signal depends on the parameters p_0 , a and τ . The results of simulations of the PV transients are given in Figure 1.14 and Figure 1.15 for a set of values of the Bohr radius of trapped holes a , $2a$, $3a$ or initial hole concentration p_0 , $2p_0$, $3p_0$, respectively and constant value of lifetime of charge carriers without spatial separation τ . The PV amplitude of $U_{pv}^{amp} = ep_0 d^2 / 2\epsilon\epsilon_0$ for $t \sim \tau$ uniquely determines the

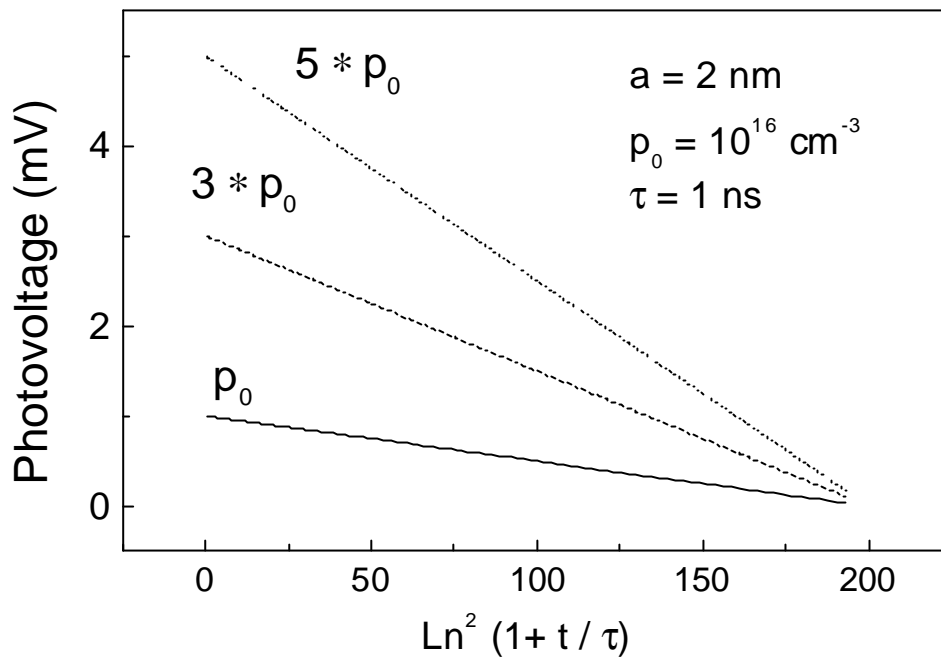


FIG.1.14 Simulated PV transients (after (1.4.5)) for a constant lifetime of charge carriers (t) without spatial separation and Bohr radius of trapped holes (a). The initial trapped hole concentration is the parameter.

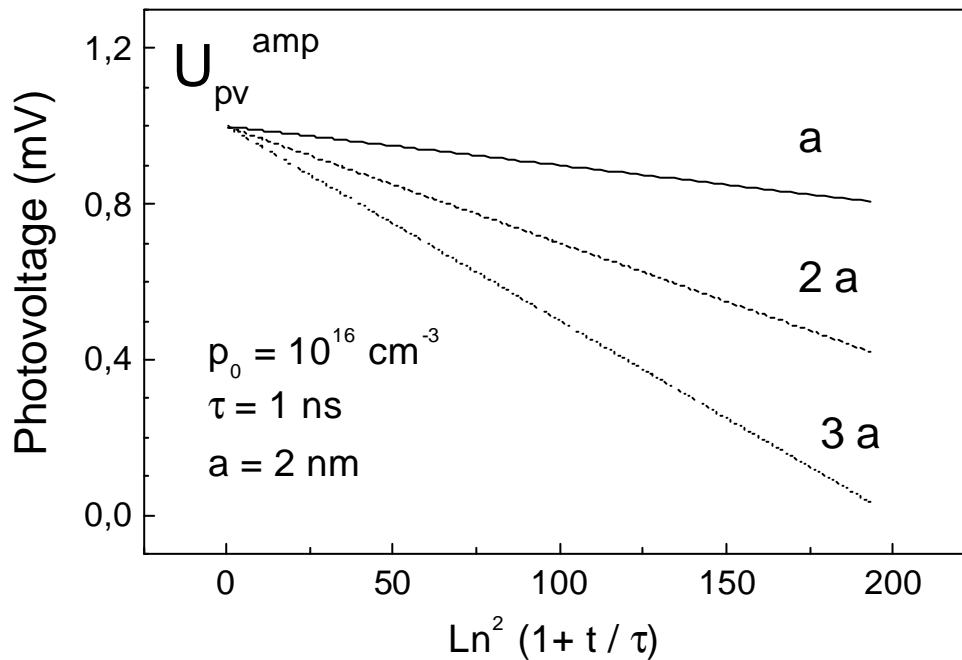


FIG.1.15 Simulated PV transients (after (1.4.5)) for a constant lifetime of charge carriers (t) and initial trapped hole concentration (p_0). The Bohr radius of trapped holes is the parameter.

trapped hole concentration p_0 . The slope of the PV transient for $t > t$ (in units of $Ln^2(1+t/t)$) decays linearly, while its value is determined by the Bohr radius a for a given p_0 .

1.4.4 Role of thermal emission for the PV decay

For increasing temperatures ($kT \sim E_t$), the recombination is accelerated due to the thermal emission of holes and their movement toward the interface (Figure 1.16). The band offset at interface ΔW , for example for Ti/TiO₂, is about 1.3 eV⁴¹ what is much larger than the value of kT at the range of the used experimentally temperatures. Therefore, the thermal overcoming of the interface barrier by electrons can be neglected and thermal emission of trapped holes can be considered. The rate of the thermal emission of holes from the traps is proportional to the number of trapped holes:

$$\frac{dp(t)}{dt} = -s_p v_T n_1 \cdot p(t) \quad (1.4.6)$$

where $n_1 = N_v \exp(-E_t/kT)$, s_n – thermal cross-section of trap, v_T – thermal velocity of hole, N_v – effective density of states in the valence band.

The solution of this equation is given by

$$p(t) = p_0 \cdot \exp\left(-\frac{t}{t_{TE}}\right) \quad (1.4.7)$$

where the definition of the thermal emission time t_{TE} is introduced:

$$(t_{TE})^{-1} = s_p v_T N_v \exp\left(-\frac{E_t}{kT}\right) \quad (1.4.8)$$

Our consideration is valid if retrapping of the emitted charge carriers can be neglected. It is reasonable for low trap concentrations and/or thin metal oxide layer.

The simple superposition of the process of (i) spatially dependent recombination and (ii) thermal emission of carriers is possible while exponential function does not perturb the logarithmic decay at shorter times ($t < t_{TE}$) and decays much faster at longer times ($t > t_{TE}$).

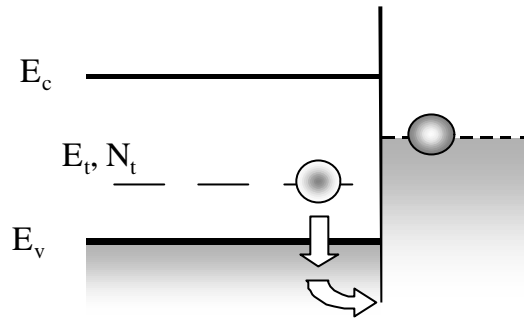


FIG.1.16 Thermal emission of trapped holes and recombination at the interface with excess electrons in the metal substrate.

The resultant PV transient which takes into account spatial recombination and thermal emission of charge carriers can be fitted if exchanging p_0 in equation (1.4.5) by $p(t)$ from (1.4.7).

CHAPTER 2 Experimental

2.1 Experimental methods

Nanoscale materials have a huge surface-to-volume ratio due to the characteristic geometrical sizes of the spatial elements in the nanometer range. Their optical and transport properties are frequently determined by the surface conditions. Therefore, contactless approaches of experimental methods become an important requirement for their investigation. A number of contactless experimental techniques were designed to measure the surface potential and its change under illumination for crystalline materials. Contact potential difference ⁴² (CPD) method (also known as Kelvin probe), electron beam technique (EB) ^{43,44} and Surface PV (also known as Metal – Insulator – Semiconductor) technique ¹⁰ are the most commonly used contactless method. CPD measures the surface potential with respect to the workfunction of the reference electrode. Charge redistribution between two materials with different workfunctions charges the sample - air slit - reference electrode capacitor. The vibration of the reference electrode causes an *ac* current in the external circuit, which depends on the workfunction difference of sample and reference electrode. The oscillation frequency of the reference electrode in the range of several

Hz determines the time resolution of the CPD method. An essentially faster time response has the EB technique. A vacuum diode is formed by an electron gun as a cathode and the sample as the anode. The current in the external circuit is a monotonous function of the applied voltage and the workfunction difference of the cathode gun and the sample. However, the application of this technique is strongly restricted to vacuum ambience. The SPV technique has the advantage of comparable time resolution with EB what is essentially faster in comparison to CPD, and of operation in different ambient conditions. Therefore, it seems to be a promising method to investigate transport (time resolved features of PV) and optical (spectral features of PV) properties of nanoscale materials.

Transient SPV was firstly investigated by O.E. Johnson,¹¹ and its spectral modification was applied by Goodman.¹² The appearance of fast light sources (laser, for example) and registration devices enlarged the experimental possibilities via extension of the time range of measurements. The combination of SPV with spatial scanning methods improved its spatial resolution up to a range of 200 nm for Kelvin Probe Force Microscopy,⁴⁵ and to atomic level for Scanning Tunneling Microscopy.^{46,47} Nowadays the SPV and other modifications are well developed experimental method with a strong interpretation methodology for crystalline semiconductors.⁹

In this chapter, the experimental realization of the SPV method will be described in details. Several additional experimental techniques which were used in the work as accomplished will be also mentioned.

2.1.1 Principle of SPV operation

Photovoltage measurements were performed in a fixed parallel plate capacitor arrangement. The basic cell for the measurements (Figure 2.1) consists of the semitransparent Cr electrode (transparency of about 70%, diameter $d = 5$ mm) evaporated on a quartz homogenizer, mica spacer (thickness $d_m = 50$ μm) and sample layer on the conductive substrate (reference electrode). The quartz homogenizer is not only the mechanical support for the Cr electrode but homogenizes the light spot in order to avoid shunting capacitance of unilluminated areas, which decreases the PV signal. The PV signal is registered by an oscilloscope or lock-in amplifier from Cr electrode as a voltage drop on a load resistor R . A high - impedance buffer agrees the high output impedance

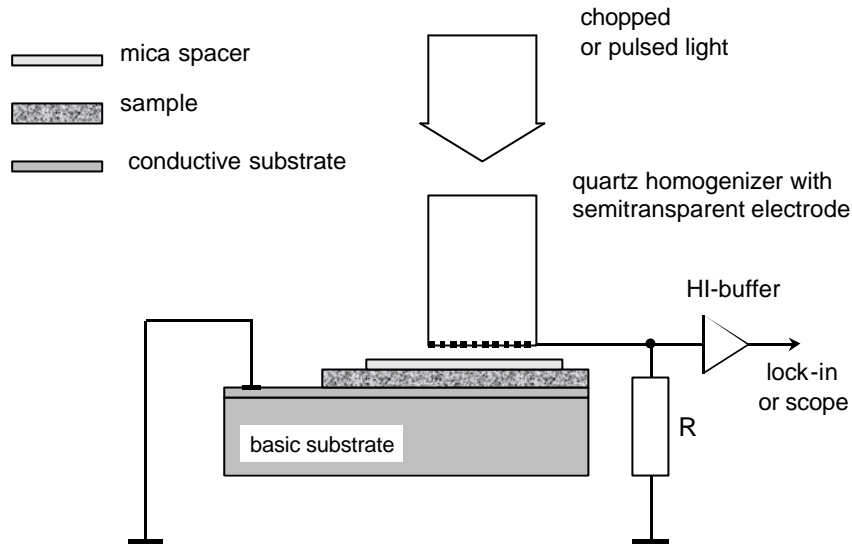


FIG. 2.1: Basic cell for PV measurements.

of the sample and the low impedance of a measurement device. The preamplifier input impedance should be high compared to that of the capacitance that couples the signal electrode to the specimen at the frequency corresponding to the inverse of the specimen lifetime.

2.1.2 Equivalent circuit of the PV cell

The equivalent circuit of the basic cell for the PV measurements is shown in Fig. 2.2. The PV signal, mica spacer and load resistor are represented as serial connection of a voltage source $U_{pv}(t)$, capacitance C , and resistor R .

The Kirchhoff's laws for the equivalent circuit yield an equation for the charge on the capacitor $q(t)$:

$$U_{pv}(t) + \frac{q(t)}{C} + R \frac{dq(t)}{dt} = 0 \quad (2.1)$$

with general solution:

$$q(t) = A e^{-\frac{t}{RC}} - \frac{1}{R} e^{-\frac{t}{RC}} \int U_{pv}(t) e^{\frac{t}{RC}} dt \quad (2.2)$$

where A is the arbitrary constant.

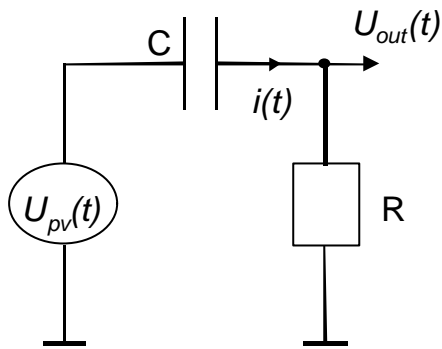


FIG.2.2: Equivalent circuit of measurement cell

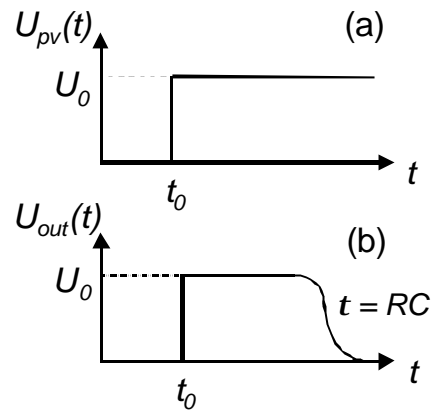


FIG.2.3: Input (a) and output (b) voltage pulses

The initial condition for (2.1):

$$q(t=0) = 0 \tag{2.3}$$

and the input voltage $U_{pv}(t)$ (Fig.2.2(a)):

$$U_{pv}(t) = \begin{cases} 0, & t < t_0 \\ U_0, & t > t_0 \end{cases} \tag{2.4}$$

cause an output voltage response $U_{out}(t)$ (Fig.2.2(b)) as:

$$U_{out}(t) = R \frac{dq}{dt} = U_{pv}(t) e^{-\frac{t}{RC}} \tag{2.5}$$

The time scale of measurements is not limited by the measurement cell to short times but is limited by the charging of the capacitor C via the load resistor R with time constant $t = RC$ to long times.

2.1.3 Voltage response measurements

The time range of PV measurements was experimentally examined by substitution of the voltage pulse generator (HP 214 B) instead of the sample (see equivalent circuit). Fig. 3.4 compares the voltage pulse of the generator (dot lines) and the voltage pulse after capacitive circuit and high-impedance buffer (solid lines) measured by HP 54510B

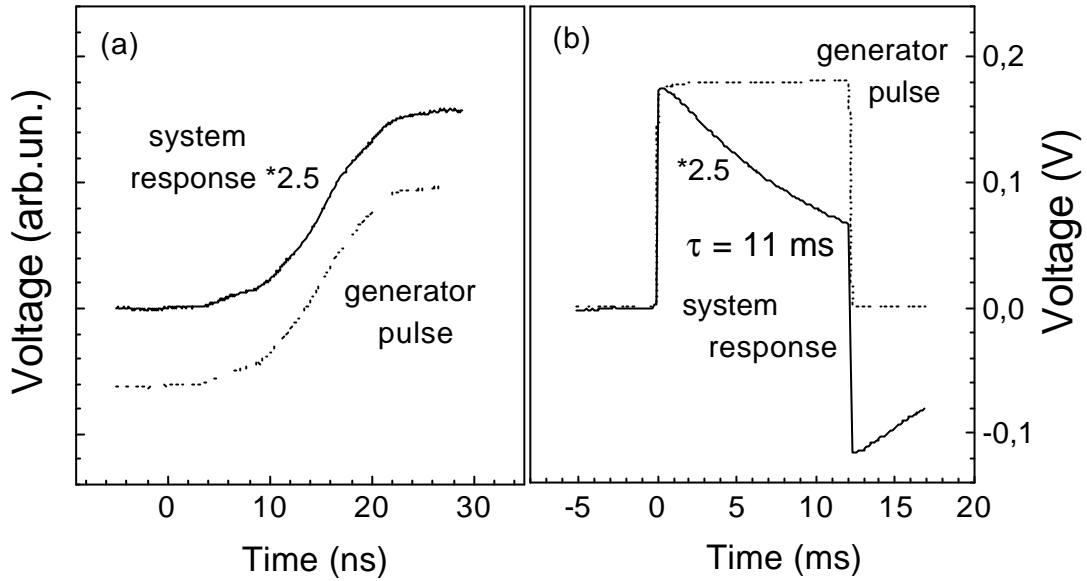
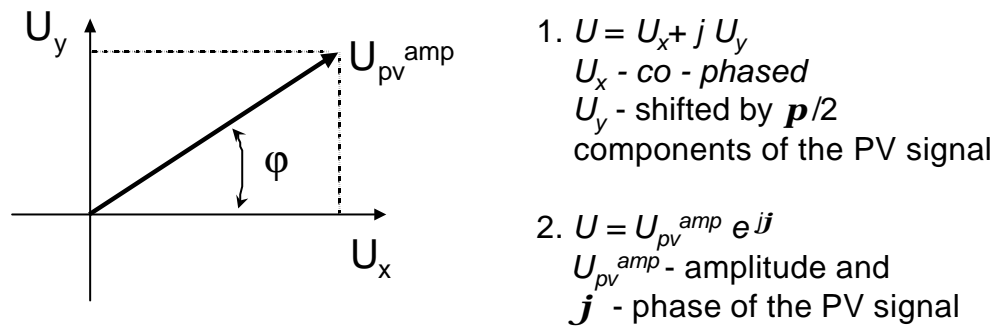


FIG. 2.4: Comparison of the input voltage pulse (after voltage pulse generator) and output one measured by PV cell at shorter (a) and longer (b) times.

oscilloscope. No change of the shape of voltage pulse introduced by the capacitive circuit and high-impedance buffer (900 MHz) was observed for short times, the time resolution is determined by the frequency band of the oscilloscope (300 MHz) and estimated as 1-2 ns. The experimentally obtained discharging time $\tau = 11$ ms of the RC circuit is in good agreement with the calculated one for the used load resistor $R = 1$ GW and capacitance of a mica layer $C = \epsilon_m \epsilon_0 S/d_m = 12$ pF (ϵ_m - permittivity of mica). The amplitude of the signal after PV cell 2.5 times smaller because of the distribution of the output voltage between output resistor of the HI - buffer 75 W and input resistor 50 W of the oscilloscope. All measured PV transients will be multiplied with coefficient 2.5. The PV spectra will be normalized to the photon flux and in this case given in the arbitrary unit scale.

2.1.4 Chopped signal control

Spectral photovoltage was excited by CW illumination and chopped with a frequency f_{ch} in the range from 100 Hz to 1000 Hz. A two channels lock-in amplifier was used for the spectral PV measurements. Co - phased and phase shifted by $\pi/2$ photovoltage signals with respect to the chopped light were denoted as U_x and U_y signals, respectively.



$$\text{where } |U_{pv}^{amp}|^2 = U_x^2 + U_y^2 \quad \text{and } \mathbf{j} = \arctg U_y/U_x \pm n\pi, \quad n \hat{\mathbf{I}} Z$$

FIG.2.5 Representation of the PV signal on a complex plane: co-phased and shifted by $\pi/2$ components or amplitude and phase.

Figure 2.5 shows the standard representation of a signal with amplitude U_{pv}^{amp} and its phase shift \mathbf{j} with respect to the reference signal in the complex plane. The signal of a reversibly biased silicon photodiode was used for the calibration of the initial phase of the lock-in amplifier. The transient PV signal of the photodiode under a N_2 laser pulse (FWHM = 5 ns) illumination has a negative sign and follows the shape of the laser pulse. Its PV spectra have a negative U_x signal and $U_x \gg U_y$. Some data will be presented as normalized amplitude $U_{ph}^{amp} / \mathbf{F}$ and phase φ of the PV signal (Fig.3.5). The PV spectra are measured in the regime of weak excitation when U_{ph}^{amp} depends linearly on the photon flux \mathbf{F} (excitation intensity divided by $h\nu$).

The increase (decrease) time of the PV after switching on (off) the illumination will vary in a wide range with respect to the chopper frequency. An example of the measurements of the co-phased and shifted by $\pi/2$ with respect to reference pulse voltage signals is shown in Fig.2.6. The PV signals of different sign and duration are simulated by the voltage pulses from the generator (test pulses). The repetition period and duration of the reference pulses (solid line) are 2 ms and 1 ms, respectively. The test voltage pulses have positive (a,c) or negative (b,d) sign and shorter (a,b) or longer (b,d) duration (dot lines). The sign of U_x component corresponds to the sign of the test voltage pulse. The U_y - signal characterises the phase shift between the reference pulse and the test signal. An essential U_y signal points to a slow increase and decrease of the test signal in comparison to the period of the reference signal.

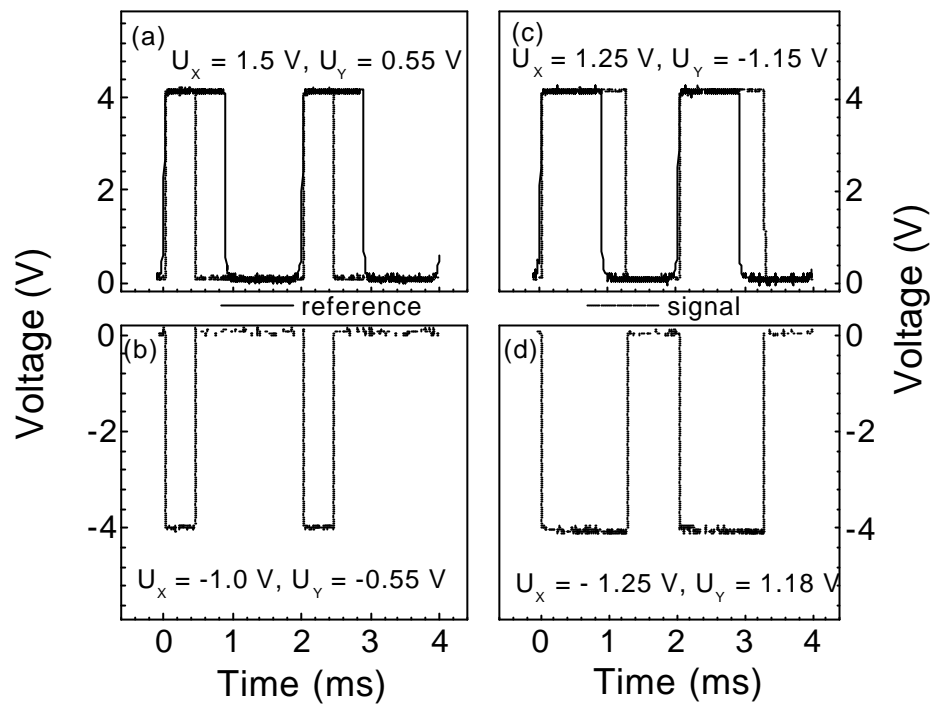


FIG.2.6: An example of simulations of the PV signal by the voltage pulses from the pulse generator of positive (a,c) or negative (b,d) sign with shorter (a,b) or longer (c,d) pulse duration than the reference one (solid curve, period 2 ms, filling factor 0.5). U_x and U_y are the voltage values of the two channels of lock-in amplifier.

2.1.5 Vacuum and gas ambience, control of temperature

The experimental setup for the transient and spectral PV measurements is shown in Fig. 2.7. The samples were placed on the table of the vacuum chamber which was designed for the measurements in vacuum and different gas ambiances. The vacuum was changed between 10^{-4} and 10^3 mbar by using a system of vor-vacuum pump (Pfeiffer vacuum, type DUO 016B) and turbo-pump (Pfeiffer vacuum, type TPU 240) and controlled by the digital vacuum measurement unit (Pfeiffer vacuum, Gauge TPG 256). The location of the specimen in a shielded box well isolated from shocks and vibrations is crucial for the PV measurements. The vacuum chamber screens the PV cell from ambient electric fields, the additional screening of all wires inside the chamber was made by Al foil.

The vacuum chamber was in good thermal contact with the reservoir of liquid nitrogen. The thermo - resistor and a Pt 100 resistor were built-in inside the table. This combination allowed to measure in a temperature range of 80 – 700 K. The external power controller for the thermo-

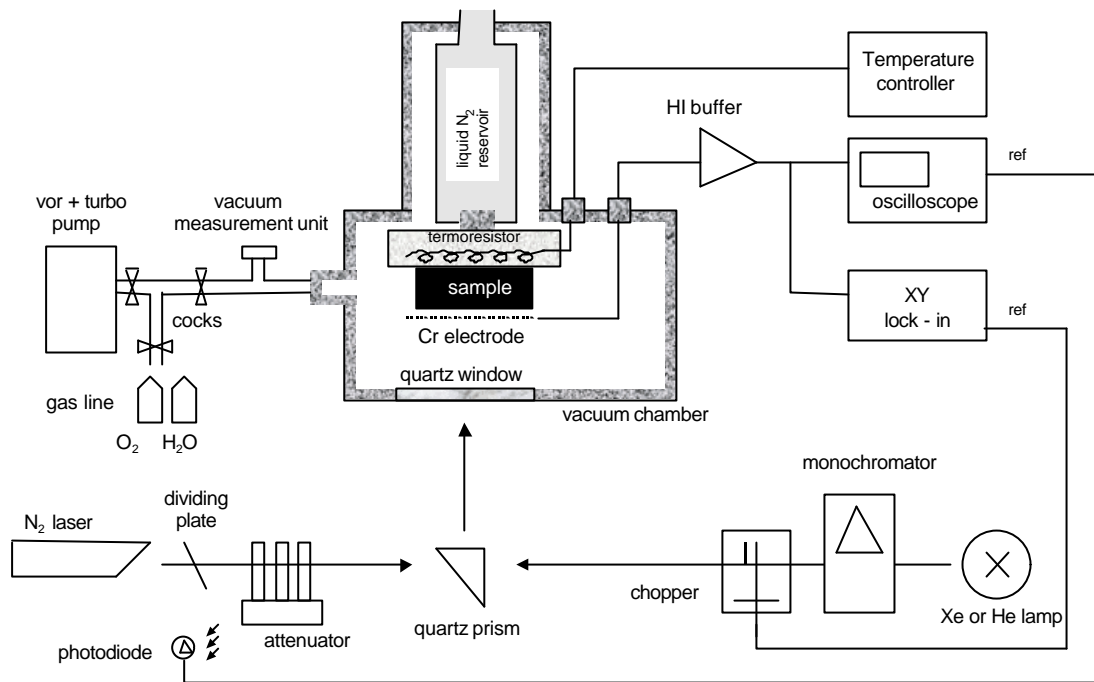


FIG. 2.7 Schematic picture of the experimental setup for transient and spectral PV measurements.

resistor (1/16 DIN Plastics Controller) with a Pt100 resistor kept the temperature of the table with a precision of < 1 K.

Two N_2 lasers (wavelength 337 nm) with different duration times of a pulse 0.3 ns or 5 ns were used for the excitation of PV transients. The maximal energy density per pulse were 10 μ J and 300 μ J, respectively. A dye - laser with adjustable wavelength and intensity maximum at 440 nm was used with optical pumping by the N_2 laser. Attenuation of the excitation intensity was made by a set of calibrated neutral glass filters. The spectral PV was excited by a 1000 W Xe lamp in the UV range or by a tungsten 150 W lamp in the IR range with quartz prism monochromator (SPM2, Carl Zeiss Jena). Quartz optics (deflection prisms, quartz window of the vacuum chamber) allowed optical measurements up to 4.5 eV. Ge or Si photodiodes with known spectral sensitivity were used for the measurements of incident intensity and subsequent normalization of the PV spectra on the photon flux. The linear regime of the photodiode was controlled.

Measurements of the PV transients were made by HP 5150B oscilloscope (bandwidth 300 MHz) and of the PV spectra by two

channels lock-in amplifier (EG&G Princeton Applied Research, Model 5210).

2.1.6 Subsidiary method

DC current - voltage (I-V), Impedance spectroscopy (IS), Fourier Transform Infra Red (FTIR) spectroscopy, Optical Transmittance (OT), X-ray diffraction (XRD), Raman spectroscopy (RS) measurements were applied for the characterization of the samples.

The I-V measurements were carried out in diode like structures Au/porousSi/p⁺- Si to get information on the dc electrical conductivity of the porous Si layers at different temperatures. The I-V characteristics were measured with a HP 4140 B digital pA-meter with a step like applied potential with a sweep time of 1 s in order to decrease charging effects. The I-V measurements at different temperatures were performed in the same vacuum chamber with temperature control as used for the PV measurements for the direct correlation with the PV measurements.

The IS measurements were performed in a sandwich-like geometry of a graphite/porousTiO₂/SnO₂:F structure to get information about the change of the dc electrical conductivity and capacitance in air, vacuum, or water vapors ambiances. A HP 4192A LF impedance analyzer with the frequency range 5 Hz – 13 MHz was used for the IS measurements.

FTIR spectroscopy was made using a BOMEM DA-3 FTIR spectrometer in the transmittance mode to detect chemical bonds covering the internal surface of the free-standing porous Si samples just after preparation, thermal oxidation or etching.

Optical transmittance measurements were performed to measure the absorption and scattering coefficients of the nanoporous TiO₂ layers on a quartz substrate and compare them with the spectral dependence of the PV. Tungsten or Xe lamps with a quartz prism monochromator for light illumination in the range of 0.7 – 4 eV were used as light sources and Si or Ge photodiodes in a liner regime were used to record the transmittance signal.

The average size (L) of the TiO₂ nanoparticles was determined from the broadening of the peaks in the angular x-ray diffraction dependence, using the Debeye-Scherrer equation $L = 0.9 (\lambda / \cos\theta \Delta\theta)$, where $\lambda = 0.154$ nm (Cu K_a line), θ is the Bragg angle, and $\Delta\theta$ is the full width of peak at the half maximum.

Raman spectra were measured at room temperature on a visible

Renishaw Ramanscope spectrometer using the 514.5 nm line of an Ar laser as excitation source. The Raman spectra were acquired over the range of 100–2000 cm^{-1} at 1 cm^{-1} resolutions. The laser spot size, laser power, and the acquisition time were set to 1 mm, 50 mW, and 150 s, respectively.

2.2 Nanoscale materials

Several materials, such as porous Silicon, poly(p-phenylene vinylene), sintered TiO_2 layers, ultrathin anodic TiO_2 layers, natively oxidized ZnO layers, thermally oxidized Cu_2O layers were used for the investigation of PV phenomena in nanoscale materials. The nanometer range of the characteristic dimensions, like a pore size for porous material, polymer chain length for organic polymer or thickness of the layers for ultrathin metal oxide films gives the general definition as “nanoscale materials” for these objects.

2.2.1 Porous silicon

A well defined porous matrix of porous material can be obtained by anodization of crystalline silicon. A set of preparation parameters, as type, crystallographic orientation and doping level of the substrate, anodization current and time, and composition of the electrolyte allows one to create porous materials of different morphologies, to change the porosity and size of nanocrystals, thickness of the porous layer.⁴⁸ Porous silicon (PS) samples were prepared from p - Si (100) substrates with resistivities in the range from 0.005 to 5 $\Omega \text{ cm}$ by anodization in $\text{HF}:\text{C}_2\text{H}_5\text{OH}:\text{H}_2\text{O}$ (1:2:1) solution at a constant current density (values within the range from 50 mA/cm^2 to 200 mA/cm^2) for 20 min. Every specific set of preparation parameters will be given during the description of the experimental results. Free - standing PS films were lifted by rapid increasing the anodization current above one order of magnitude for a short time at the end of the anodization procedure. The area of the porous layer was 0.8 cm^2 what is larger than the area of the PV electrode (0.2 cm^2) in order to suppress effects due to lateral inhomogeneity of the samples. Special attention has been paid to the post anodization conditions in order to fix the experimental conditions and to reach a good reproducibility. It should be remarked, that changes of the surface conditioning of the Si nanostructures are crucial during the

experiments. All PS samples were rinsed in distilled water for 2 s and dried in air for 30 min before the measurements. All measurements were done within a few hours after the anodization procedure supposing unchanged surface conditions if particular treatments were not applied.

The structural properties of PS are well - tabled for a standard sets of preparation parameters. With respect to the literature,⁴⁸ the thickness of the PS films was about 50 μm , the porosity of the samples varied in the range of 45 - 85 % for different samples depending on the used conditions.

2.2.2 Poly(p-phenylene vinylene)

Poly(p-phenylene vinylene) samples were prepared by doctor-blade technique.⁴⁹ The main steps of preparation procedure are shown in Figure 2.8. The parent 1,4-bis(chlormethyl)benzol after reaction with tetrahydrothiophen produces bissulfonium acid. The dissolved bissulfonium acid in methanol (methanol/water or aceton/water) is

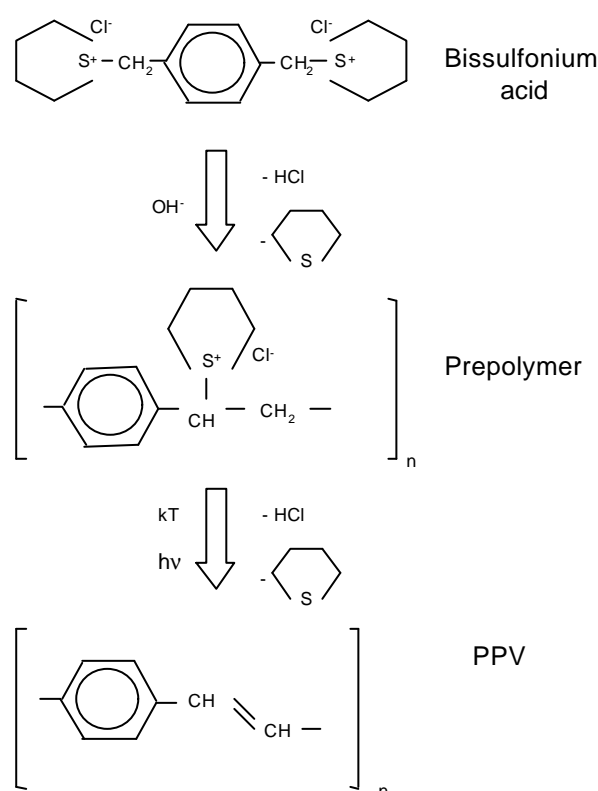


FIG.2.8: Schematic synthesis way of PPV

polymerised in NaOH (or LiOH) bases. The neutralisation of the excess base is reached through the addition of hydrochloric or acetic acids. By means of the dialysis with deionized water the rest waste products are separated. The methanol solution with the prepolymer (concentration : 0.01 – 0.1 %) is pasted as a thin film on the indium – tin – oxide (ITO) coated glass substrates (Flachglas firm, 300 nm thickness, resistivity 20 $\Omega/$) and dried in laboratory conditions. Since the polyelectrolyte precursor has a high molecular weight, even diluted solution exhibits a high viscosity which is necessary for film formation. The thermal conversion of the tetrahydrothiophene (THT) - precursor prepolymer films at 120 – 180 °C for 2-3 hours in the evacuated glass vessel (10^{-3} mbar) leads to the removal of HCl - gas and to the converting it into PPV. The thickness of one PPV layer which was measured with a step profiler is about 90 nm. Samples of three thicknesses (90 nm , 290 nm and 780 nm) were fabricated by layer-by-layer method.

The layers of poly(p-phenylene vinylene) (PPV) were synthesized in “Kristall und Materiallabor” of Bayreuth Institute for Macro-molecule investigation (BIMF) by J.Gmeiner. Details of preparation and characterization procedures one can find in Ref.[49](#).

2.2.3 Metal oxide layers

Layers of TiO₂, Cu₂O and ZnO were prepared at Ti, Cu and Zn substrates, respectively. The TiO₂ layers were obtained by anodic oxidation in the galvanostatic regime in a 0.5 M H₂SO₄ electrolyte and a current of 1 mA/cm² was supported until the final voltage U_0 was reached. The thickness d of the anodic layers is determined by U_0 and controlled by ellipsometrical measurements.^{[50](#)} A set of samples with thickness from 5 nm to 200 nm was prepared for U_0 from 3 V to 255 V, respectively. Copper oxide was prepared by thermal oxidation of Cu at 150 °C for 2 hours (growth rate about 5 nm/h^{[51](#)}). The ZnO was formed by prolonged native oxidation at room temperature. The thicknesses of the Cu₂O and ZnO layers were estimated as 10 and 3 - 6 nm, respectively.

Scanning Electron Microscopy (SEM) and Raman spectroscopy were used to characterise the anodic TiO₂ layers of different thickness. Figure 2.10 presents SEM images of 20 nm (a), 80 nm (b) and 200 nm (c) thickness anodic TiO₂ layers. The images show the continuous layer of 20 nm thickness, early stage of pore formation for 80 nm and highly porous

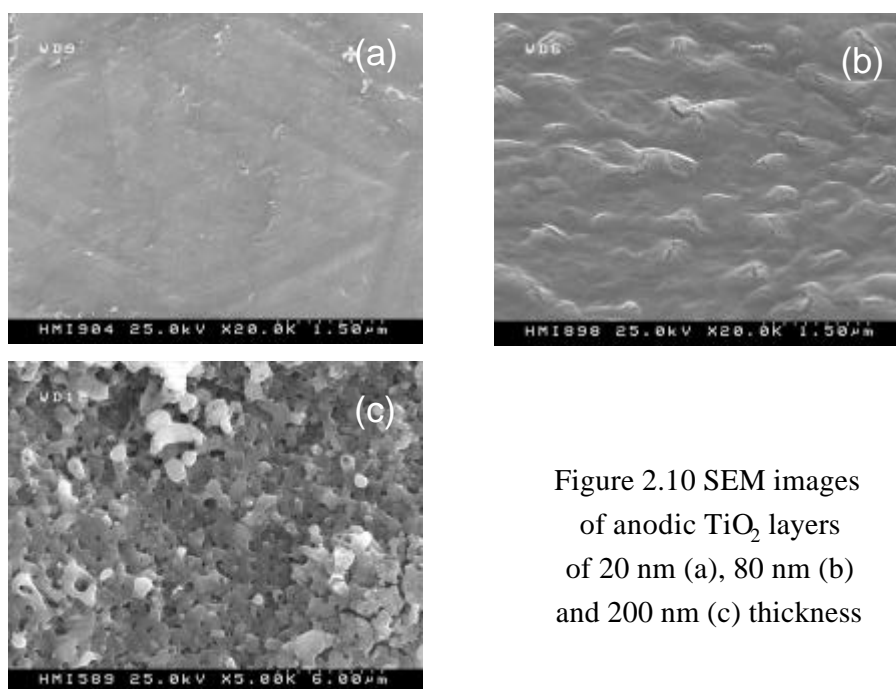


Figure 2.10 SEM images of anodic TiO₂ layers of 20 nm (a), 80 nm (b) and 200 nm (c) thickness

TiO₂ layer for 200 nm. The porous layer has continuous morphology with the large size dispersion of nanoparticles from 100 nm to 1 μm. Raman spectra of ultrathin anodic TiO₂ layers of two thicknesses ($U_0=18$ V and $U_0=80$ V) are shown in Fig.2.11(a). Four peaks at 145 cm⁻¹ and 640 cm⁻¹ (E_g), 399 cm⁻¹ (B_{1g}), 516 cm⁻¹ (doublet A_{1g} and B_{1g}), which are assigned to the anatase phase of TiO₂⁵² are well resolved.

2.2.4 Sintered porous TiO₂ layers

Different pastes containing TiO₂ nanocrystals of anatase or rutile (INAP GmbH) are used for the preparation of nanoporous TiO₂ layers. The glass substrates are covered with a transparent conducting SnO₂:F layer. The nanoporous TiO₂ layers are prepared by screen printing of the paste on the substrate and subsequent firing at 450°C in air for 30 min. The thickness of the TiO₂ layer is typically $d = 4$ μm for the samples used in the PV experiments. Some control experiments are carried out on samples with d from 0.5 to 12 μm.

The TiO₂ nanoparticles of different samples are characterized by Raman scattering (Figure 2.11(b)) and by x-ray diffraction (Figure 2.12). Characteristic modes appear in the Raman spectra at 143 cm⁻¹ (B_{1g}), 447 cm⁻¹ (E_g), and 612 cm⁻¹ (A_{1g}), which are well known for crystalline

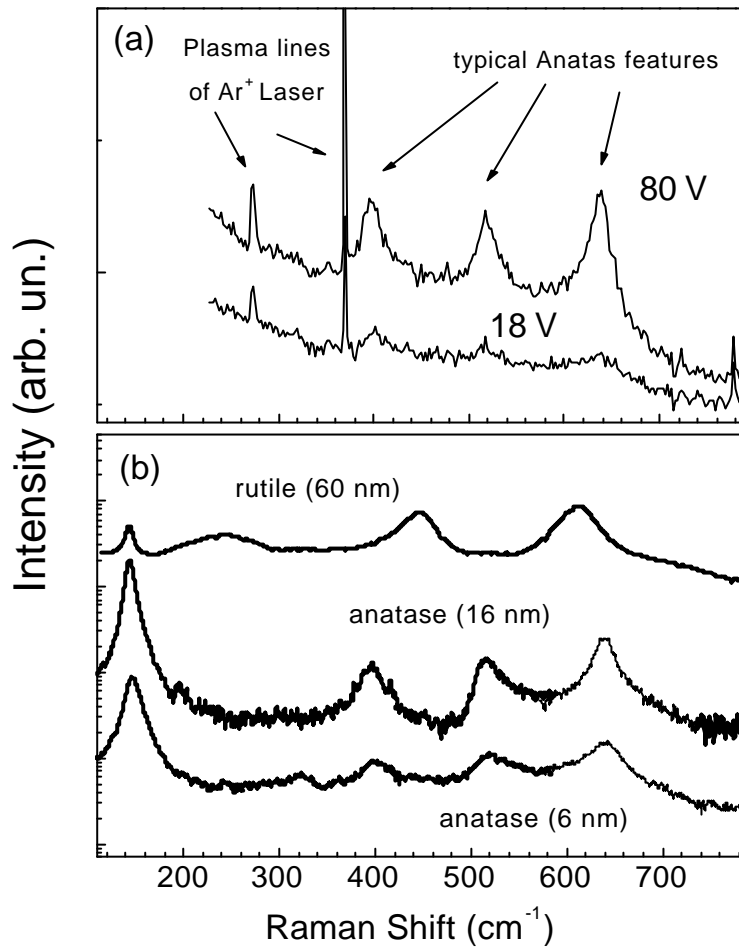


FIG.2.11: Raman spectra of anodic TiO_2 layers (a) for two values of U_0 and sintered nanoporous TiO_2 layers (b) of different crystalline phase and size of nanoparticles.

rutile,⁵³ and at 145 and 640 cm^{-1} (E_g), 399 cm^{-1} (B_{1g}), 516 cm^{-1} (doublet A_{1g} and B_{1g}), which coincides with Figure 2.11(a) and is assigned to the anatase phase of TiO_2 .⁵² The third E_g mode at 198 cm^{-1} which is well resolved for anatase single crystals as a small narrow peak⁵⁴ is seen only slightly for the nanoporous TiO_2 layer of anatase (16 nm) but not for the nanoporous TiO_2 layer of anatase (6 nm). The mode at 198 cm^{-1} disappears also for anodic nanoporous layers of anatase for which disorder is important.⁵⁵

As can be seen from Figure 2.12, the nanoporous TiO_2 layers contain nanocrystals of only one phase. The average size (L) of the nanocrystals is determined from the broadening of the peaks in the angular x-ray diffraction dependence, using the Debye-Scherrer equation $L=0.9\cdot\lambda/(\cos\theta\cdot\Delta\theta)$, where $\lambda = 0.154\text{ nm}$ (CuK_α line), θ is the Bragg

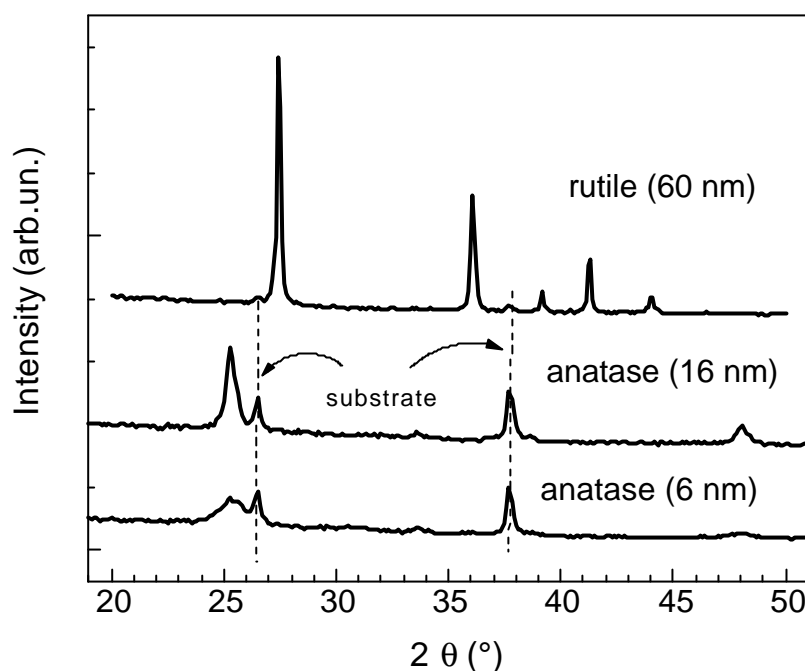


FIG.2.12: XRD picture of sintered porous TiO_2 layers of different crystalline phase (rutile, anatase) and size of nanoparticles.

angle, and $\Delta\theta$ is the full width of peak at the half maximum.⁵⁶ On the basis of this analysis the porous TiO_2 layers of rutile with the diameter of crystallites of 60 nm and of anatase with the diameters of crystallites of 16 and 6 nm are distinguished. These layers are used in the PV experiments and denoted as rutile (60 nm), anatase (16 nm) and anatase (6 nm), respectively.

2.2.5 Geometry of the samples

Figure 2.13 shows the geometry of free-standing porous Si (a), Au/porous Si/ $\text{p}^+\text{-Si}$ (b), graphite/porous $\text{TiO}_2/\text{SnO}_2:\text{F}$ (c), PPV/ITO (d) and TiO_2 (Cu_2O , ZnO)/Ti (Cu, Zn) (e) structures. The free-standing porous Si samples are used in the PV and FTIR measurements. The shape and area of the samples are determined by the electrochemical cell. The axially symmetrical samples have a radius of 0.5 cm independent on the preparation conditions and thickness (L) of about 40 - 60 μm for different anodization parameters. Au/porous Si/ $\text{p}^+\text{-Si}$ structures are used for I-V measurements. The area of the Au electrode (100 nm thick) of 0.13 cm^2 is much smaller than the total area of the porous Si (0.8 cm^2) what allows to measure the current-voltage

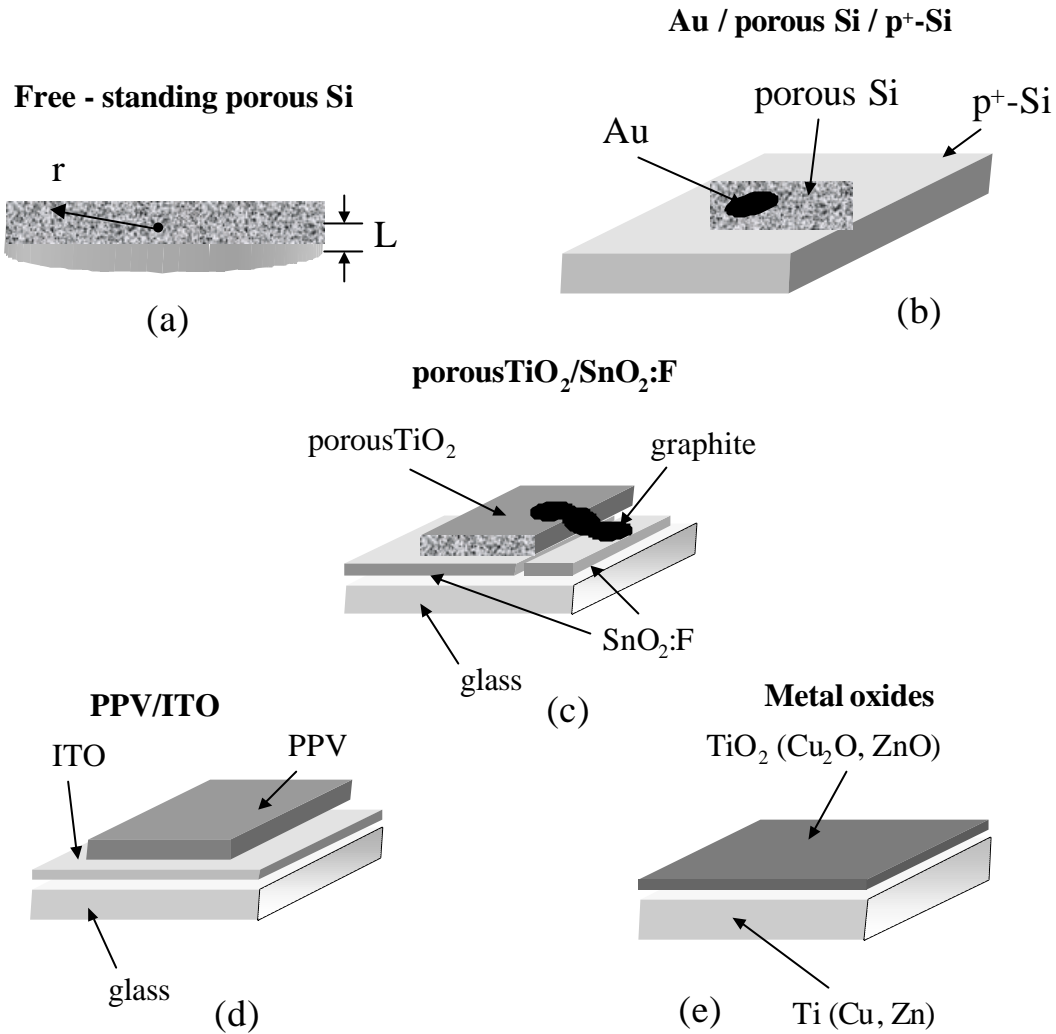


FIG.2.13: Geometry of free-standing porous Si (a), Au/porous Si/p⁺-Si (b), Graphite/porous TiO₂/SnO₂:F (c), PPV/ITO (d) and TiO₂ (Cu₂O, ZnO)/Ti (Cu, Zn) (e) structures.

characteristics and PV transients on the same sample in the same conditions.

Porous TiO₂/SnO₂:F and graphite/porous TiO₂/SnO₂:F (Fig.2.13(c)) structures are used in PV and IS measurements, respectively. The conductive SnO₂:F substrate consists of two parts, separated by the insulating slit. The porous TiO₂ layer is located between one of the SnO₂:F layers and top graphite layer which is in the electrical contact with the second SnO₂:F layer. The typical area of the porous TiO₂ layer is 1 cm² and the thickness is 0.5 – 4 μm (see for details Ref.57). A porous TiO₂ layer of 1 μm thickness on a sapphire substrate is used for the OT measurements.

The areas of PPV/ITO (d) and anodic TiO₂ (thermal Cu₂O, native ZnO)/Ti (Cu, Zn) (e) structures are about 1 cm² and 2 cm², respectively.

The back contact to the Cu experimental table was realized by mechanical pressing of the sample (a, b, e) or via the Cu clamp to the conductive substrate of SnO₂:F (c) or ITO (d).

CHAPTER 3 Drift and diffusion of light induced charge carriers in porous silicon

The surface of a semiconductor is characterized by the electronic states within the forbidden gap. Occupation of the surface states by charge carriers supported from the vicinity of the surface space charge region (SCR) leads to the charge separation in space and hence to the formation of the built-in electric field as a consequence of the Poisson equation. The microstructural topology of a nanoporous material changes the basic properties of the surface SCR in comparison to the crystalline precursor. A nanoporous material consists of a network of constituents with the size in the nanometer range.⁵⁸ A schematic picture of the geometrical surface of porous Si (c,e) and band diagram (d,f) is shown in Fig.3.1 for different degrees of porosity. Charge trapping by surface states of nanoparticles (internal surface states) creates micropotentials within one nanoparticle and changes the macropotential created by surface states of the geometrical surface (external surface states) of a nanoporous material. Illumination of a semiconductor with a photon energy above the bandgap generates excess charge carriers. The redistribution of the excess charge in the electric field of the surface SCR screens the charge of the surface states and surface SCR.

The distance of the spatial separation of excess charge carriers for a

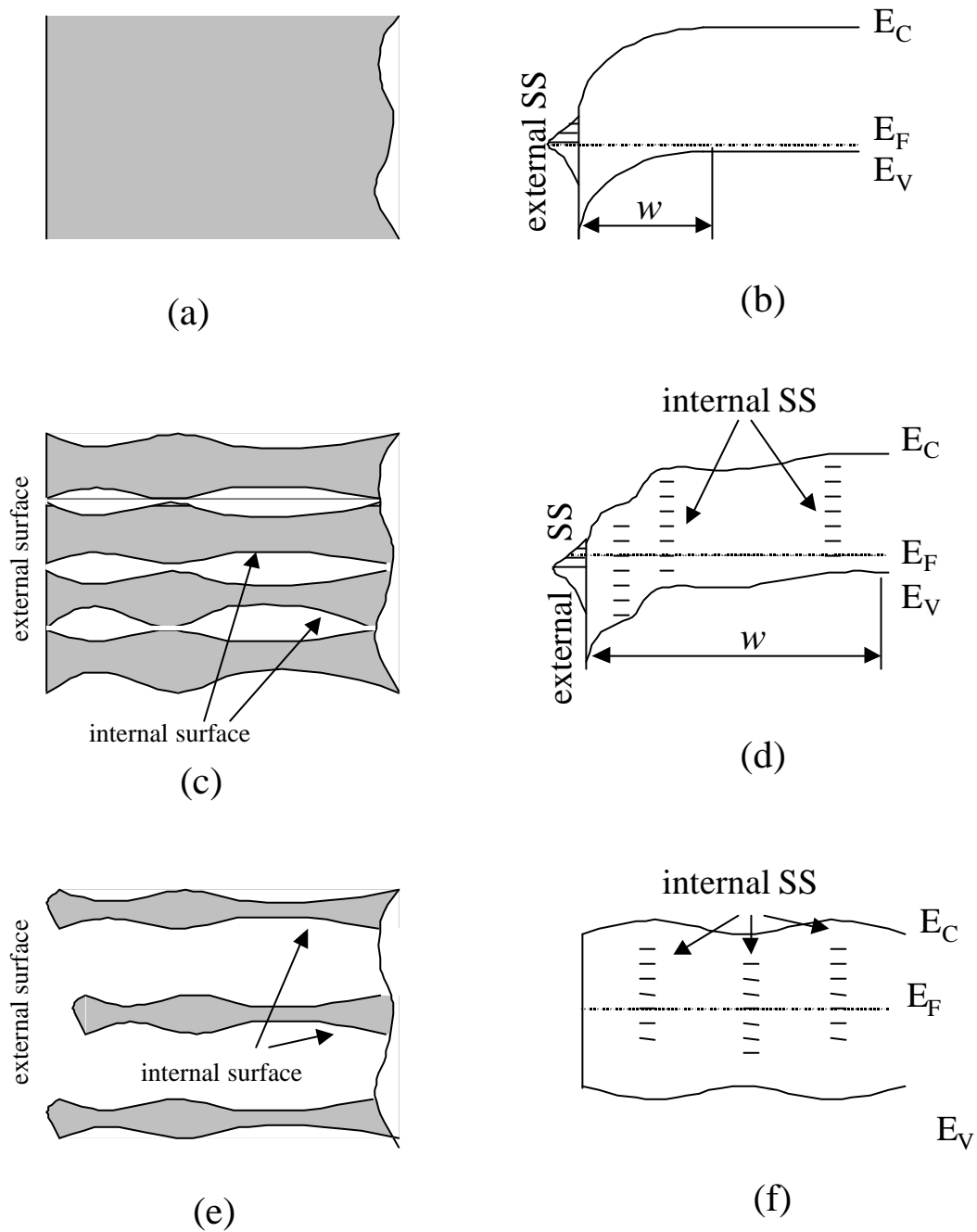


FIG.3.1: Schematic picture of surface geometry and energy band diagram of (a,b) p^+ -Si, (c,d) porous Si of small porosity and (e, f) porous Si of large porosity.

given density and distribution of surface states depends on the concentration of excess charge carriers. The extension of the surface SCR towards the bulk of a semiconductor depends on the concentration of free charge carriers (1.2.13) and is usually much larger than the characteristic size of a nanoparticle of the porous material. At a low illumination intensity and, therefore, at a low excess carrier concentration in comparison to the density of occupied surface states, the excess charge is not able to screen completely the electric field of the surface SCR by separation over the distance of a nanoparticle and separation over many nanoparticles takes place. Transport properties of the nanoporous material play a role in this case.

Transport properties of the porous material are more complicated in comparison to the crystalline precursor because numerous additional factors, like built-in potential within the nanoparticles,⁵⁹ high density of internal surface states⁶⁰ (extremely sensitive to the ambience⁶¹), scattering on the grain boundaries,⁶⁰ size disorder,⁷ different geometrical paths,⁷ are involved. These reasons lead to the essential difference in conductivity and mobility of charge carriers for crystalline materials and its porous derivatives.⁵⁹ The problem becomes more complicated with the decrease of the size of nanoparticles due to the change of the electronic states distribution (quantum confinement effect⁸) and due to the increase of the surface to volume ratio. Change of the transport mechanism is accompanied this transition in porous Si.⁶⁰

Some properties of the surface SCR and charge carrier transport in porous materials can be understood by direct comparison of the PV measurements for a porous material with the crystalline one from which the porous material is made. The advantages of porous Si for the analysis are: (i) transport properties of crystalline Si are well investigated (ii) transition from the bulk to nanoporous material can be made by anodization procedure, which allows to vary the size of nanoparticles in a wide range⁶² (iii) surface states can be easily changed by the oxidation and etching processes.⁶³

In this chapter, we discuss the free carrier concentration in porous Si with large size of nanoparticles (mesoPS, quantum size effect is absent) and investigate the evolution of the surface potential with decreasing nanoparticle size. Thermal annealing will be performed in order to stabilize the surface properties of porous Si. The role of surface states introduced by oxide and size of nanoparticles for charge carrier separation will be investigated. The diffusion mechanism of PV as a

dominating one will be shown for porous Si with small size of nanoparticles (nanoPS, quantum size effect is present). The shape of typical PV transients and the role of the dielectric (Maxwell) relaxation time for the charge carrier separation will be discussed.

3.1 Separation of charge carriers in the electric field of the surface space charge region

Figure 3.2 compares the PV transients of HF-etched p^+ -Si (resistivity $0.01 \Omega\text{cm}$) with as prepared free-standing meso-PS (substrate: p^+ -Si, $0.01 \Omega\text{cm}$, (100) orientation, anodization at 50 mA/cm^2 in 25% ethanoic HF for 20 min). The shape of the exciting N_2 laser pulse is shown for comparison. The PV signals are negative for both samples and arise immediately with the laser pulse. This behaviour is typical for the surface PV in p-type semiconductors with the downward band bending where charge carriers are separated in the electric field of the surface space charge region.⁹ The electric field of the surface SCR prevails over the intraparticle field for the case of low porosity material. The fast carrier separation takes place within one nanoparticle.

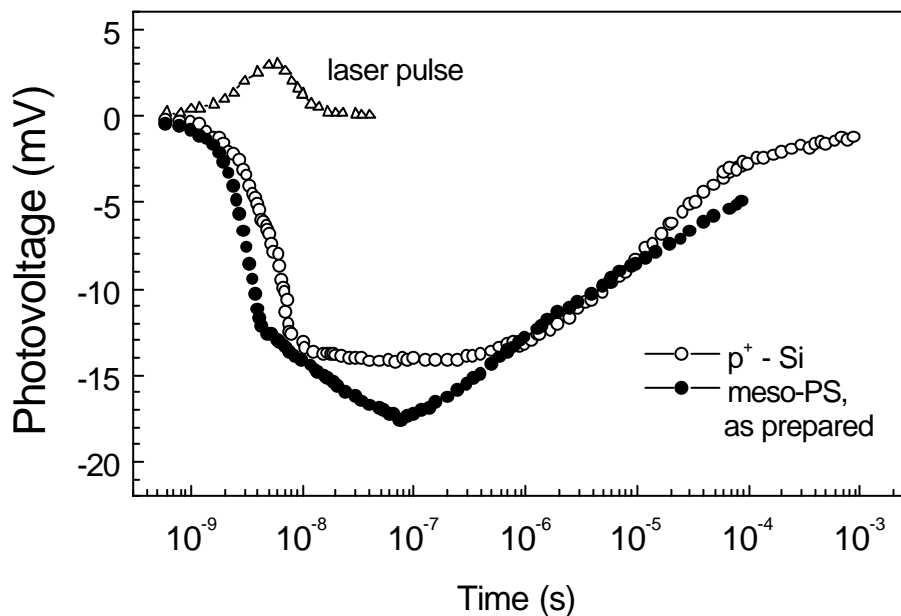


FIG. 3.2: Photovoltage transients for HF-etched p^+ -Si ($0.01 \Omega\text{cm}$) and as prepared free-standing meso-PS (substrate: p^+ -Si, $0.01 \Omega\text{cm}$, (100) orientation, anodization at 50 mA/cm^2 in 25% ethanoic HF for 20 min). The shape of the N_2 laser pulse is shown for comparison.

However, a retarded to 100 ns component arises in the PV transient of the porous Si sample in comparison to the p^+ -Si sample. If we take into account a much smaller concentration of free carriers in porous Si (this question will be discussed below), the width of the surface SCR of porous Si is much larger than of the p^+ -Si and the surface SCR consists of a large amount of nanoparticles. The retarded component of the PV arises due to the interparticle transport which is much slower than the intra-particle transport. In order to estimate the interparticle mobility one has to know the distance of excess charge separation. Its estimation from the PV value is not trivial because the part of the excess electrons and holes compensate the charge of each other and the amount of the non-compensated charge is not known.

The exponential decay of the PV transient for p^+ -Si is related to the lifetime of minority carriers (electrons in this case). The lifetime of minority carriers is spread over a wide time range due to trapping/detrapping effects on the internal surface states for porous Si.

3.2 Surface potential and free carrier concentration in mesoporous Si

The internal surface states on the surface of pores are extended throughout the bulk of the porous material. Charge carrier trapping diminishes the role of external surface states on the geometrical surface by decreasing the potential difference between the geometrical surface and the bulk. The relative input of both types of states is determined by the amount of the trapped charge and therefore depends on the density and distribution of surface states.

Figure 3.3 shows the intensity dependence of the PV amplitude for a set of free-standing meso-PS samples (substrate: p^+ -Si, 0.01 Ωcm , (100) orientation, anodization in 25% ethanoic HF at 50 mA/cm^2 for 20 min, 75 mA/cm^2 for 15 min, 100 mA/cm^2 for 10 min, or at 200 mA/cm^2 for 5 min) made at different anodization currents and of a HF-etched p^+ -Si substrate from which the porous Si was made. The initial band bending was very similar for the p^+ -Si sample and the p^+ -Si substrates used for the preparation of porous Si samples. The increase of the anodization current from 50 mA/cm^2 to 200 mA/cm^2 results in the increase of the porosity from⁶⁴ 50% to 70% and the density of internal surface states due to the larger surface to volume ratio in meso-PS.

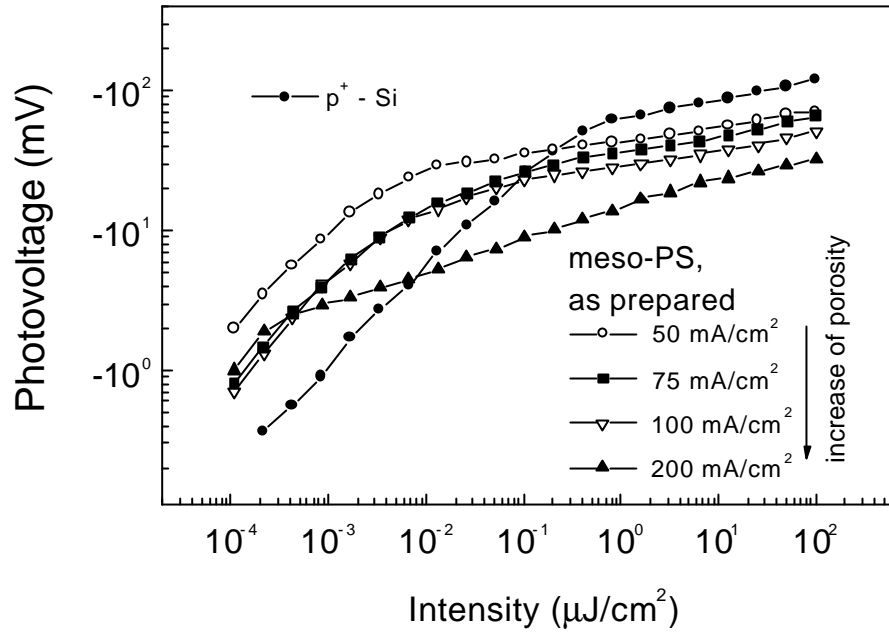


FIG. 3.3: Intensity dependence of the photovoltage amplitude for p^+ - Si ($0.01 \Omega\text{cm}$) and a set of as prepared free-standing meso-PS samples (substrate: p^+ -Si, $0.01 \Omega\text{cm}$, (100) orientation, anodization in 25% ethanoic HF at 50 mA/cm^2 for 20 min, 75 mA/cm^2 for 15 min, 100 mA/cm^2 for 10 min, or at 200 mA/cm^2 for 5 min) made at different anodization currents. Excitation with an N_2 laser.

The PV has negative sign for all samples, what is a characteristic feature for p-type semiconductors with downward band bending.⁹ The shape of the curves for meso-PS (except of 200 mA/cm^2) is similar to the shape for the p^+ -Si sample. For crystalline semiconductors, the PV is a linear function of the excitation intensity at small values (low signal case) and saturates at larger intensities (high signal case) under homogeneous excess charge carriers generation in the surface SCR. A non-homogeneous excess charge carriers generation may be the reason for the sub-linear dependence of the PV amplitude at small excitation levels in meso-PS. A saturation value of the PV (U_{pv}^{sat}) would be equal to the surface potential $\mathbf{j}_s = U_{pv}^{sat}$. A continuous shift of the PV amplitude at larger intensities toward smaller values is observed with increasing porosity and density of internal surface states. The existence of a depletion region in the vicinity of M/porous Si or porous Si/c-Si interfaces has been shown by several methods,^{65,66} while the band bending due to external surface states is usually neglected for materials with quantum dots.⁶⁷ The slight increase of the PV amplitude at larger intensities may be caused by the change of the occupation of external surface states (the influence of surface states population on the intensity

dependence of the PV in crystalline semiconductors was discussed by Shapira⁶⁸). The trapping effects are already dominating for meso-PS made at an anodization current of 200 mA/cm².

An essentially smaller concentration of free charge carriers in porous Si in comparison to the p⁺-Si substrate was numerously assumed with respect to the conductivity measurements.⁶⁰ For PV measurements, the free carrier concentration can be estimated from the shift of the intensity at which the transition from the low to the high signal case takes place (if the quantum efficiency of electron-hole pairs generation is independent of intensity). For example, this shift is about 60 times between the p⁺-Si substrate and meso-PS made at 50 mA/cm². With respect to the free carrier concentration of the p⁺-Si substrate ($p = 10^{19}$ cm⁻³), the free charge carrier concentration of the meso-PS made at 50 mA/cm² is $1.6 \cdot 10^{17}$ cm⁻³. This is in good agreement with the value obtained recently by FTIR measurements ($(0.6 - 1) \cdot 10^{17}$ cm⁻³).⁶¹

The spectral dependence of $-\ln(T)/d$, where T is the transmittance and d is the sample thickness is shown in Fig.3.4 for the p⁺-Si substrate and the as prepared free-standing meso-PS (substrate: p⁺-Si (100) orientation,

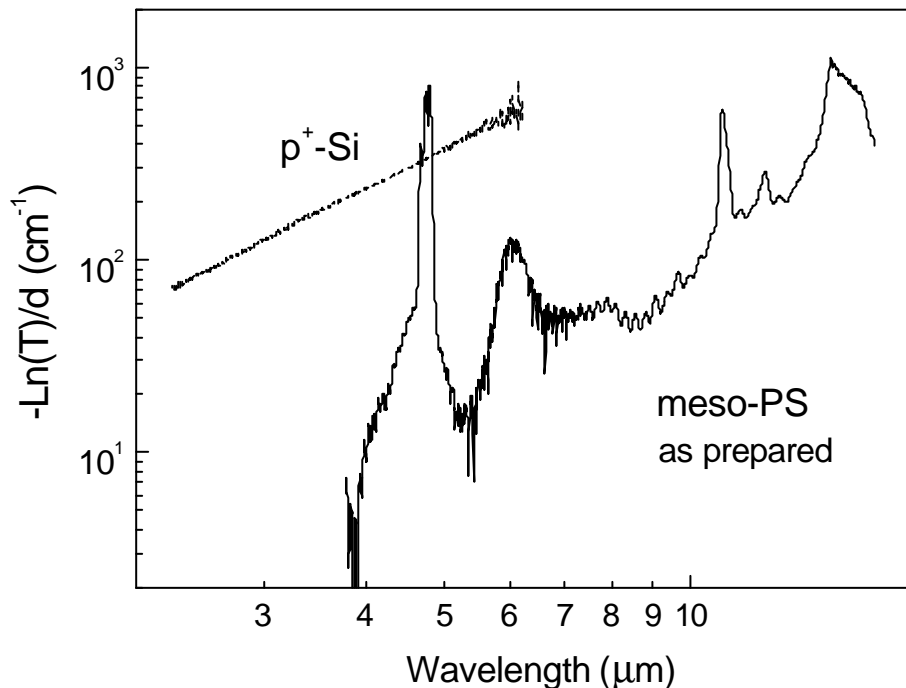


FIG 3.4: IR absorption spectra of p⁺-Si (0.015 Ωcm) and as prepared free-standing meso-PS (substrate: p⁺-Si, 0.01 Ωcm, (100) orientation, anodization at 50 mA/cm² in 25% ethanoic HF for 20 min). The curve for p⁺-Si is taken from Ref.⁶¹.

0.01 Ωcm , anodization at 50 mA/cm² in 25% ethanoic HF for 20 min). The curve for p⁺-Si sample (0.015 Ωcm) is taken from Ref.61. The quantity of $-Ln(T)/d$ is directly related to the absorption coefficient (without correction to interference what is not important for the analysis of the data). The spectral dependence of the reflection and scattering (which are nearly constant in middle IR range) were not taken into account. The continuous increase of the absorption background toward the higher frequency belongs to the absorption by free carriers. We estimate the free carrier concentration in as prepared free-standing meso-PS by the procedure described in Ref.61. Assuming porous Si as an effective medium and following the Drude model⁶⁹ the absorption coefficient is given by

$$a \sim p (1-r) l^2 t / n \quad (3.1)$$

where p , r , n , and l are the free charge carrier concentration, porosity, refractive index, and the wavelength of IR radiation, respectively. The value of n is 3.4 for crystalline Si, and about 2.1 for porous Si with 50% porosity.⁶¹ Free charge carrier concentration in p⁺-Si is $5 \cdot 10^{18} \text{ cm}^{-3}$. According to the ratio $-Ln(T)/d$ for crystalline Si and meso-PS the free charge carrier concentration is $1.55 \cdot 10^{17} \text{ cm}^{-3}$ for as prepared meso-PS. This value is in good agreement with the value estimated from the shift of the intensity dependence of the PV (discussion to Fig.3.3). Therefore, the free charge carrier concentration in meso-PS can be obtained from the intensity dependence of the PV.

3.3 Oxidation and surface states

Native oxidation of as prepared meso-PS leads to a continuous change of the electronic properties and therefore of the PV measurements with increasing storage time of as prepared samples. The velocity of the changes depends on the humidity and temperature of the ambience, but the quality and resulting PV transients look quite similar after long times of storage. In order to carry out experiment under well stabilized conditions we performed thermal oxidation of porous Si samples and investigate the role of surface states introduced by the oxidation for the PV.

Figure 3.5 shows the evolution of PV transients for as prepared free-standing meso-PS (substrate: p⁺-Si, (100) orientation, 0.01 Ωcm ,

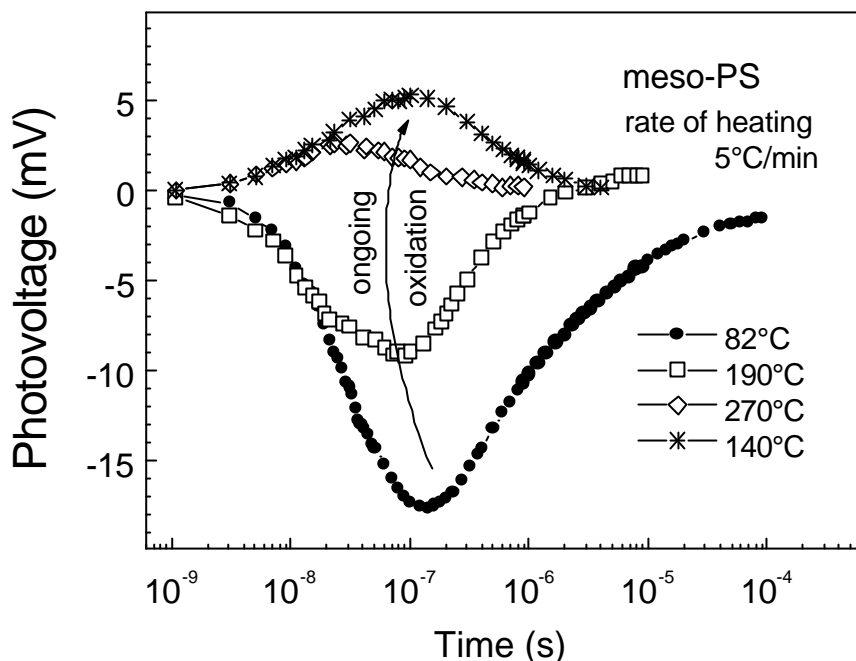


FIG. 3.5: Typical photovoltage transients of as prepared free-standing meso-PS (substrate: p^+ -Si, $0.01 \Omega\text{cm}$, (100) orientation, anodization at 50 mA/cm^2 in 25% ethanoic HF for 20 min) during annealing in air.

anodization at 50 mA/cm^2 in 25% ethanoic HF for 20 min) during annealing and subsequent cooling in air. The rate of heating was $5 \text{ }^\circ\text{C/min}$.

The PV signal is negative at low temperatures and short times of annealing and positive at large temperatures and long times of annealing. The negative PV signal does not return back when the temperature decreases again, which points to the chemical origin of the observed changes. Similar changes of the PV transients were observed for prolonged native oxidation at room temperature. We remark, that the value of the PV signals depend also on the rate of heating. Continuous transformation from negative to positive PV signal points out to the transition from downward to upward band bending, that means preferential storage of negative charge on the external surface states of oxidized porous Si.

The changes of chemical bonds due to oxidation can be investigated by FTIR technique. Typical IR transmittance spectra of as prepared (substrate: p^+ -Si, $0.01 \Omega\text{cm}$, (100) orientation, anodization at 50 mA/cm^2 in 25% ethanoic HF for 20 min), thermally oxidized in air (at $400 \text{ }^\circ\text{C}$ for 20 min) and HF-etched after oxidation free-standing meso-PS are shown

in Fig. 3.6. The Si-H_x stretching modes⁷⁰ (2087-2110 cm⁻¹), SiH₂ bending mode⁷¹ (910 cm⁻¹), and Si-H_x wagging modes⁷² (625, 666 cm⁻¹) are dominating in the spectra of as prepared meso-PS.

In order to stabilise the properties of the surface and to avoid any influence of oxidation process during PV measurements we performed oxidation of the meso-PS sample in air at 400 °C for 20 min. Upon annealing in air, new chemical bonds appear on the surface as a wide absorption band due to different Si-H and Si-O chemical bond configurations in the IR spectra. The lines of O₂-Si bending mode⁷³ (800 cm⁻¹), O₃-Si-H bending mode⁷⁴ (880 cm⁻¹), O₂-Si=H₂ bending mode⁷⁵ at 975 cm⁻¹, Si-O-Si stretching modes⁷⁶ (1070 – 1190 cm⁻¹) can be distinguished for oxidized sample. The well resolved peaks at 2200 cm⁻¹ and 2250 cm⁻¹ are attributed to the O₂Si-Si-H or O₂Si=H₂ and O₃-Si-H stretching modes,⁷⁷ respectively, and show the presence of O in the backbonds of Si. The surface is completely oxidized since no SiH_x stretching modes without oxygen in Si backbonds are observed after oxidation.

After oxidation, the oxide was removed by HF-treatment. The IR spectrum for HF - etched sample does not contain features of oxygen bonds and repeats all the lines of the as prepared sample. As remark, the

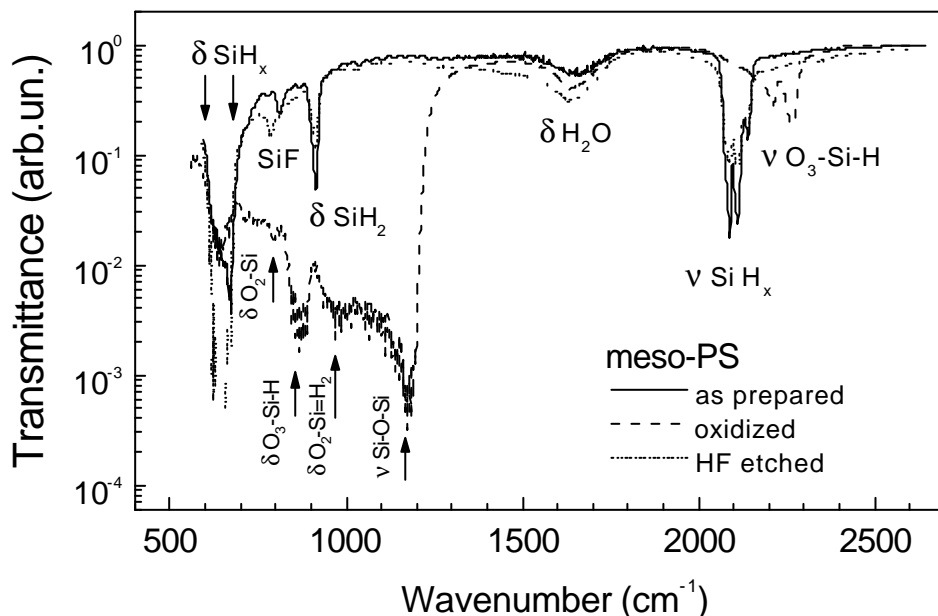


FIG 3.6: InfraRed transmittance spectra of as prepared (substrate: p⁺-Si, 0.01 Ωcm, (100) orientation, anodization at 50 mA/cm² in 25% ethanoic HF for 20 min), oxidized (in air at 400 °C for 20 min) and HF-treated (after oxidation) free-standing meso-PS.

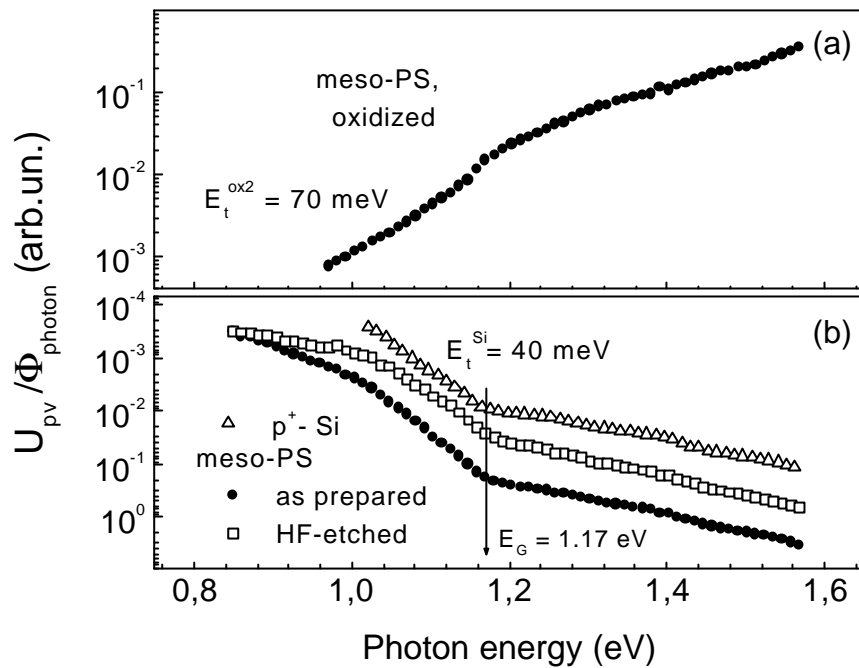


FIG 3.7: Photovoltage spectra for p^+ -Si ($0.01 \Omega\text{cm}$), as prepared (substrate: p^+ -Si, $0.01 \Omega\text{cm}$, (100) orientation, anodization at 50 mA/cm^2 in 25% ethanoic HF for 20 min), thermally oxidized (in air at $400 \text{ }^\circ\text{C}$ for 20 min), and HF-etched (after annealing) free-standing meso-PS.

lines around 800 cm^{-1} belong to Si-F.⁷⁸ The bending mode $\delta_{\text{H}_2\text{O}}$ of liquid water around 1650 cm^{-1} is well pronounced in all IR spectra.

As shown above, the mechanism of the formation of PV in meso-PS is determined by the separation of excess carriers in the built-in electric field of the surface SCR. This fact allows to investigate the band structure by spectral dependent PV measurements. We point out that up to now only a very few data about optical absorption below the band gap, are available for porous Si in general. The reason for this is that methods like constant photocurrent measurements (CPM)⁷⁹ which have been developed for the investigation of disordered semiconductors, can not be simply applied to a porous semiconductor (problem with contacts and large thickness variation of the free-standing porous Si). The advantage of PV measurements are the contactless approach and the very high sensitivity (changes of nano-Volts can be easily detected by using the lock-in technique).

Figure 3.7 shows photovoltage spectra of p^+ -Si ($0.01 \Omega\text{cm}$), as prepared (substrate: p^+ -Si, $0.01 \Omega\text{cm}$, (100) orientation, anodization at 50 mA/cm^2 in 25% ethanoic HF for 20 min), thermally oxidized (in air at

400 °C for 20 min), and HF-etched (after annealing) free-standing meso-PS. The PV spectra were normalised to the photon flux. The PV signal for p⁺-Si is negative in the whole spectral range. The PV spectrum contains a kink at 1.17 eV (band gap E_G). This value of E_G is close to 1.2 eV, which was measured by optical transmittance measurements.⁸⁰

The shape of the PV spectra for the as prepared meso-PS is similar to that of the crystalline material. The larger amplitude is in agreement with the intensity dependence of the transient PV at small excitation level. The slope of the tails below the band gap of as prepared meso-PS (E_t^{as prep1}) and crystalline Si (E_t^{Si}) is equal to 40 meV. An additional tail (E_t^{as prep2} = 87 meV) appears for the as prepared meso-PS below 1.04 eV. The fact that the tail with 40 meV appears in the p⁺-Si substrate and in the as prepared meso-PS samples gives evidence for an undisturbed by the huge internal surface of the meso-PS central part of the nanoparticles. The internal surface area of meso-PS is of the order up to 200 m²/cm³.⁸¹ The density of surface atoms is of the order of 5 · 10¹⁴ cm⁻². Therefore, more than 1% of all Si atoms in meso-PS are located at the internal surface. The surface atoms induce disorder and the tail with 87 meV can be related to the disordered surface region of the Si nanoparticles. The tail with 87 meV appears at the absorption which is less than the absorption at E_G by two orders of magnitude. This points to a very low disorder induced by the internal surface.

The PV spectrum for oxidized meso-PS has positive sign, which is in agreement with the change of the sign of the PV transient. Two tails are present in the PV spectra of oxidized meso-PS (E_t^{ox1} = 40 meV, E_t^{ox2} = 73 meV). The tail with E_t^{ox1} = 73 meV appears at the absorption which is less than the absorption at E_G by only two times. This means, in comparison to as prepared sample, that the degree of disorder has been increased dramatically due to oxidation. This is not surprising since oxygen is introduced with Si-backbonds during the oxidation process what induces strong stress.

Similar to the as prepared sample, two tails are present in the PV spectra of HF-etched meso-PS (E_t^{HF1} = 40 meV, E_t^{HF2} = 185 meV). The tail with E_t^{HF2} = 185 meV appears at the absorption which is less than the absorption at E_G by 30 times. This means that the removal of the oxide by the HF treatment reduces the stress in the Si-bonds in comparison to the oxidized meso-PS sample. On the other side, the ratio between surface and bulk atoms in the nanoparticles has been increased by the

oxidation and etching procedures so that the disorder in the HF-treated meso-PS sample is larger than the as prepared one.

3.4 Role of the characteristic dimensions of the nanoparticles

The mean size of the Si nanoparticles in meso-PS is continuously decreased by subsequent oxidation and treatment. Figure 3.8 shows the PV transients for as prepared (substrate: p^+ -Si, $0.01 \text{ } \Omega\text{cm}$, (100) orientation, anodization at 50 mA/cm^2 in 25% ethanoic HF for 20 min), oxidized (annealed in air at $400 \text{ } ^\circ\text{C}$ for 20 min), and HF-etched (after oxidation) meso-PS. The annealing and HF-etching processes were made in turn, the numbers in the figure present the sequence in the cycle (1- as prepared, 2,4,6 - oxidized, 3,5 - HF-etched). The as prepared meso-PS is hydrogenated as shown by our IR transmittance measurements and other publications.⁶³ Hydrogen provides the surface with good electronic passivation properties.⁸² The surface of oxidized meso-PS is covered by oxygen which introduces acceptor - like surface

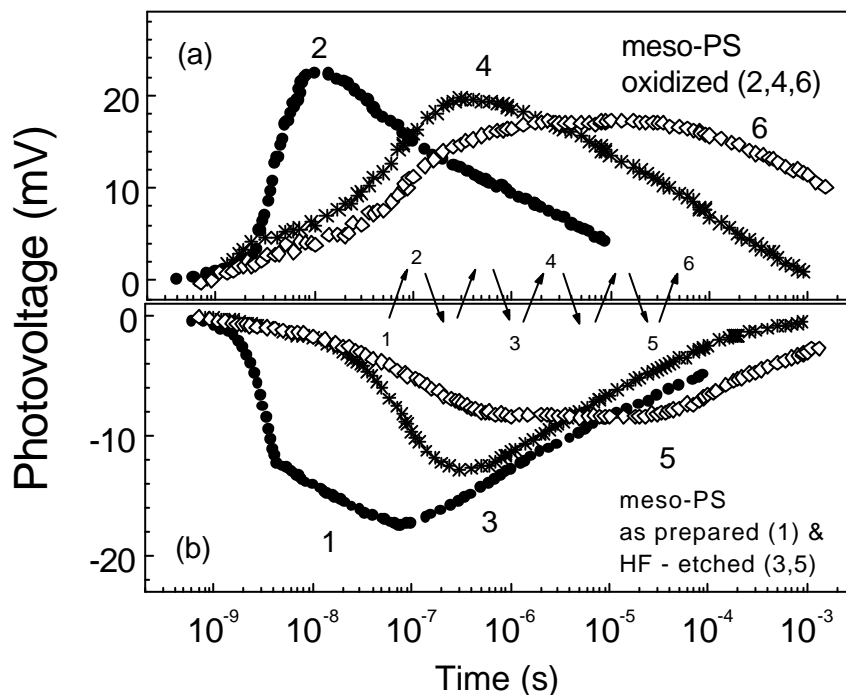


FIG 3.8: Photovoltage transients for (b) as prepared (substrate: p^+ -Si, $0.01 \text{ } \Omega\text{cm}$, (100) orientation, anodization at 50 mA/cm^2 in 25% ethanoic HF, 20 min), (a) oxidized (annealing in air at $400 \text{ } ^\circ\text{C}$ for 20 min), and (b) HF-treated (after oxidation) meso-PS. The annealing and HF-etching processes were made in turn, numbers in figure present the sequence in the cycle (see inset).

states⁸³ and create dangling bonds of amphoteric nature.⁶¹ Preferential trapping of electrons on the external surface states of meso-PS changes the downward to the upward band bending. This is the reason for the positive sign of the PV signal in oxidized porous Si (curve 2). The time of the PV formation in oxidized meso-PS is comparable with the duration of the laser pulse and gives evidence for charge carrier separation in the electric field of surface SCR. The acceptor-like states in oxidized meso-PS are removed by HF treatment and the sign of the PV changes to negative (curve 3) as for the as prepared sample. A similar change of the PV sign was also observed by the Kelvin-probe technique and explained as a change of porous Si to an n-type due to donor (water or oxygen)-like doping.⁸⁴

The growth velocity of a second SiO₂ bilayer is much lower than that of the first one for a Si surface.⁸⁵ The lateral growth covers the surface of porous Si by a thin oxide layer during oxidation, which is removed than by HF-etching. The initial skeleton with 6 - 10 nm average size⁶¹ of nanowires becomes essentially thinner and more disordered after 4 cycles. The kinetics of charge carrier separation changes dramatically in the oxidation - etching cycle (curves 3 - 6). The increase of the PV and separation of charge carriers become more and more retarded.

There are two reasons for the retardation: the mobility of charge carriers decreases and the electric field of the surface SCR decreases. The increase of surface-to-volume ratio with decreasing size of nanoparticles increases the role of interparticle transport for excess carrier separation. Further, the dimensions of the Si nanoparticles reach values at which quantum confinement takes place. The diameters of the nanoparticle are not constant. Therefore, barriers are introduced into the SCR and interparticle transport slows down the process of carrier separation. Charge carrier trapping on the internal surface states decreases the potential difference between geometrical surface and bulk of porous material and increases the width of surface SCR, therefore the electric field decreases. Smearing over the wide time range of the PV transients points out on the dispersive transport due to size disorder and disorder which was found by TOF measurements.⁷

The symmetric shape of the PV transients for HF-etched (negative PV signal) and oxidized (positive PV signal) meso-PS (compare curves 3 and 4 or curves 5 and 6) shows the similarity of the kinetics of charge carrier separation and, therefore, transport in these two cases. This shows that transport depends mostly on the size of nanopartiles and on

the topology of the porous matrix. The oxide coverage of the nanoparticles changes the type of band bending due to electron trapping on the external surface states and does not influence significantly the transport properties. Therefore, the very different charge carrier concentrations in HF-treated and oxidized meso-PS do not influence the mobility of excess charge carriers, different conductivities for as prepared and oxidized meso-PS originate⁶⁰ more from the change of charge carrier concentration.

The average size of the nanoparticles in porous Si can be decreased by decreasing doping level of the substrate (for example, from p^+ to p -Si).⁷ The PV transient of as prepared nano-PS (substrate: p -Si, 1 Ωcm , (100) orientation, anodization at 50 mA/cm^2 in 25% ethanoic HF for 20 min) (Fig.3.9a) is positive and strongly retarded in time up to the ms range (already limitation by RC). The size of nanoparticles is about 2-3 nm and free carrier concentration is extremely low in this case.⁶² The retarded shape of the PV is typical for diffusion PV (discussed in Chapter 1) which originates from the gradients of excess charge carrier and assumes the minor role of band bending. The positive sign of the PV

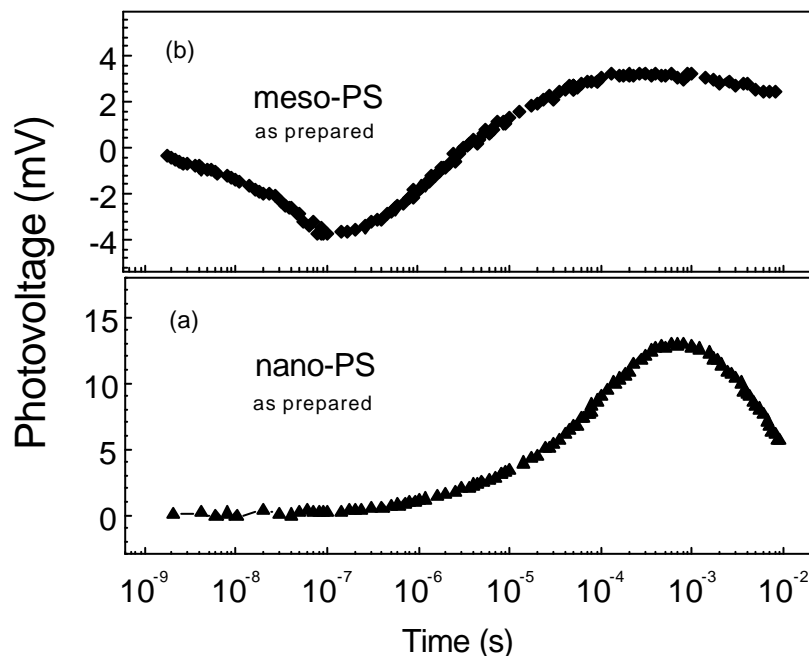


FIG. 3.9: Photovoltage transients for (b) as prepared free-standing meso-PS (substrate: p -Si, 0.15 Ωcm , (100) orientation, anodization at 50 mA/cm^2 in 25% ethanoic HF for 20 min) and (a) as prepared free-standing nano-PS (substrate: p -Si, 1 Ωcm , (100) orientation, anodization at 50 mA/cm^2 in 25% ethanoic HF for 20 min) made from different doping level of the substrates.

implements a higher diffusion coefficient for excess electrons than for excess holes.

The most striking feature of the PV transient of as prepared meso-PS (substrate: p-Si, 0.15 Ωcm , (100) orientation, anodization at 50 mA/cm² in 25% ethanoic HF for 20 min) (Fig.3.9b) is the change of the sign (negative for times up to a μs , positive for longer times) during the transient which can be explained as a superposition of the PV caused by band bending and of the diffusion PV. The concept of flat bands in porous Si of large porosity explains the absence of photovoltaic effect in diodes based on porous Si, which was reported several times⁸⁶ and which was explained by graded bands, which forces the photoexcited electrons and holes to move in the same direction and prevent the charge separation.

The characteristic feature of the diffusion PV transient is the time at which the peak is reached. Several possible reasons for the PV maximum were assumed for semiconductor depending on the conductivity, thickness, lifetime of charge carriers. In the next part we discuss the mechanism which limits the increase of the diffusion PV in porous Si.

3.5 Role of Maxwell relaxation time for charge carrier separation

The time of the peak position (t_{peak}) of the PV transients is the most characteristic feature of the PV transient in the case of diffusion PV. However, the analysis of t_{peak} is limited by the time scale of the measurements. For the oxidized porous Si sample, t_{peak} could be shifted over 3 orders of magnitude depending on temperature. A very good reproducibility of the PV transients was reached for measurements after oxidation in air at 400°C for 20 min. Figure 3.10 shows the PV transients of oxidized meso-PS (substrate: p-Si, 0.15 Ωcm , (100) orientation, anodization at 50 mA/cm² in 25% ethanoic HF for 20 min) at different temperatures. After oxidation, the sign of the PV signal is positive over the whole time range. The PV response within the first 100 ns we relate to the SPV (the oxidation changed the nature of the surface states and therefore the band bending). This component depends only slightly on the temperature. The peak of the slow component is related to the diffusion PV and shifts with increasing temperature to shorter times. The shift of t_{peak} was reproducible with temperature, which shows the thermal origin of this shift and absence of further oxidation.

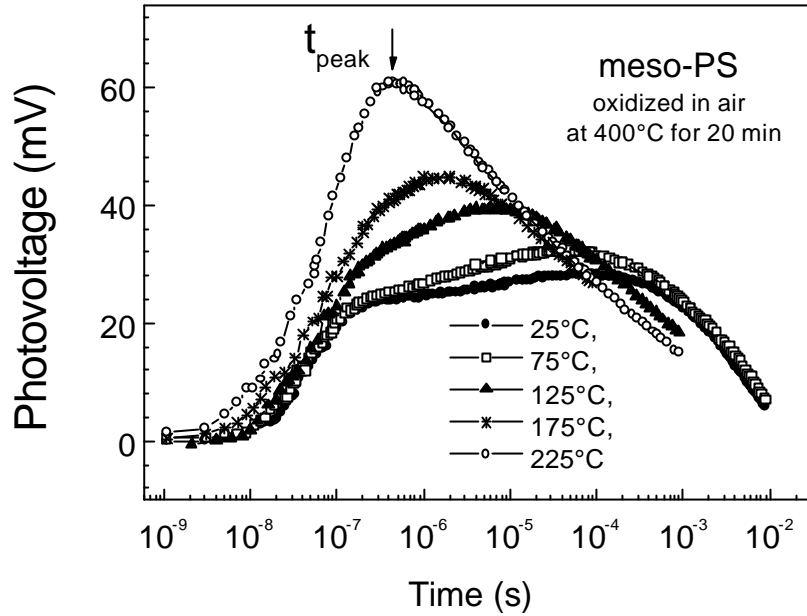


FIG. 3.10: Photovoltage transients for oxidized (in air at 400°C for 20 min) free-standing meso-PS (substrate: p-Si, 0.15 Ωcm , (100) orientation, anodization at 50 mA/cm² in 25% ethanoic HF for 20 min) at different temperatures.

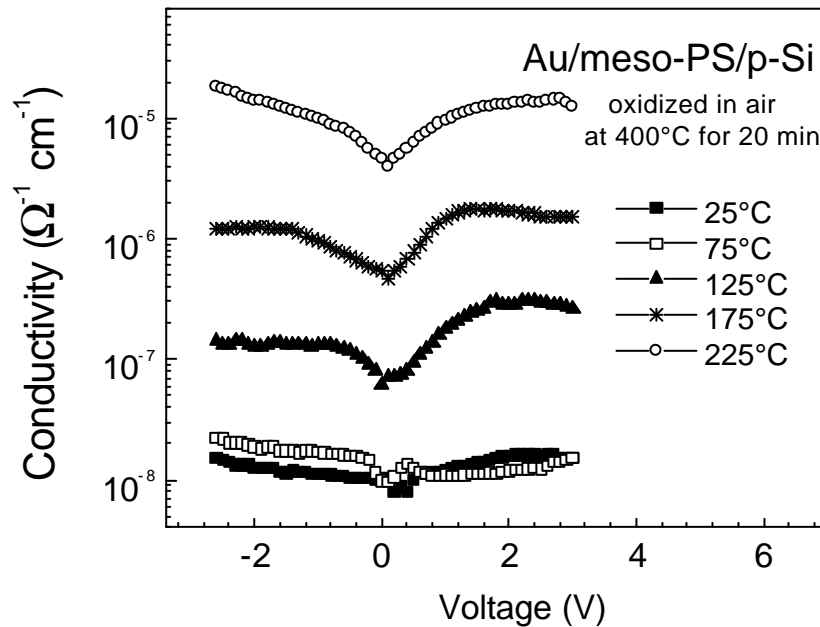


FIG. 3.11: Potential dependence of the dc conductivity for the Au/meso-PS/p-Si structure at different temperatures. Meso-PS was prepared and oxidized at identical to used in Fig.3.10 conditions, except of its lifting from the substrate.

In order to relate t_{peak} to the bulk electrical properties, dc conductivity measurements (with a HP 4140B picoammeter) were performed on Au/porous Si/p-Si structures at different temperatures under identical conditions as for the PV measurements (Fig.3.10). Fig. 3.11 shows the potential dependence of the dc conductivity (σ) for the Au/porous Si/p-Si structure at different temperatures. The conductivity increases with increasing temperature. The zero point of the $\sigma(V)$ characteristics is shifted at lower temperatures due to charging, probably of defects at the mesoporous Si/p-Si interface. To eliminate the contact problem the porous layer was made thick enough and its resistance limited the current, the unsymmetrical shape of the I-V characteristics with respect to the voltage polarity shows the introduced uncertainty into the determination of the conductivity value.⁸⁷

The dc conductivity is related to the dielectric (Maxwell) relaxation time τ_M via (1.3.13). The dielectric constant of porous Si is not exactly known. The excess charge carriers move within the silicon nanoparticles. It is reasonable to assume that ϵ ranges between 12 (crystalline Si) and 6 (with respect to the porosity, low frequency case).

Figure 3.12 compares the temperature dependence of t_{peak} and τ_M for oxidized meso-PS Si ($\epsilon = 12$ and 6, open circles and squares,

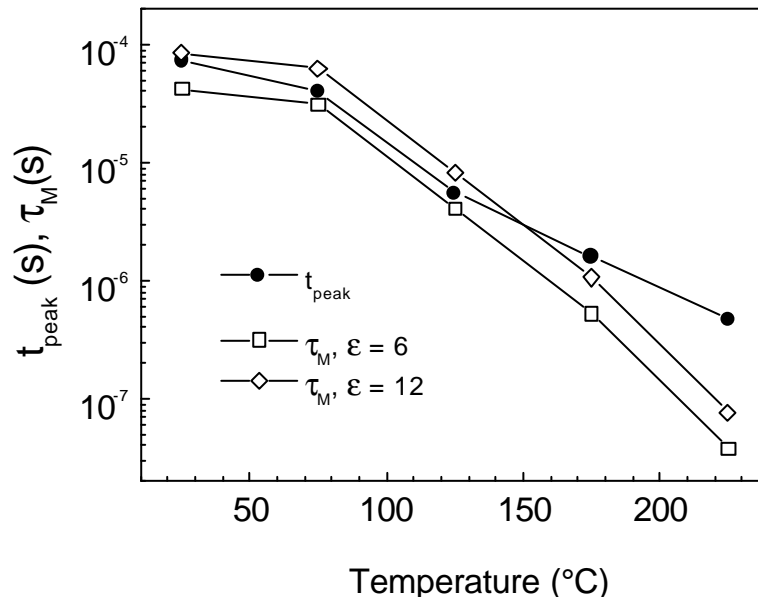


FIG. 3.12: Temperature dependence of time of the PV maximum (t_{peak}) of free-standing meso-PS and Maxwell relaxation time (τ_M) of Au/meso-PS/p-Si structure, respectively. Both samples were oxidized in air at 400°C for 20 min prior to the temperature measurements in order to stabilise their surface properties.

respectively, σ taken at -1 V). The values of t_{peak} fit excellently with τ_M at the lower temperatures.

This shows directly the importance of the dielectric relaxation for the formation of diffusion PV transients. At higher temperatures, t_{peak} becomes larger than τ_M while this deviation exceeds the uncertainty caused by the determination of σ . The reason of this deviation is that t_{peak} and τ_M are related to the electronic transport at different length scales. At shorter times, i.e. higher temperatures, the separation of excess carriers within shorter length scales becomes much more important while the dc conductivity is measured over the whole sample thickness.

The PV technique allows to measure contactless the dc conductivity of a porous semiconductor. Short circuit, uncertainty in the contact area and sample thickness under contacts evaporation are avoided in this case.

3.6 Conclusion of chapter 3

Porous silicon of different porosity was used to demonstrate the transition from surface PV to diffusion PV in porous materials. Separation of light induced charge carrier takes place in the electric field of surface SCR in meso-PS with low porosity. The surface potential decreases with increasing porosity. The free charge carrier concentration is estimated of the order of $1.6 \cdot 10^{17} \text{ cm}^{-3}$ in meso-PS. The surface potential and charge carrier concentration change with time due to the oxidation process. The SiO_2 bonds introduce acceptor - like electronic states at the external surface of porous Si, which change the downward band bending to the upward. The decrease of the electric field of the surface SCR and the decrease of the size of nanowires with increasing porosity leads to the retardation of the charge carrier separation. The kinetics of the retardation are similar for H-terminated and oxidized porous Si surfaces and depend on the size of the nanoparticles and on the surface morphology. The potential difference between the surface region and the bulk can be neglected in nano-PS with large porosity. The PV appears mainly due to concentration gradients under strong light absorption and charge carrier separation takes place in a diffusion process. The diffusion PV transients are characterized by the maximum, the time at which coincides with the Maxwell relaxation time. The increase of the PV is determined by the diffusion of charge carriers and its shape in agreement with the shape of simulated transients of the diffusion PV model. The decay is determined by the recombination of

charge carriers. The PV measurements open new opportunities to the contactless electrical characterisation of porous semiconductors and its application.

CHAPTER 4 Diffusion photovoltage in poly(p-phenylene-vinylene)

The role of the Maxwell (dielectric) relaxation time for the diffusion PV was discussed in the previous chapter. An increase of the PV signal is possible only until the Maxwell relaxation time (τ_M) is not reached. For some materials, the value of τ_M which results from the conductivity and permittivity of the material may exceed the time necessary for excess charge carriers to diffuse over the thickness of the layer. Therefore, the spatial separation of excess electrons and holes in the diffusion process due to the concentration gradients will dominate above the attraction due to internal electric field between separated electron and hole clouds over the all time of the PV measurements.

An example of a material with a low conductivity is the organic polymer poly(p-phenylene-vinylene) (PPV). PPV is one of the basic materials for modern organic light-emitting diodes (OLEDs) due to a high efficiency of radiative recombination.⁸⁸ A better understanding of the basic involved processes, like charge carrier injection, charge carrier transport, electron-hole interaction (formation of excitons), and radiative recombination in organic molecular semiconductors, is necessary for the further improvement of OLEDs characteristics.

PPV consists of interconnected organic polymer chains without long range structural order. A relatively weak interaction exists between the

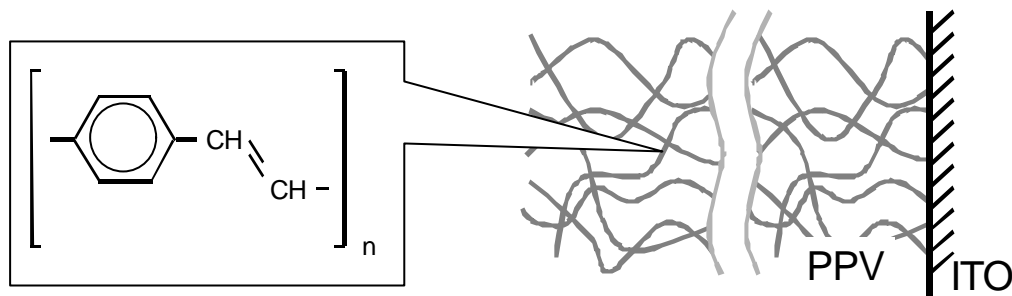


FIG.4.1 Basic element of polymer chain in PPV and schematic picture of topology of PPV layer at ITO substrate.

chains what makes the material flexible. A schematic picture of the polymer is shown in Figure 4.1. The chemical content of a basic PPV polymer unit is given in the inset. The electrical conductivity results from the mobile charge carriers introduced by a series of alternate single and double carbon bonds. If an organic molecule contains series of alternate single and double carbon bonds in a chain, the π -orbital is delocalized over the entire chain above and below the framework of the sigma bonds. This enables delocalized electrons in conjugated polymers to act as charge carriers along the chain. Due to the large intra-chain distance, the transport of charge is believed to be principally along the conjugated chain with inter-chain hopping or tunnelling.

Several concepts were applied to describe the transport properties of PPV. The hopping in disordered system,⁸⁹ multiple trapping transport with exponential^{90,91} or Gaussian³ distributions of traps, polaron transport^{3,92} and hopping of polarons⁹³ were reported. Domination of positive charge carriers, dispersion and low drift mobility for holes on the order of 10^{-6} .. 10^{-5} cm^2/Vs ,³ and much smaller⁹² for electrons, wide distribution of electronic states which change the concentration of mobile charge carriers or the effective mobility are general characteristic features of the electrical transport in PPV. Thermal activation of the conductivity or mobility may reveal information about the energy position or distribution of electronic states. An activation energy (E_A) strongly depends on the preparation conditions and exposure to oxygen in PPV. A number of different values of E_A (0.03-0.06 eV and 0.13-0.18 eV (Ref.94), 0.40-0.42 eV and 0.49-0.53 eV (Ref.95)). Experimental evidence for the existence of bipolaron states in PPV at 0.6 eV and 1.6

eV was obtained from photoinduced absorption spectra.⁹⁶ Therefore, further experimental studies of the carrier transport and the nature of traps is required to distinguish between different transport models.

A new approach to the investigations of the electronic transport in PPV by means of the diffusion PV method will be discussed in this chapter. Under the gradient of concentration of excess charge carriers due to light absorption, the spatial separation of excess electrons and holes with different diffusion coefficients will proceed in time. The kinetic of the PV signal contains information about the charge carrier separation until the Maxwell (dielectric) relaxation time (τ_M) is reached (the role of τ_M for the separation of charge carriers was discussed in Chapter 1 and experimentally shown in Chapter 3). The value of τ_M which results from the conductivity of $10^{-11}..10^{-12} \Omega^{-1}\text{cm}^{-1}$ (Ref.97) is of the order of 0.1-1 s in PPV, that is essentially longer than the possible time of the PV measurements (RC limitation, 11 ms).

The built-in electric field, for example due to the trapped charge on the surface states or at PPV/ITO interface, can accelerate the excess charge carriers and change the kinetic of the diffusion process. The role of the electric field can be suppressed or elevated by variation of the ratio between the layer thickness (L), the absorption length of the light (a)

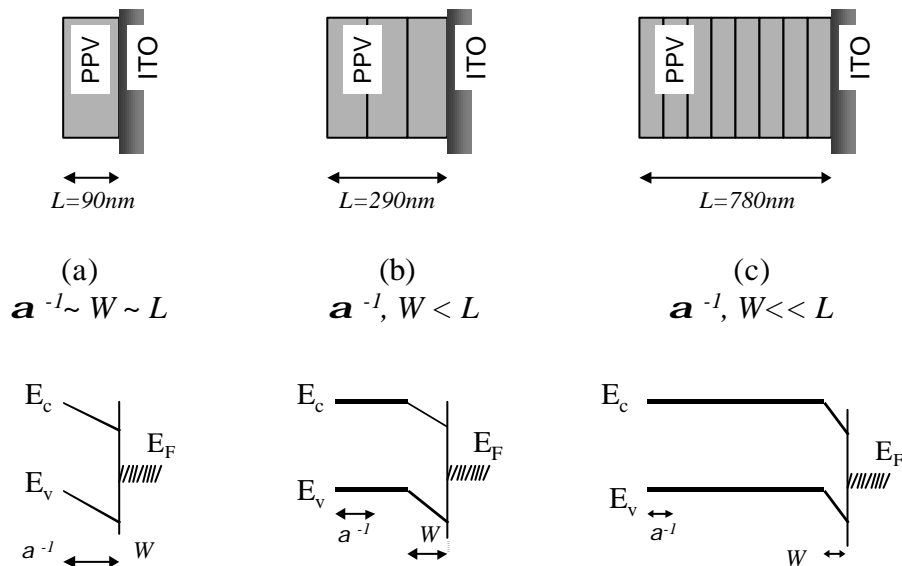


FIG.4.2: Geometry and band energy diagram of thin (a), middle (b) and thick (c) PPV layers on the ITO substrate, where a^{-l} , W , L are the absorption length of the light, width of the interface space charge region, and thickness of the PPV layer, respectively.

and the width of the surface space charge region (W). Three PPV samples with the thickness of 90 nm, 290 nm and 780 nm were used for the measurements and denoted as thin, middle and thick, respectively. Figure 4.2 shows the schematic geometrical picture and band energy diagram of the PPV films with different thickness. Due to technological reasons discussed in Chapter 2, the PPV films consist of layers of approximately 90 nm thickness each. The first layer at the ITO substrate is highly doped (10^{16} cm^{-3})⁹⁸ and contains a space charge region with band bending. The estimated value of W is 50 - 150 nm.⁹⁸ Light of wavelength $\lambda=337$ nm was used for the excitation of PV transients, the respective absorption length α^{-1} is about 10^{-5} cm in PPV. Therefore, the excess charge carriers were generated homogeneously in the thin sample, which is completely depleted due to the PPV/ITO interface. A strong gradient of the excess carrier concentration appeared in the thick sample, where the depletion region is essentially thinner than the layer thickness.

In this chapter we discuss the formation of the PV signal due to spatial separation of excess charge carriers in a diffusion process under light induced concentration gradients (diffusion PV). Simulations of the PV transients by means of the diffusion PV model developed in Chapter 1 will be made for the thick PPV films where the diffusion dominates and diffusion coefficients of excess holes (D_p) and electrons (D_n) can be estimated. The role of the intensity of the light pulse and of CW bias illumination on the charge carrier separation will be discussed. The influence of the PPV/ITO interface on the PV will be shown in thin PPV films. The thermal activation of the diffusion PV will be demonstrated and the activation energy of the PV amplitude and time of the PV maximum will be determined.

4.1 Gradient of concentration as a driving force of photovoltage in a thick film

The sign of the diffusion PV depends on the sign of the more mobile charge carriers and on the direction of the concentration gradient. The direction of the concentration gradient of excess charge carriers induced by light can be changed by changing the direction of illumination. Figure 4.3 shows typical PV transients of the thick PPV sample at a front (b) and back (a) side illumination. Both transients are strongly retarded in time in comparison to the duration of the laser pulse what is usual for

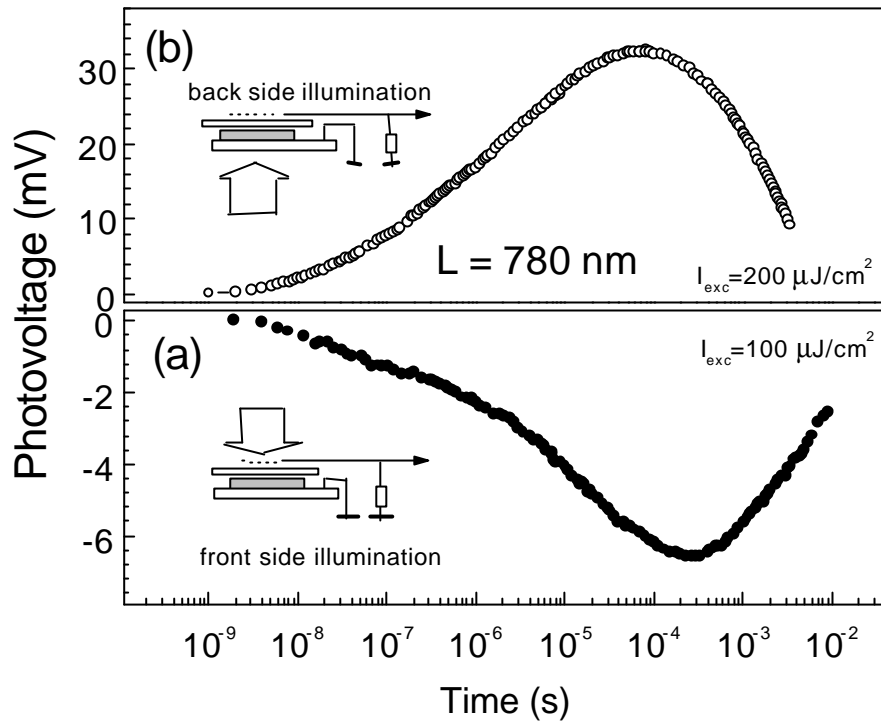


FIG.4.3: Photovoltage transients of the thick PPV sample (780 nm thickness) at a front (a) and back (b) side illumination. The insets show the scheme of illumination.

diffusion PV. The positive (negative) sign of PV under back (front) side illumination corresponds to the faster propagation of positive charge carriers in PPV with $D_p > D_n$. The different signs of the PV at the opposite illumination directions are caused by the opposite direction of the concentration gradients. The amplitude of the PV transient for a front side illumination is smaller while the time at which the amplitude is reached is longer. Variations of the absolute value of the amplitude and of the time position of the minimum (maximum) is caused by different illumination intensities (absorption by the Cr-electrode or glass substrate) and the influence of the PPV/ITO interface. The charge carrier separation at the PPV/ITO interface will be discussed in the next section.

4.2 Role of PPV/ITO interface in thin film

Figure 4.4 shows typical PV transients of the thin PPV sample at a front and back side illumination. These transients are also strongly retarded in time but the sign of the two processes is independent of the illumination direction. The role of the light induced gradient of the concentration is negligible for the formation of the PV in the thin film,

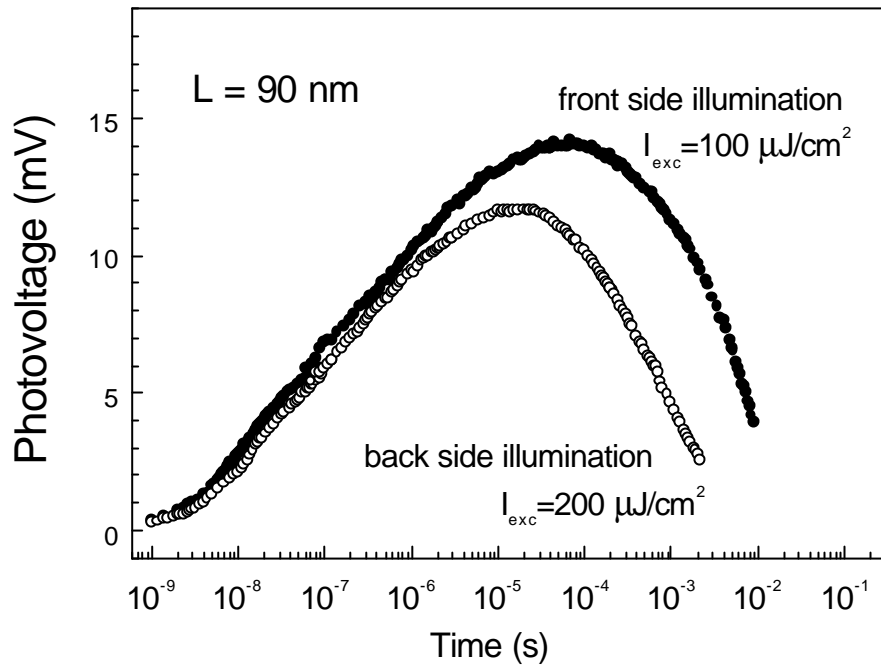


FIG.4.4: Photovoltage transients of the thin PPV sample (90 nm thickness) at a front and back side illumination.

since the values of the film thickness and the absorption length of the light are comparable.

The preferential location of holes near the free surface is concluded from the positive sign of the PV. The value of W is about 100 nm for thicker PPV layers on the ITO substrate as obtained from measurements by impedance spectroscopy.^{89,99} While the diffusion coefficient for holes is larger than for electrons and therefore, the injection of holes into the ITO is preferable, the downward band bending (from a free surface to interface) and potential barrier at the PPV/ITO interface should prevent the hole injection. Two reasons can be responsible for the PV formation in the thin PPV layer: (i) the downward band bending displaces the excess holes toward the free surface and excess electrons toward the interface and/or (ii) preferential injection of electrons into the ITO separates the excess electrons and holes.

Figure 4.5 shows PV transients at a front side illumination of the thin PPV sample at different temperatures. The PV signal is positive at lower temperatures and the sign does not change during the transient. With increasing temperature, a negative component arises in the PV transient at longer times.

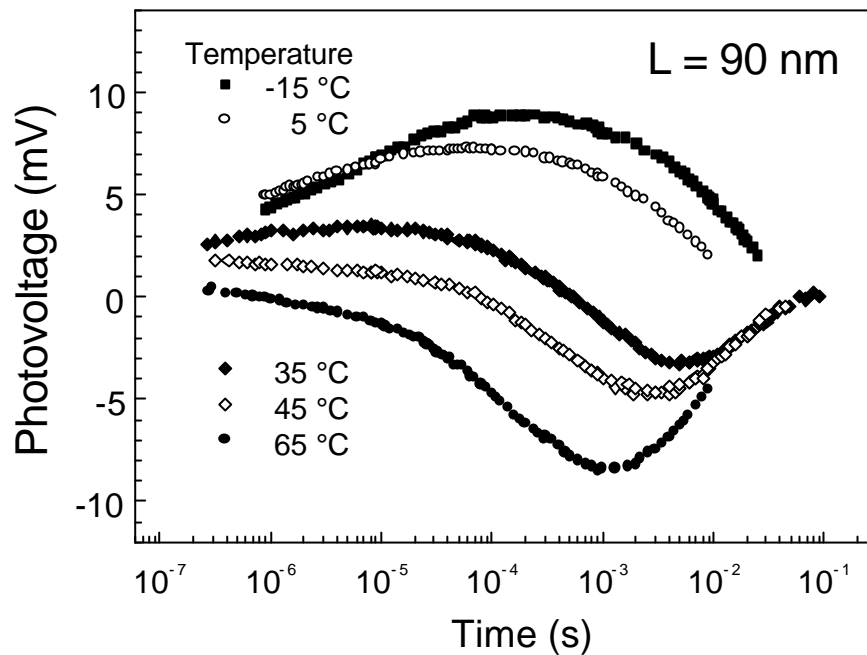


FIG.4.5: Photovoltage transients of the thin PPV sample (90 nm thickness) at a front side illumination at different temperatures.

The negative component of the PV (similar to that in the thick sample) dominates at the higher temperatures. The reason for the negative PV at higher temperatures is the injection of excess holes into the ITO substrate becoming possible due to thermal activation over the interface potential barrier. The positive and negative signals, for example at 35 °C, during the PV transient show the superposition of (i) the charge carrier separation by the built-in electrical field and/or the electron injection into ITO substrate at shorter times and (ii) the preferential recombination of holes at the ITO/PPV interface at longer times. As remark, the change of the type of band bending with time at higher temperatures due to the filling of interface states and due to the change of the interface dipole can not be excluded.

The unsymmetrical PV signal at a front and back side illuminations in the thick PPV film can be explained now. The gradient of the excess charge carrier concentration and the built-in electric field of the interface space charge region separate the charge carriers in one direction at a back side illumination (larger amplitude and shorter time of maximum) and in opposite directions at a front side illumination (smaller amplitude and longer time of maximum).

4.3 Dependence of the spectral PV on the layer thickness

Figure 4.6 shows the spectral dependencies of the PV signals for the co-phased (X) and shifted by 90° (Y) components with respect to the exciting light signals for the thin (a), middle (b), and thick (c) PPV samples (front side illumination). The appearance of the PV at around 2.3 eV for PPV layers of different thickness implements the existence of electronic states essentially below the band gap of PPV ($E_G = 2.4$ eV^{92, 100}). The X-component has a positive sign in the thin sample, changes the sign from positive to negative in the middle sample and a negative sign in the thick sample. The positive (negative) sign of the spectral PV signal at 3.7 eV in the thin (thick) sample is in agreement with the sign of the transient PV signal. The change of the sign of the PV signal for the middle sample near the band gap of PPV is caused by the change of the absorption length of the light and transition from homogeneous illumination to strong absorption case with respective change of the PV mechanism. The Y – component shows the degree of retardation of the PV signal with respect to the duration of the chopped light pulse (chopper frequency 70 Hz). The Y-component is much smaller than the X-component in the thin layer, the PV signal is fast. This ratio increases with increasing sample thickness, which is in agreement with the longer PV transients for the thicker samples. The PV transient of the middle PPV sample at a front side illumination (not shown) has the same sign and shape as of the thick one, but the value of t_{max} was two time smaller. The decrease of the spectral PV signals toward the UV range is due to the decrease of the photon flux.

The normalized PV spectrum for the thick sample with dominating diffusion PV is shown in Figure 4.7. The spectrum has a kink at around 2.45 eV, which corresponds to the band gap of PPV. The value of the band gap of 2.4-2.5 eV was found by other methods.^{92,100} The value of sub-band gap tail is 70 meV, which shows rather large disorder in this material.

4.4 Estimation of the diffusion coefficients

The dependence of t_{max} on the thickness of the samples does not allow to determine the diffusion coefficient of excess charge carriers since several mechanisms are involved in the formation of the PV in the thin and middle PPV layers. However, t_{max} decreases with decreasing

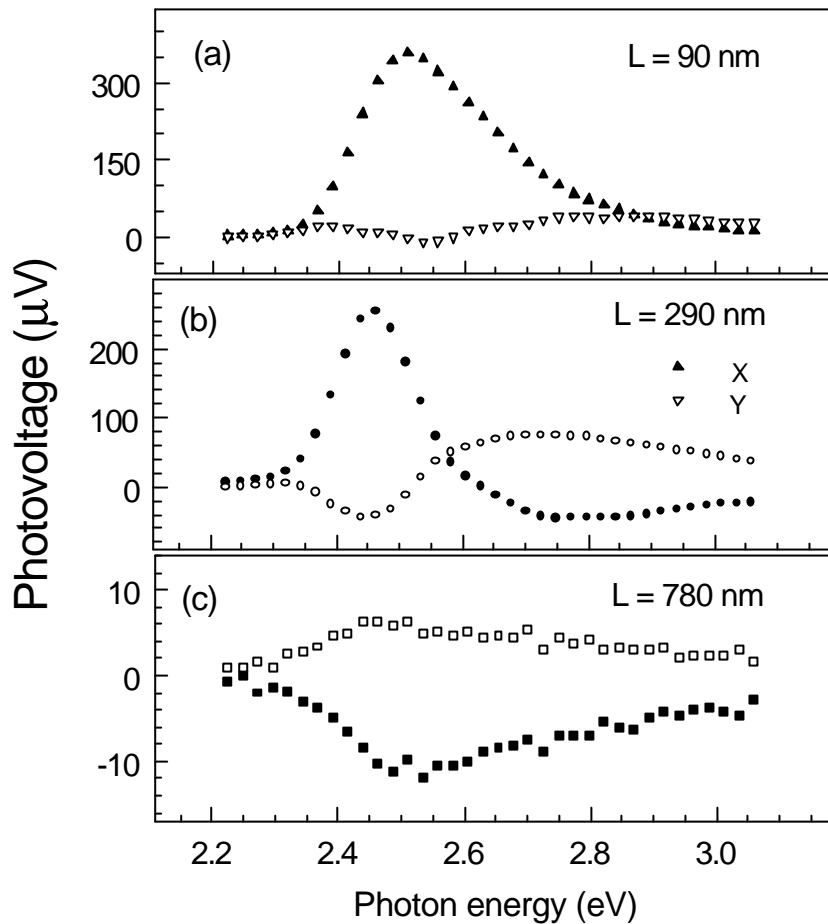


FIG.4.6: Co - phased (X) and shifted by 90° (Y) with respect to the exciting light components of photovoltage spectra of (a) the thin ($L=90 \text{ nm}$), (b) middle ($L=290 \text{ nm}$) and (c) thick ($L=780 \text{ nm}$) PPV samples.

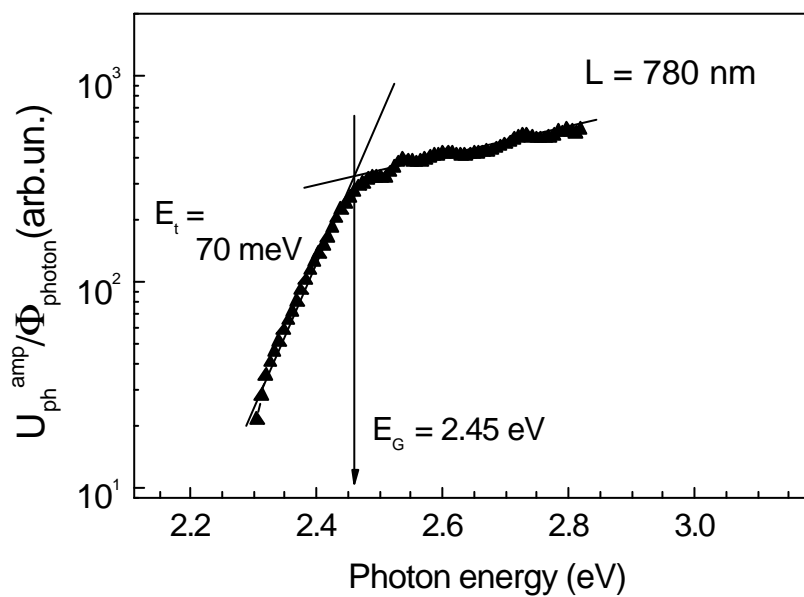


FIG.4.7: Photovoltage amplitude of the thick ($L=780 \text{ nm}$) PPV sample (normalized to the photon flux).

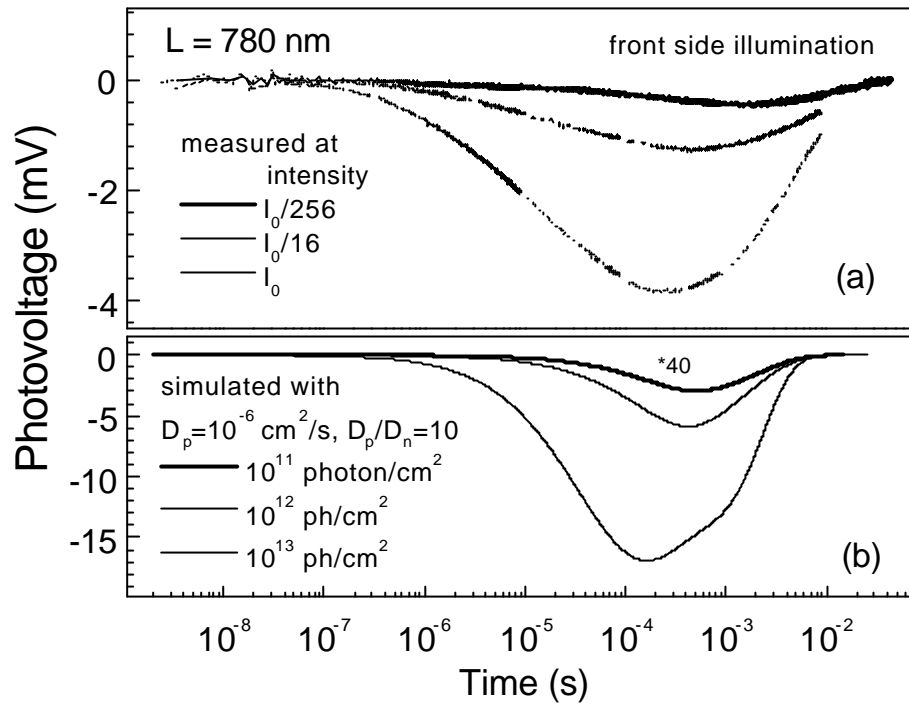


FIG.4.8: Measured (a) and calculated (b) photovoltage transients of the thick PPV sample for different illumination intensities.

thickness of the PPV layers. Due to this fact, the model of the diffusion PV (discussed in Chapter 1) which considers the diffusion over the thickness of the layer can be applied to the thick PPV sample with dominating diffusion PV in order to estimate the diffusion coefficients of holes (D_p) and electrons (D_n). The diffusion length of holes in PPV is of the order of 200 - 300 nm. This value increases for the diffusion PV due to suppressed recombination of spatially separated charge carriers and it will be comparable with the thickness of the layer, therefore the light induced excess holes are able to diffuse over the thickness of the layer.

Figure 4.8a shows PV transients for the thick PPV sample (front side illumination) at different excitation levels. The increase of the illumination intensity causes an increase of the PV amplitude and a decrease of t_{max} .

The model of diffusion PV for PPV takes into account diffusion of charge carriers with constant diffusion coefficients $D_{p,n}$ and drift of charge carriers due to Coulomb interaction between separated in space charge carriers of opposite sign. The thickness of the layer $L=780$ nm, the absorption coefficient of the light 10^5 cm^{-1} , dielectric constant of PPV as 4 (Ref.92) were taken as parameters for the simulations. As was shown in Chapter 1 for a sample of a given thickness and large Maxwell

relaxation time in comparison to the time of diffusion over the thickness of the sample, the value of t_{max} is determined by the diffusion of the charge carriers with the larger diffusion coefficient, i.e. D_p . The “width” of the PV transient depends on the D_p/D_n ratio.

The numerical simulation of PV transients at different excitation levels is given in Figure 4.8b. The increase of the light intensity was considered as an increase of the initial concentration of excess charge carriers. The simulated PV transients show the same tendency as the measured. The amplitude of the PV increases and the time at which the maximum of the PV is reached decreases with increasing light intensity. The calculated and measured PV amplitudes and values of t_{max} are in good agreement. This allows to estimate the values for D_p and D_n as about 10^{-6} cm²/s and 10^{-8} .. 10^{-7} cm²/s, respectively. The value of D_p is in good agreement with the hole mobility of 10^{-5} cm²/Vs obtained from the time-of-flight measurements.³

4.5 Dependence of the diffusion PV on bias illumination

Constant diffusion coefficients independent of the sample thickness and time were used to simulate the diffusion PV transients. However, the mobility (diffusion coefficient) of holes depends on the thickness of the layer and transport is dispersive in PPV due to a large amount of traps.³

The differences in measured and calculated PV transients can be clearly seen if representing the PV transient in a linear scale. Figure 4.9 compares measured and simulated PV transients without and with CW bias illumination ($\lambda=500$ nm, $I=10$ mW/cm²) in a linear time scale. The calculated PV transients are plotted in Figure 4.9b. The D_p and D_n of 10^{-6} cm²/s and 10^{-8} cm²/s, respectively, are used for the simulations. All other parameters are the same as used for the simulations shown in Fig.4.8. The bias illumination was introduced into the diffusion PV model as a constant level of an intrinsic concentration of electrons n_0 and holes p_0 . While the amplitude of the PV and the time at which the maximum of the PV is reached are similar for measured and simulated PV transients without bias illumination, the increase of the measured PV transient is faster than the increase of the simulated one. The reason for this is, that, due to the dispersive nature of the transport, the diffusion coefficients decrease in time. The values of the PV amplitude and of t_{max} decrease under bias illumination. The “width” of the PV transient is smaller under bias illumination, an increase of the diffusion coefficient of electrons

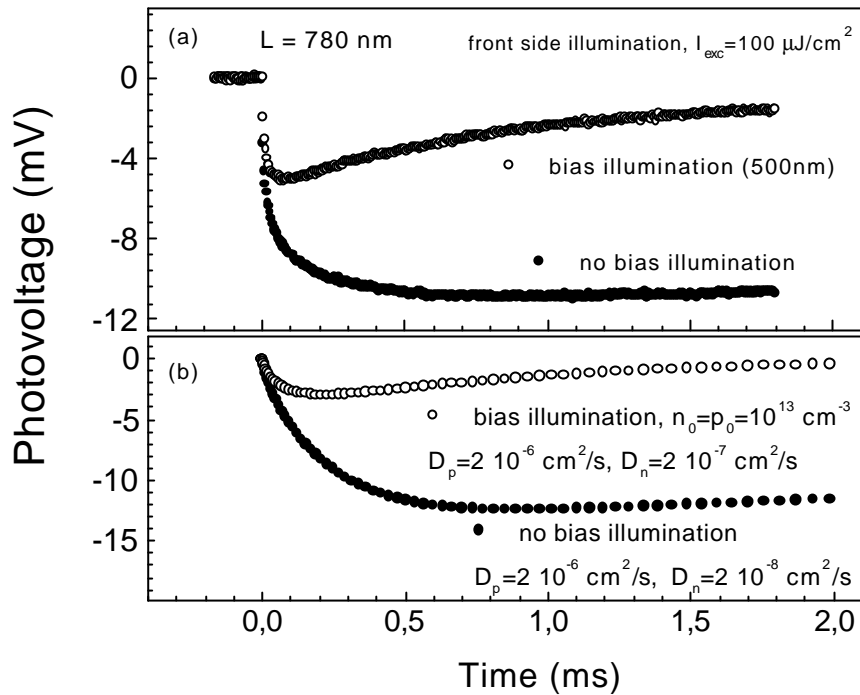


FIG.4.9: Measured (a) and calculated (b) photovoltage transients of the thick sample for laser excitation with and without bias illumination.

should be introduced into the model in order to simulate this effect. The filling of deep states by excess charge carriers, which rises the quasi Fermi-level and shifts the transport level toward higher energies with lower detrapping time is the possible physical reason for the higher diffusion coefficients.

4.6 Thermal activation of the diffusion photovoltage

Figure 4.10 shows PV transients at a front side illumination of the thick PPV sample at different temperatures. The PV amplitude increases with increasing temperature. The value of t_{\max} decreases with increasing temperatures up to 300 K and remains constant at higher temperatures within the range of the measurements. The retarded shape of the diffusion PV transients is unchanged within the range of the measurements.

It is well known that the surface PV decreases with increasing temperature, because of the thermal transitions of charge carriers which compete with the optically-induced transitions are raised.¹⁰¹ An increase of the amplitude with increasing temperature is expected for the diffusion PV and implies the thermal activation of the diffusion

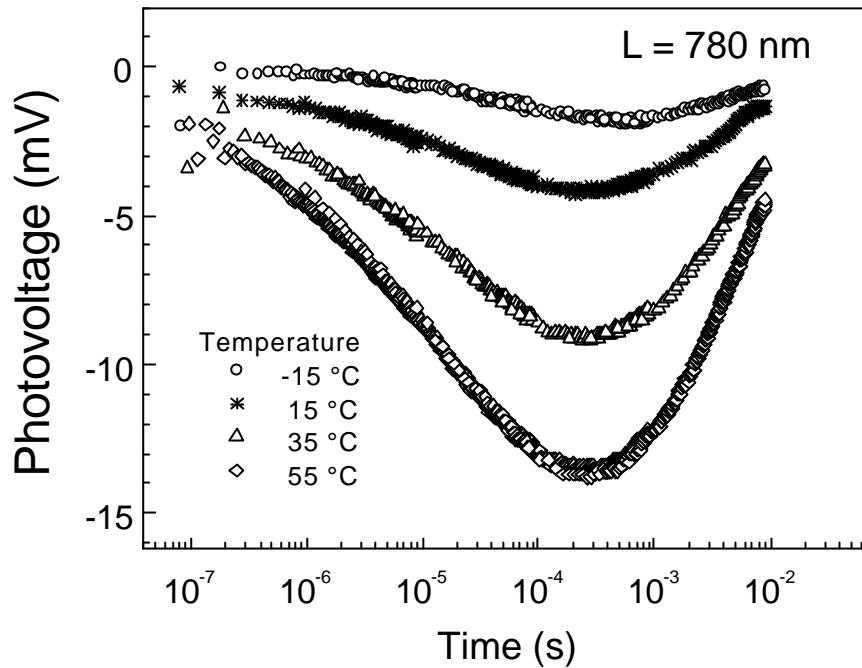


FIG.4.10: Photovoltage transients at a front side illumination of the thick PPV sample at different temperatures.

coefficients and/or of the charge carrier concentration. Figure 4.11 shows the Arrhenius plot of the PV amplitude U_{pv}^{ampl} (a) and the time at which the maximum of the PV is reached t_{max} (b) for thick and middle PPV samples. The activation energy E_A of the PV amplitude is 0.42 eV for the samples of thick and middle thickness. This value is in good agreement with the $E_A=0.40-0.42$ eV,¹⁰² which was identified from the deep level transient spectroscopy as the electron traps, and with 0.40-0.44 eV or 0.4 eV, which was measured by broadband impedance spectroscopy or *dc* conductivity measurements, respectively.¹⁰³ Thermal activation of t_{max} implies thermal activation of the diffusion coefficient of holes due to the diffusion PV model. The same activation energies of 0.42 eV for U_{pv}^{ampl} and t_{max} which are seen at low temperatures for the PPV sample of middle thickness show that the PV amplitude increases at the expense of the faster carrier separation at higher temperatures. The independence of t_{max} on temperature at higher temperatures shows, probably, an increased role of the carrier recombination at higher temperatures. A potential barrier which exists at the PPV/ITO interface also complicates the problem. Thermal activation of the PV amplitude at higher temperatures where the time of peak of the PV transient is independent of temperature point to the activation of the PV amplitude

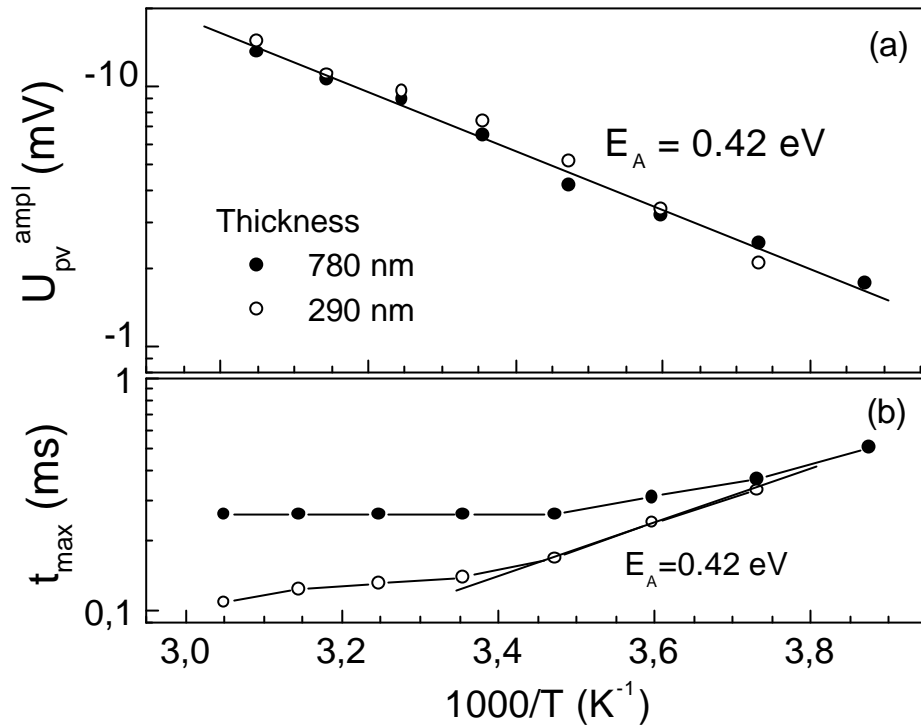


FIG.4.11 Arrhenius plot of the amplitude (U_{pv}^{ampl}) (a) and time of maximum (t_{max}) (b) of the PV for the thick (solid circle) and middle (empty circle) PPV samples.

at the expense of the thermal activation of the charge carrier concentration.

4.7 Conclusion of chapter 4

The two mechanisms of charge carrier separation due to diffusion of excess holes and electrons with different diffusion coefficients and in the built-in electric field are involved into the formation of PV signal in PPV layers. Since the width of the space charge region with the built-in electric field is about 100 nm, the two mentioned mechanisms of the PV formation dominate in the thick or in the thin PPV layers, respectively. The shapes of the PV transients in thick PPV layers are in good agreement with the typical simulated shape of the PV transient obtained from the diffusion PV model. The peak time of the PV depends on the thickness of the layer at a given intensity of illumination and points to the diffusion of charge carriers over the thickness of the PPV layers. The estimated values of D_p and D_n are of the order of $10^{-6} \text{ cm}^2/\text{s}$ and $10^{-7}..10^{-8} \text{ cm}^2/\text{s}$, respectively. The diffusion coefficient of holes increases with

increasing illumination intensity. This can be related to the filling of bandgap states by excess charge carriers in the material with dispersive transport. The diffusion PV is thermally activated with an activation energy E_A for the amplitude of the PV amplitude of 0.42 eV. The diffusion PV method is a powerful tool for the investigation of charge carriers diffusion in PPV and is also applicable to other materials with large t_M .

CHAPTER 5 Trap limited photovoltage in ultrathin metal oxide layers

Metal oxides are wide band gap materials with a large degree of disorder and numerous defects in the forbidden gap. The scattering of free charge carriers by phonons and defects in such materials with small average scattering time may lead to the spatial localization of carriers within the mean free path. The very low value of the charge carrier mobility in metal oxides¹⁰⁴ implies localization and a mean free path of the order of the inter-atomic distance. Such scattering decreases the uncertainty in a particle's position and hence increases its momentum (energy) uncertainty. The energy spectrum of the charge carriers changes.

The electronic states in the forbidden gap of metal oxides films are crucial for the charge carrier transport. For example, the importance of defects for electronic transport has been shown for TiO₂ films¹⁰⁵ and Ta₂O₅ layers.¹⁰⁶ The conductivity and mobility of nanoporous TiO₂ films change over several orders of magnitude depending on the ambient conditions (vacuum, oxygen, water) by means of the change the electronic states distribution or dielectric screening of the barriers. The electrically based sensor applications of metal oxides are well known.¹⁰⁷

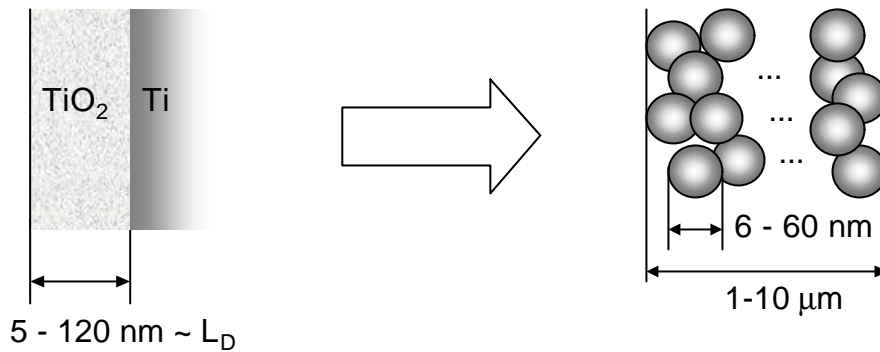


FIG.5.1: Ultrathin anodic TiO_2 layer as a model system for the investigation of transport properties of a “nanoparticle”.

The ultrathin metal oxide layers are suitable objects for the investigation of the charge carrier separation on a nanometer scale. Such charge carrier separation is a constituent part of the transport in nanoporous materials which consists of inter- and intra-particle parts and involves a number of additional factors. Figure 5.1 compares typical sizes of the used ultrathin metal oxide layers with thickness range 5-120 nm (left hand side) and nanoporous TiO_2 film with size of nanoparticles 6 - 60 nm and film thickness 1-10 μm (right hand side). The values of mobility of electrons is several orders of magnitude smaller for nanoporous TiO_2 in comparison to the bulk one.^{6,108} Therefore, ultrathin metal oxide layers can serve as a model system to investigate the role of electronic states for intra-particle transport which may be useful for a better understanding of the electric transport in a network of interconnected nanoparticles.

The electronic state distribution within the band gap and the transport properties of ultrathin metal oxide layers are important for applications. For, example, ultrathin metal oxide layers are novel promising high- k dielectrics for electronics.¹⁰⁶ The metal oxide layers with high dielectric constant are candidates for new gate oxide in MOSFETs. The increase of the dielectric constant relative to the SiO_2 (usual gate dielectric) permits the use of thicker films to obtain the same effective capacitance as with thinner SiO_2 dielectrics. The use of *high- k dielectrics* allows to increase the capacitance of gate dielectrics and prevent direct tunneling at the same time. However, leakage currents via tunneling assisted by traps in the forbidden gap is a limiting factor for the device performance.

Despite of great applied and fundamental interest, little is known about

the relation of the electronic states in the band gap to the basic transport properties of such nanoscale materials. There are only few experimental techniques allowing to obtain information about the electronic states in ultrathin metal oxides. As known, a photovoltage (PV) arises whenever excess charge carriers are separated in space. For example, the separation of a negatively and of a positively charged sheets with a density of only 10^{10} cm^{-2} by 1 nm would cause a reasonable voltage drop of the order of 100 μV . The PV measurements have the advantages to be contactless and to give information about the energy position, type of states, trapping/detrapping times of the traps via the light absorption and spatial charge carrier separation. This makes PV measurements more universal than other techniques like photoelectron spectroscopy¹⁰⁹ or internal electron photoemission.¹¹⁰

In this work we apply the transient photovoltage¹¹ and spectral photovoltage¹³ techniques to characterize trap states in ultra thin metal oxide layers. Several metal oxide layers (TiO_2 , Cu_2O , ZnO) with different dominating traps (hole traps, electron and hole traps, electron traps, respectively) are investigated. A model of the PV formation due to electronic states in the forbidden gap (trap-limited PV model) is proposed. The relaxation of the trap-limited photovoltage signal including recombination of spatially separated excess carriers due to tunneling at lower temperatures and thermal emission at higher temperatures is developed for the case when only one type of charge carriers is predominantly trapped in the metal oxide layer. The accent of investigation will be made on the ultrathin TiO_2 layers, while other materials will be used to show the generality of the phenomenon of trap limited photovoltage in ultrathin metal oxide layers with band gap states.

5.1 Formation of the photovoltage

5.1.1 Preferential trapping of electrons or holes

Figure 5.2 shows typical PV transients for different ultrathin metal oxide layers (TiO_2 , Cu_2O , ZnO) on the respective metal substrates. The PV transients were excited by light with photon energy above the band gap of the metal oxides (3.42¹¹¹, 2.0¹¹² and 3.3¹¹³ eV for TiO_2 (anatase), Cu_2O and ZnO , respectively). Depending on the metal oxide, the PV signal can be positive (TiO_2) or negative (ZnO) or also may change the sign in time (Cu_2O). A positive (negative) PV signal means that negative

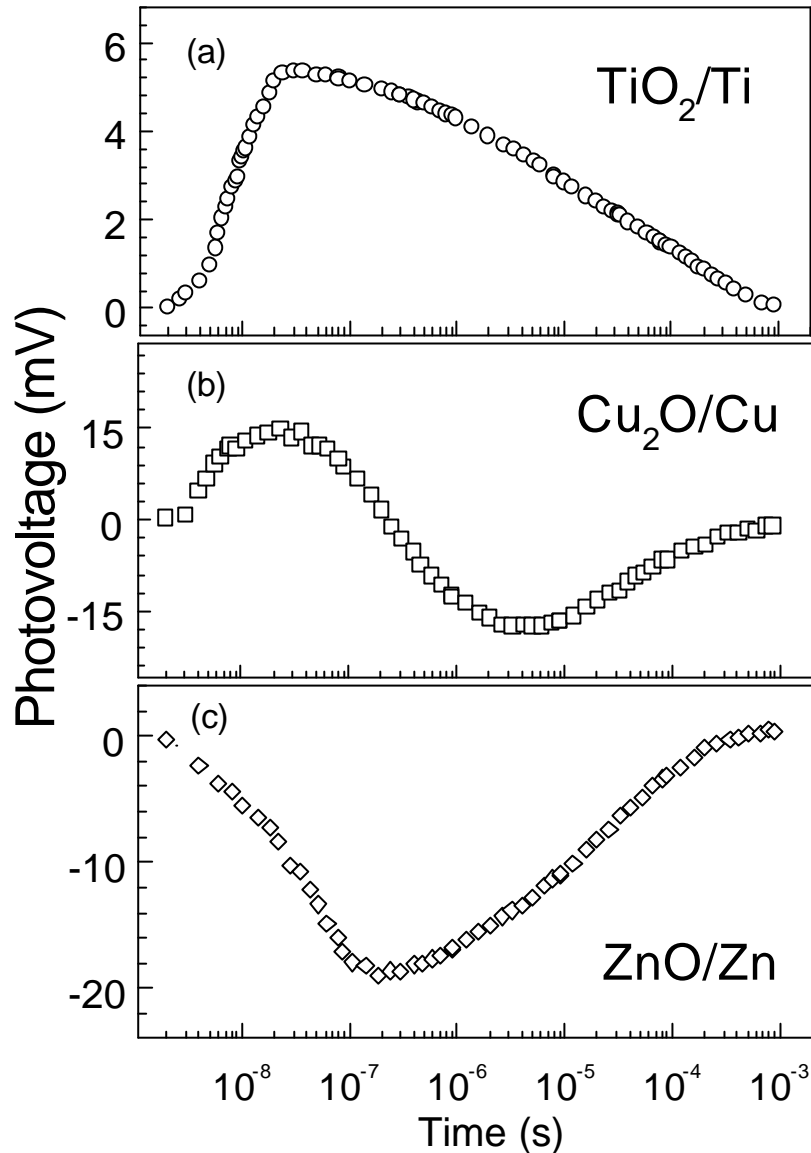


FIG.5.2: Photovoltage transients for ultrathin layers of TiO_2 (a), Cu_2O (b) and ZnO (c) at the Ti, Cu and Zn metal substrates, respectively.

(positive) charge carriers are moving towards the metal surface (due to the band offset at oxide/metal interface) so that preferentially positive (negative) charge carriers stay trapped in the ultrathin metal oxide layer.

In the usual case, both electron and hole traps are present in metal oxides, but their concentration, distribution, and thermal cross-sections may be very different. The PV signal would not appear if both electrons and holes are trapped homogeneously in the metal oxide layer. For example, for the ZnO layer the maximum of the negative PV signal is reached only after about 200 ns (for comparison, the duration time of the laser pulse was 5 ns) what gives an imagination about the release time of trapped holes in this case. In difference, there are no traps for electrons

or there are some with a very short release time (in comparison to the duration of the laser pulse) in the TiO₂ layer. The situation is more complicated in the Cu₂O layer where the concentration of trapped holes is larger than the concentration of trapped electrons at the shorter times but where the release time is much shorter for the holes.

The formation of the PV signal within the duration of the laser pulse in the ultrathin TiO₂ layer allows to estimate the lower limit of the mobility of electrons μ_n . The excess electrons escape from the thickness of the layer of 10 nm within (or faster) the duration of the laser pulse of 10 ns, the estimated mobility is $\mu_n > 4 \cdot 10^{-3} \text{ cm}^2/\text{Vs}$.

Surface states at the metal oxides are changed immediately with changing the ambient gas atmosphere (air, vacuum, adsorbed water, oxygen).¹¹⁴ However, the PV signal in TiO₂ layer did change only very slowly during prolonged storage time after changing the ambience. This demonstrates that the traps being responsible for the formation of the PV signal in ultrathin TiO₂ layers are not related to the free surface of the metal oxides.

5.1.2 Limitation of the photovoltage amplitude

The intensity dependence of the absolute values of the PV amplitude for the TiO₂ and ZnO layers is shown in Figure 5.3. The dependence is a linear function of the intensity for small excitation level and obeys a square root dependence at higher intensities. A linear dependence of the PV signal on the excess carriers concentration is considered in the small signal case. The concentrations of electrons n and holes p under illumination with absorption coefficient a and intensity I can be given by the continuity equations:

$$\frac{dn}{dt} = -\gamma np - \frac{n}{\tau_l} + aI \quad (5.1a)$$

$$\frac{dp}{dt} = -\gamma np + aI \quad (5.1b)$$

where the terms on the right hand side of equation (a) are the bimolecular recombination with coefficient γ , decrease of the electron concentration due to escape into the substrate with characteristic time τ_l and the optical generation.

The PV is created by the non-compensated charge carriers $p - n \approx n_b$, which is obtained from the difference in (5.1a) and (5.1b):

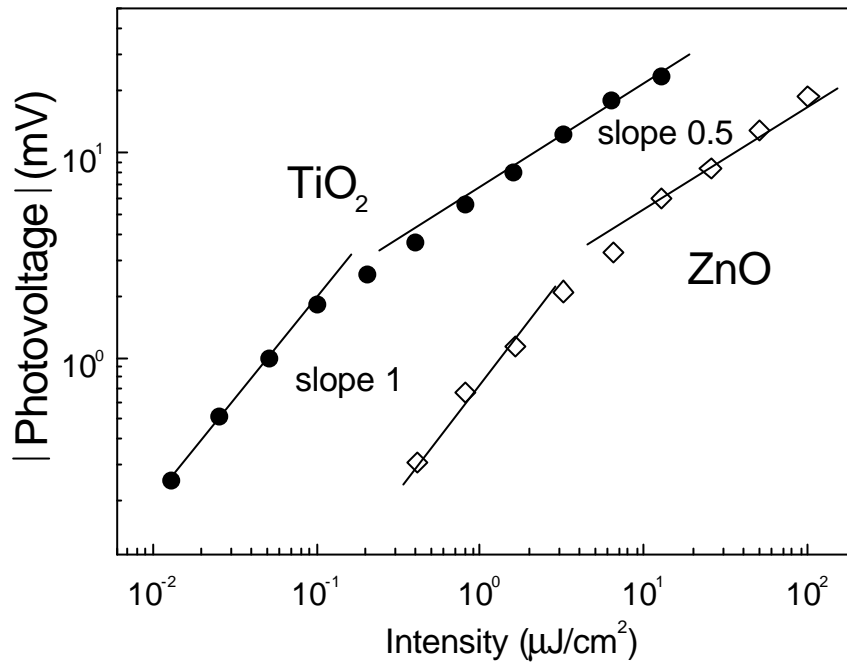


FIG.5.3: Dependence of the absolute value of the PV amplitude on the excitation intensity for the TiO_2 and ZnO layers.

$$\frac{dn_l}{dt} = \frac{n}{t_l} \quad (5.2)$$

where n_l is the concentration of the electrons which are escaped from the layer until the time t is reached.

Substitution of the n_l into steady-state equation (5.1a) with neglecting the second term produces a quadratic equation with two solutions:

$$n = -\frac{n_l}{2} \pm \frac{1}{2} \sqrt{n_l^2 + \frac{4aI}{g}} \quad (5.3)$$

where the negative solution has no physical meaning.

The neglect of the n/t_l term in comparison to the γnp term in (5.3.1a) means that the electron concentration decreases rather due to the bimolecular recombination than due to the escape into the substrate. The steady-state equation can be taken in the case when the time of bimolecular recombination is much faster than the duration of the illumination pulse.

The equation (5.2) with the electron concentration (5.3) gives the differential equation:

$$\frac{dn_l}{\left(\sqrt{n_l^2 + \frac{4aI}{g}} - n_l\right)} = \frac{dt}{2\tau_l} \quad (5.4)$$

which after multiplication on the conjugated term and normalization of the concentration $x = \frac{n_l}{\sqrt{4aI/g}}$ is obtained as:

$$\left(\sqrt{x^2 + 1} + x\right) dx = \frac{dt}{2\tau_l} \quad (5.5)$$

The solution of this differential equation has a form $n_l = \sqrt{\frac{4aI}{g}} f\left(\frac{t}{\tau_l}\right)$, where $f(t/\tau_l)$ is a function of time. Therefore, the square root dependence of the excess carrier concentration n_l , and therefore of the PV in assumption of a small signal case, on the excitation intensity I is determined by limitation due to bimolecular recombination.

5.1.3 States in the forbidden gap

The discussed mechanism of the PV formation in ultrathin metal oxide layers demands the presence of the electronic states in the bandgap of metal oxide which act as trapping centers. Figure 5.4 depicts the spectral dependent PV for the different ultrathin metal oxide layers (TiO₂, Cu₂O, ZnO) on the respective metal surfaces. The PV signals were normalized to the photon flux. The sign of the spectral dependent PV at 3.7 eV is in agreement with the sign of the transient PV signal for the TiO₂ and ZnO layers. The appearance of the PV at around 3.15 eV for the TiO₂ layer implements the existence of electronic states essentially below the band gap of anatase. The positive sign of the PV below the bandgap of the TiO₂ implements excitation of electrons on the delocalized states where they are able to move, excitation of electrons from the occupied acceptor states to the conduction band, or from the valence band to the empty donor states can be discussed in these cases. At the latter transition, transport of excess electrons via localized states by means of hopping, trap-assisted tunneling or tunneling should be possible. The energy of the exponential tail below the band gap is $E_0^{\text{TiO}_2} = 80 \text{ meV}$ for the ultrathin TiO₂ layer what is in very good agreement with measurements on porous TiO₂ layers by spectral photoconductivity^{115, 116} or PV.¹¹⁴

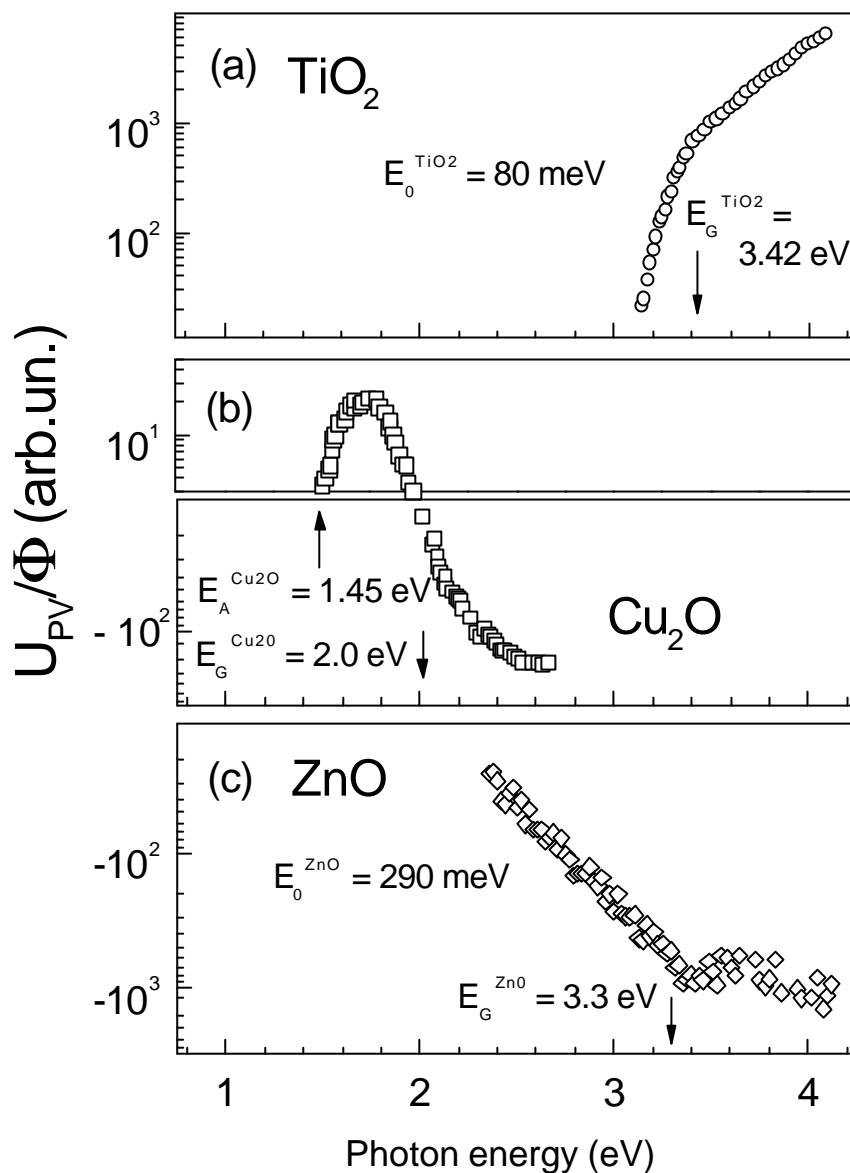


FIG.5.4: Photovoltage spectra for the TiO_2 (a), Cu_2O (b) and ZnO (c) layers.

The exponential tails are more extended in the ultrathin ZnO layer ($E_0^{\text{ZnO}} = 290 \text{ meV}$) than for the TiO_2 layer. As remark, $E_0^{\text{ZnO}} > 100 \text{ meV}$ due to the high density of high-angle grain boundaries was found for 150 nm thick ZnO films.¹¹³ The exact value of E_0^{ZnO} is controlled by the lattice mismatch of the ZnO layer and substrate and is usually much lower for thick ZnO layers.¹¹³ The valence band - donor transition at 3.15 eV which sometimes was considered as a band gap value of ZnO due to the domination in absorption may also smear the tails.

For the Cu_2O layer, the PV signal is positive for excitation with photon energies below the band gap and negative when the energy of the

exciting photons is above the band gap (2.0 eV). The positive PV signal which appears at 1.45 eV can be attributed to the electron transition from the occupied states above the valence band to the conduction band from where the electrons can easily reach the metal surface. The conductivity is controlled by an acceptor-type level at 0.54 eV above valence band which is compensated by a donor-type level at 0.92 eV below the conduction band in the Cu₂O films.¹¹² An activation energy of 0.55 eV was found from thermostimulated conductivity and is related to the excess Cu vacancies.¹¹² The negative PV signal for excitation with the photon energy above the band gap results from the shorter detrapping time of holes as can be seen from the PV transient (Fig.5.2b).

5.2. Relaxation of the photovoltage

5.2.1. Recombination of spatially separated charge carriers

The model of the PV formation in ultrathin TiO₂ layers implies the trapping of holes with long detrapping time (in comparison to the time of measurements) and injection of electrons into the Ti substrate. The decay of the PV is possible due to the recombination of the spatially separated electrons and holes in this case. The overlap of the electron and hole wave functions determines the recombination rate of spatially separated charge carriers (spatially dependent recombination).

The model of the PV decay due to spatially dependent recombination was developed in Chapter 1. The condition of homogeneous trapping of holes is satisfied due to the comparable thickness of the TiO₂ layer ($d=20$ nm) and absorption length of the light at 3.7 eV ($\alpha^{-1} = 10$ nm). Therefore, the equation (1.4.5) can be applied to the analysis of the decay of the PV transients. The measured (open circles) and calculated with equation (1.4.5) (line) PV transients of the TiO₂ layer are plotted in Figure 5.5. The dielectric constant $\epsilon = 30$ is used for the calculation. The measured and simulated transients decay linearly in $\ln^2(I+t/t)$ units for $t > t$. The value of trapped hole concentration p_0 can be found from the PV amplitude which is given by $U_{pv}^{ampl} = ep_0d^2/2\epsilon\epsilon_0$. From the fit of the measured PV transient one gets the values of the Bohr radius of the trapped hole ($a = 2.8$ nm), the initial concentration of the trapped holes ($p_0 = 2.5 \cdot 10^{16}$ cm⁻³ for the case shown in Figure 5.5) and the lifetime without spatial separation ($t = 0.4$ ns). For the relaxation of the PV

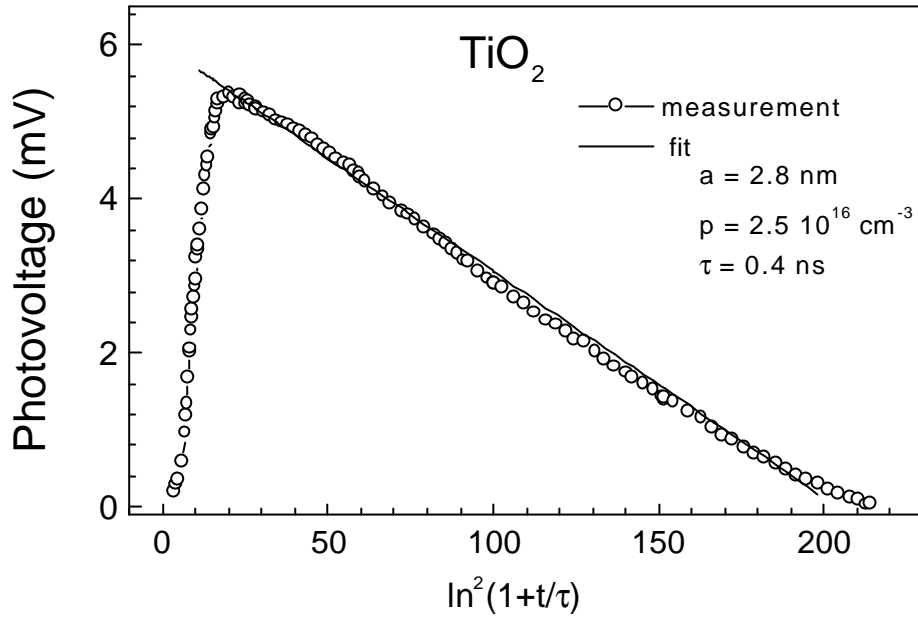


FIG.5.5: Measured (open circles) and simulated by equation (1.4.5) (line) PV transients for the TiO_2 layer. Simulations are made according to the spatially dependent recombination model with parameters $p_0 = 10^{16} \text{ cm}^{-3}$, $a = 2.8 \text{ nm}$, $\tau = 0.4 \text{ ns}$.

transients in ZnO or Cu_2O layers a simple model as in equation (1.4.5) can not be given.

5.2.2 Role of thermal emission at higher temperatures

For increasing temperature, thermal emission becomes important for the relaxation of the separated charge and a thermally activated time constant (detrapping time \mathbf{t}_d) appears. The rates of thermal generation and recombination processes are briefly discussed by means of Shockly-Read-Hall statistics in Chapter 1.4.4. The concentration of the trapped holes in the case of thermal emission can be described by

$$p(t) = p_0 \cdot \exp\left(-\frac{t}{\mathbf{t}_d}\right) \quad (5.6)$$

with

$$\mathbf{t}_d = \mathbf{t}_d^0 \cdot \exp\left(\frac{E_A}{kT}\right) \quad (5.7)$$

where E_A is the activation energy and \mathbf{t}_d^0 is the pre-exponential factor.

In the case that the relaxation of the excess carrier concentration is determined by tunneling and emission, p_0 in equation (1.4.5) has to be

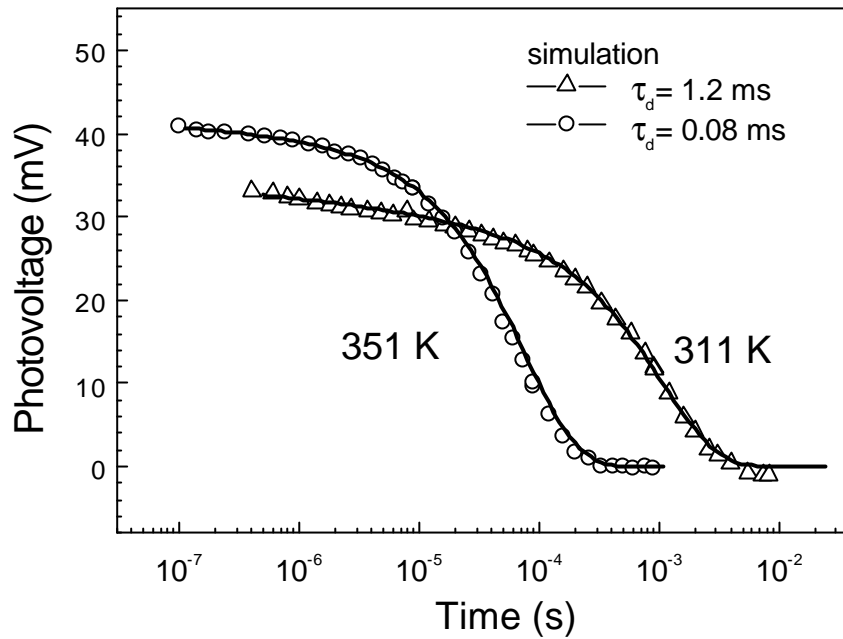


FIG.5.6: Measured (symbols) and simulated (lines) PV transients for the TiO_2 layer at two temperatures. Thermal emission of holes (detrapping times of $t_d = 1.2$ and 0.08 for 311 and 351 K, respectively) is included into the spatially dependent recombination model. The other parameters of the simulated PV transients are: $p_0 = 1.5 \dots 2 \cdot 10^{17} \text{ cm}^{-3}$, $a = 2.8 \text{ nm}$, $t = 0.4 \text{ ns}$.

replaced by $p(t)$ from equation (5.6). Figure 5.6 shows measured (symbols) and simulated (lines) with the model of spatially dependent recombination at short times and thermal emission at long times PV transients for the TiO_2 layer at 311 and 351 K. The PV transients decay with the logarithmic law to the second power at shorter times ($t < t < t_d$, the parameters of the model: $p_0 = 1.5 \dots 2 \cdot 10^{17} \text{ cm}^{-3}$ (depending on the temperature), $a = 2.8 \text{ nm}$, $t = 0.4 \text{ ns}$) and become shorter with increasing temperature. The exponential decay of the PV transients at long times ($t > t_d$) is well fitted by the t_d values of 0.08 ms and 1.2 ms at 351 K and 311 K , respectively. Therefore, the decay of the PV transient at higher temperatures is caused by thermal emission of holes trapped in the TiO_2 layer. The PV amplitude increases with increasing temperature indicating to a partial compensation of trapped holes by trapped electrons which disappear much faster than the trapped holes with increasing temperature. The trapping of electrons in the TiO_2 layer which partially compensates the trapped holes will be shown below.

The Arrhenius plot of the detrapping time for holes at two illumination intensities in ultrathin TiO_2 layer is shown in Figure 5.7. The activation

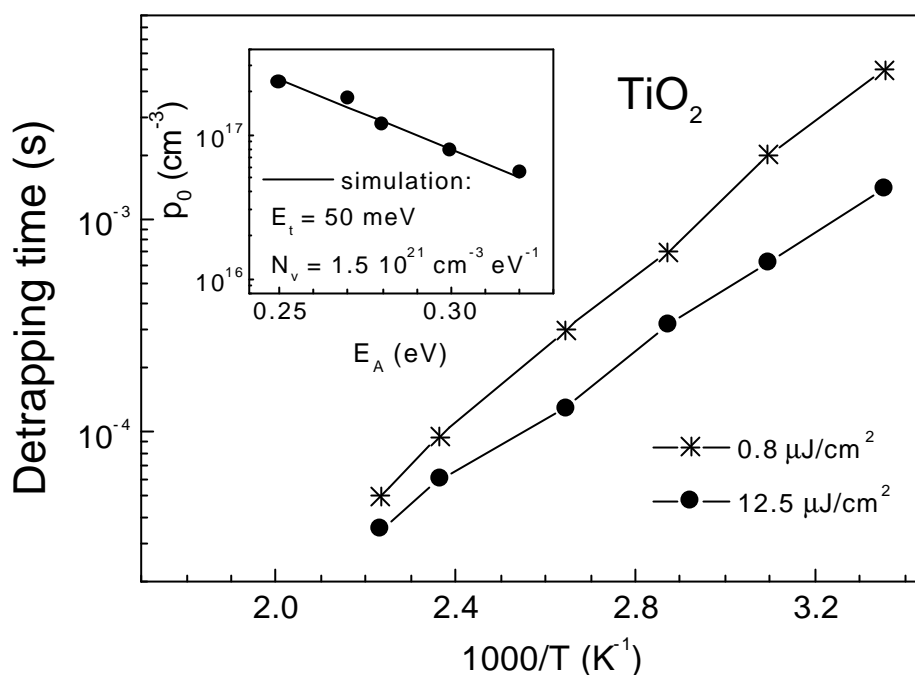


FIG.5.7: Arrhenius plot of detrapping times for holes of the TiO_2 layer. The insert shows the correlation between the activation energy of the detrapping time and p_0 .

energy E_A increases from 0.25 eV to 0.32 eV with decreasing intensity of the exciting light from $12.5 \mu\text{J}/\text{cm}^2$ to $0.8 \mu\text{J}/\text{cm}^2$. As remark, the barrier of 1.3 eV⁴¹ between the TiO_2 and the Ti is much higher than E_A and therefore the recombination of the electrons and holes due to the emission of electrons from the Ti into the TiO_2 layer can be neglected for the relaxation of the PV.

The activation energy of the detrapping time coincides with the energy position of the traps due to the SRH statistics in the case of a single level. The decrease of the energy level of hole traps with increasing concentration of the excess holes follows from the experimental data what is possible in the case of energy distribution of the hole traps. This energy distribution can be derived from the correlation of the activation energy of detrapping time E_A and excess hole concentrations p_0 at given values of the illumination intensity. The excess hole concentration p_0 at different excitation intensities are taken from the intensity dependence of the PV amplitude (Fig.5.3) at room temperature. The linear dependence of the PV amplitude on the excess hole concentration follows from the model. The activation energy of the detrapping time for holes is taken from the Fig.5.7. The insert of Figure 5.7 shows the correlation between hole concentration and activation energy, the illumination intensity is

taken as a correlation parameter. One should remark that the exact value of p_0 is not known due to the partial compensation by trapped electrons. For the given temperature range, p_0 did increase by up to 40% from room temperature to 450 K.

In the case of an exponential distribution of hole trap states ($P(E)=N_V \exp(-(E-E_V)/E_{t(V)})$, exponential tail at the valence band edge E_V) which gives the satisfactory fit of the experimental data, the parametrical dependence between p_0 and E_A can be used to obtain the tail parameter ($E_{t(V)}$) and the density of states at the valence band (N_V). The values of $E_{t(V)}$ of 50 ± 10 meV and N_V of 10^{21} eV⁻¹cm⁻³ are found from the slope of the $\ln p_0(E_A)$ and from the intersection with the concentration axis, respectively. The value of $E_{t(V)}$ (50 meV) is significantly below $E_0^{\text{TiO}_2}$ (80 meV) which has been obtained from the spectral dependent PV measurements. This difference is not surprising since the spectral dependent PV measurement is sensitive to the combination of the exponential tails at the valence and conduction bands while t_d is sensitive only to the exponential tail at the valence band.

The pre-exponential parameter in equation (5.7) is given by the effective density of states at the valence band (N_0), the thermal velocity of carriers (v_{th}) and the thermal cross section of trap (\mathbf{s}): $(t_d^0)^{-1} = \mathbf{s} N_0 v_{th}$. The experimentally obtained value of $(t_d^0)^{-1}$ is $5 \cdot 10^8$ s⁻¹. If taking a thermal velocity of hole with free electron mass, one would obtain a capture cross section for holes in ultrathin layers of anodic TiO₂ of the order of $3 \cdot 10^{-18}$ cm². Such low values of the thermal cross-section is typical for scattering on the neutral centers due to the near field interacting forces between the charge and neutral center.¹¹⁷

5.3 Electron traps in ultrathin TiO₂ layers

Figure 5.8 shows PV transients for ultrathin anodic TiO₂ film at high temperatures in vacuum ($p = 10^{-2}$ mbar). The sample was cooled down to 100 °C after heating up to 290 °C. The decay of the PV transients becomes shorter at higher temperatures due to the discussed above thermal activation of trapped holes. The most striking feature of the PV behavior with increasing temperature is the decrease of the PV amplitude at higher temperatures and even the change of the PV sign from positive to negative at about 290 °C. The reason for the negative PV at high temperature is the preferential trapping of electrons inside the metal oxide layer. The density of electron traps should be smaller than

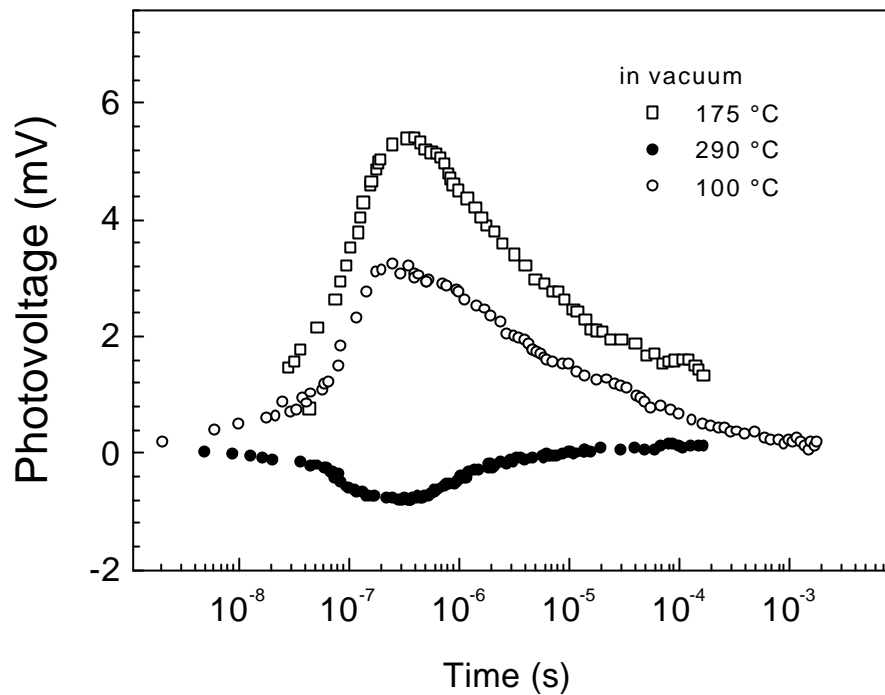


FIG.5.8: Typical PV transients for ultrathin TiO_2 film at high temperatures.

the density of hole traps what follows from the positive signal of the PV at lower temperatures. The remaining filled electron traps are deeper than the hole traps. Therefore, the detrapping of holes proceeds more efficiently than detrapping of electrons at high temperatures.

The change of the PV sign from negative to positive after the cooling of the sample down to $100\text{ }^\circ\text{C}$ is the evidence of the thermal activation of the detrapping process. However, the reproducibility of the PV transients is not absolute. The amplitude of the PV transient at $100\text{ }^\circ\text{C}$ is smaller in comparison to the amplitude at $175\text{ }^\circ\text{C}$ before the heating up to $290\text{ }^\circ\text{C}$. The additional creation of the electron traps at high temperatures in vacuum should also be considered.

5.4 Transition from the trap-limited to diffusion PV

A homogeneous spatial distribution of hole traps was assumed in the model and the decay of the PV was in good agreement with the simulations. This assumes that not only homogeneous light absorption but also the diffusion length of electrons is larger than the thickness of the layer what was the case of the layers with small thickness. The

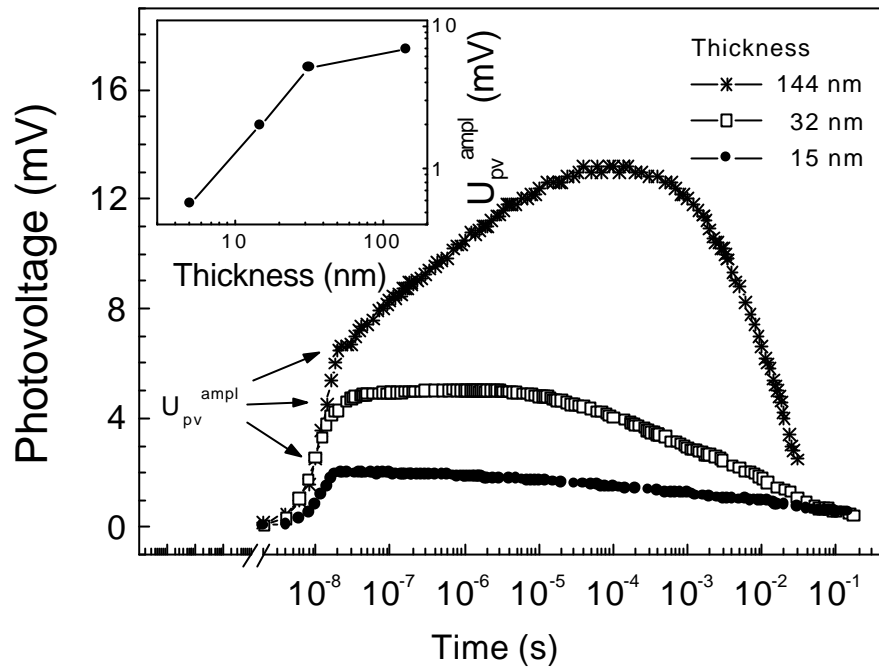


FIG.5.9: Typical photovoltage transients for anatase films of different thickness. The inset shows the dependence of the fast component of the PV on the thickness of the films.

thickness of the anodic layer can be varied by the preparation conditions. Figure 5.9 shows typical PV transients for thin anodic TiO_2 layers of different thickness. The structure of the anodic TiO_2 layer becomes porous for thicker samples. While only a fast increasing component and a slow decay are present for thin layers (15 nm thickness), the retarded PV signal appears for thick (144 nm thickness) layers. A gradient of concentration is present in thick layer and diffusion of charge carriers becomes important for their separation. The retarded component has the same origin as discussed for porous materials in Chapters 3,4. The constant level of the PV from about 10 ns to 5 μs is caused by the superposition of the processes of spatially dependent recombination (decrease of the PV) and additional diffusion of the electrons and injection into the Ti substrate (increase of the PV).

The inset in Figure 5.9. shows the dependence of the fast component of the PV amplitude on the thickness of the layers. The linear dependence at smaller thickness (5 – 32 nm) shows that the PV is created by the charge generated in the layer and all excess electrons are able to escape into the Ti substrate, the diffusion length of electrons is of the order of 30 nm. The dependence deviates from the linear for larger thickness (144 nm). The decrease of the PV despite of the larger possible distance

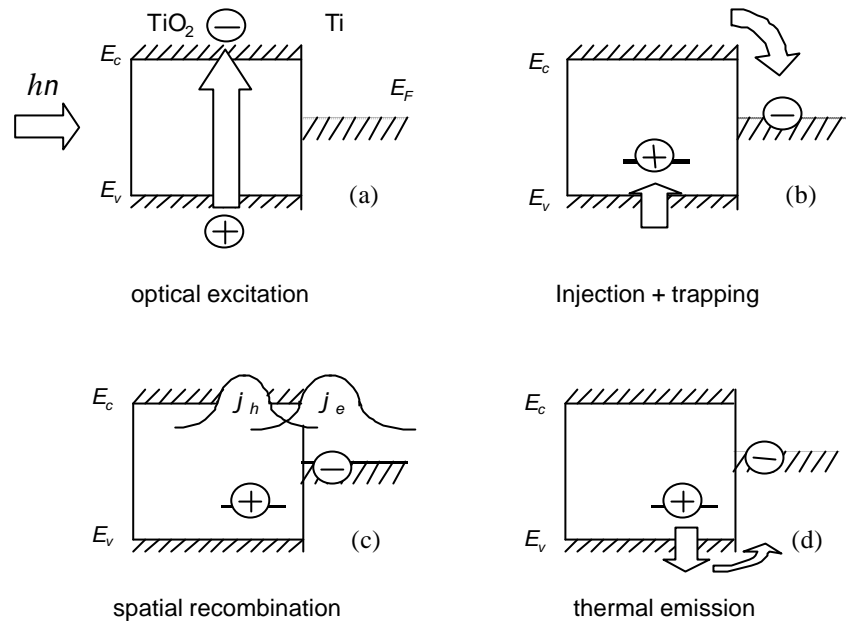


FIG.5.10: Overview of the elementary processes of the trap limited PV in case of preferential hole trapping in the metal oxide layer.

for separation shows the decrease of the excess charge carrier concentration, probably, due to the recombination and smaller diffusion length of electrons than the given thickness. This decrease may be caused by the porous structure of the thick layer.

5.5 Conclusion of chapter 5

Photovoltage signals were observed at ultrathin metal oxide (TiO₂, Cu₂O, ZnO)/ metal structures by transient and spectral photovoltage techniques. The PV is shown to be a general phenomenon for ultrathin metal oxides. The sign, the spectral behavior and the time- dependent relaxation of the PV are determined by the nature of the traps in the metal oxide layers. The time of formation of the PV signal is comparable with the duration of the laser pulse in the ultrathin anodic TiO₂ layers which gives an estimation for the mobility of electrons $\mu_n > 4 \cdot 10^{-3} \text{ cm}^2/\text{Vs}$ and more retarded for Cu₂O and ZnO layers. Figure 5.10 summarizes the elementary processes for the case of preferential hole trapping in the metal oxide. Excess electrons and holes are generated during illumination with photon energies hn larger than the band gap

(figure 5.10a). Excess electrons are injected into the metal substrate and excess holes are preferentially trapped (figure 5.10b). This leads to the formation of the PV signal. The amount of trapped charge is limited by bimolecular recombination at high excitation intensities. At lower temperatures, the decay of the PV is determined by the overlap of the wave functions for electrons (ϕ_e) and holes (ϕ_h) resulting in the recombination of spatially separated excess carriers due to tunneling (figure 5.10c). At higher temperatures, thermal emission accelerates the relaxation of the PV signal (figure 5.10d). This simple model holds for ultrathin anodic TiO₂ layers with dominating hole traps. The Bohr radius of trapped holes, the tail of the exponential approximation of electronic states distribution above the valence band, the density of states at the valence band edge were obtained for TiO₂ layers by using the proposed model of trap limited PV. A more sophisticated model of the PV formation which involve the two types of traps (donor, acceptor) with essentially different detrapping times for the charge carriers is needed for Cu₂O and ZnO layers. With respect to the elementary processes, the trap limited PV can be applied to study electronic states in any ultrathin semiconductor layer with trap states at a metal substrate.

CHAPTER 6 Photovoltage in Nanocrystalline Porous TiO₂

The unique properties of nanoporous TiO₂ promotes its usage in many novel applications. The investigation of basic physical processes involved into the performance of dye-sensitized solar cells,^{2,118} sensors,¹⁰⁷ and photocatalysis¹¹⁹ on the base of nanoporous TiO₂ is of great scientific interest. The skeleton of porous TiO₂ covered by dye molecules is interpenetrated with a chain of a p-type organic polymer material (for example, PPV)¹¹⁸ or immersed into the electrolyte² in dye-sensitized solar cells. The high efficiency of the cells is reached at the expense of the enlarged effective area of the illuminated surface of nanoporous TiO₂ and at the expense of suppressed recombination due to the spatial separation of electrons moving inside the porous TiO₂ matrix and holes or ions moving in the organic polymer or electrolyte. The optimum between the concentration of light induced charge carriers (the concentration is larger for the larger surface area for smaller particles) and transport properties (better for large particles) is reached for a typical size of particles in the range of 10 .. 20 nm. Surface properties of metal oxides are extremely sensitive to the ambient conditions.¹²⁰ The advantages of nanoporous TiO₂ for sensor applications are the enlarged surface area of a porous material⁴ in comparison to the continuous one and reversibility of surface properties by surface conditioning¹¹⁴

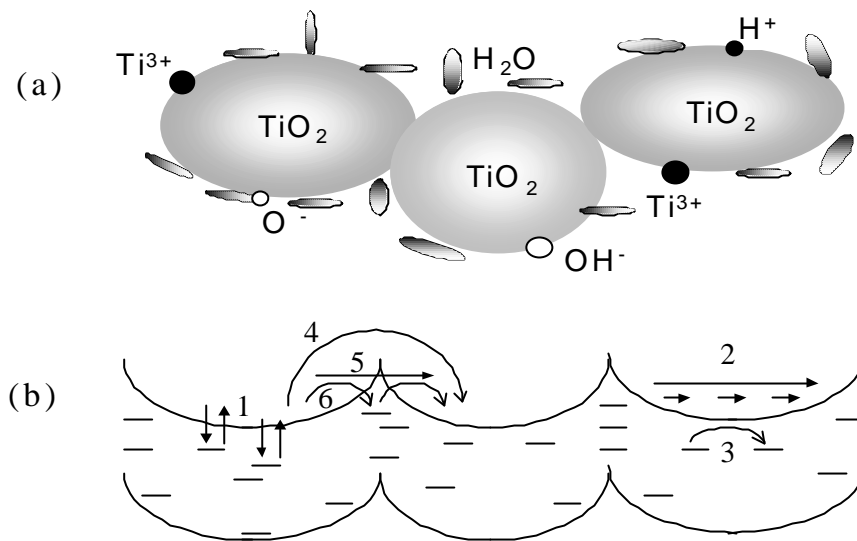


FIG. 6.1 Schematics of the geometry (a) and of the band energy diagram (b) of sintered TiO_2 nanoparticles in wet atmosphere.

(for details of surface conditioning procedure see Chapter 2). The photocatalytic activity of TiO_2 nanoparticles immersed into the electrolyte increases with decreasing diameter of the nanoparticles due to an increase of the surface area and/or due to the modification of electronic states by the quantum confinement effect.⁸ Therefore, the porous structure with a typical size of nanoparticles in the nm range, the high sensitivity of large area surface to the ambiances are the specific features of nanoporous TiO_2 which determine the basic practical applications of this material.

The schematics of the geometry and of the band energy diagram of sintered TiO_2 nanoparticles are shown in Figure 6.1. Nanoporous TiO_2 is characterized by a network of interconnected TiO_2 nanoparticles with a characteristic size in the range of 6 - 60 nm and by an enormous area of a nanoparticle surface (internal surface) of about 1000 - 26 m^2/g , respectively to the size increase.¹²¹ The surface contains Ti^{3+} , Ti^{2+} , Ti^+ and O^- ions due to deviation from the lattice stoichiometry.⁵⁷ The usual atmosphere of ex-situ experiments is wet air. The surface of nanoporous TiO_2 is characterized by the coverage of physically adsorbed water molecules H_2O and chemically adsorbed H^+ and OH^- ions in air. The adsorption and dissociation of water on the surface of crystalline TiO_2 was shown by XPS/UPS¹²² and by first-principle calculations.¹²³

The porous morphology, intrinsic surface defects, surface ions make the electronic properties of nanoporous TiO₂ very different to those of crystalline TiO₂. Up to now little is known about their role for generation-recombination and transport processes of excess charge carriers which determine the basic properties of the dye-sensitized solar cells or electrically based sensors. The transport of excess charge carriers through the sintered network of interconnected nanoparticles consists of intra- and inter-particle parts (Figure 6.1b), the possible influence of inter-particle barriers with different mechanism of transport (tunneling (5), trap-assisted tunneling (6), thermal overcoming (4)) can be discussed. In - situ measurements of the electron drift mobility in porous TiO₂⁶ gave a value which is by 5 - 6 orders lower than the electron Hall mobility in crystalline TiO₂ (rutile,¹²⁴ anatase¹⁰⁸). The electrical conductivity¹⁹ and the radiative recombination in nanoporous TiO₂¹²⁵ depend strongly on the partial pressure of oxygen. Ex-situ (in air) measurements of the conductivity and mobility revealed the Space Charge Limited Current - type of the current-voltage characteristics in nanoporous TiO₂. But the value of the dielectric constant would be unrealistic large if calculating it from the dark- and photo - current values for a constant mobility. The presence of compensating positive charge (H⁺ and/or Ti³⁺ ions) was discussed for the formation of the conductive paths for electrons in nanoporous TiO₂.¹²⁶ At small applied electric field, the transport is dominated by the diffusion of electrons while the applied electric field is screened by the charge of ions (intrinsic oxygen and titanium vacancies, polar water molecules, protons and OH radicals).¹²⁷

Porous TiO₂ belongs to a class of materials with a low electrical conductivity and, therefore, with a large Maxwell relaxation time.¹⁹ Both light absorption and the way of separation of excess carriers of charge, i.e. electronic transport, have to be considered in the interpretation of PV measurements on nanoporous TiO₂. The diffusion photovoltage concept discussed in the previous chapters will be applied to the investigation of optical absorption, electronic surface states and transport of excess carriers of charge in nanoporous TiO₂ layers of different crystalline structure and size of nanoparticles. The contactless photovoltage technique can be easily applied in the different ambiances. The change of surface state density and of related transport properties of excess charge carriers in nanoporous TiO₂ will be shown for air, vacuum, oxygen, or water ambiances.

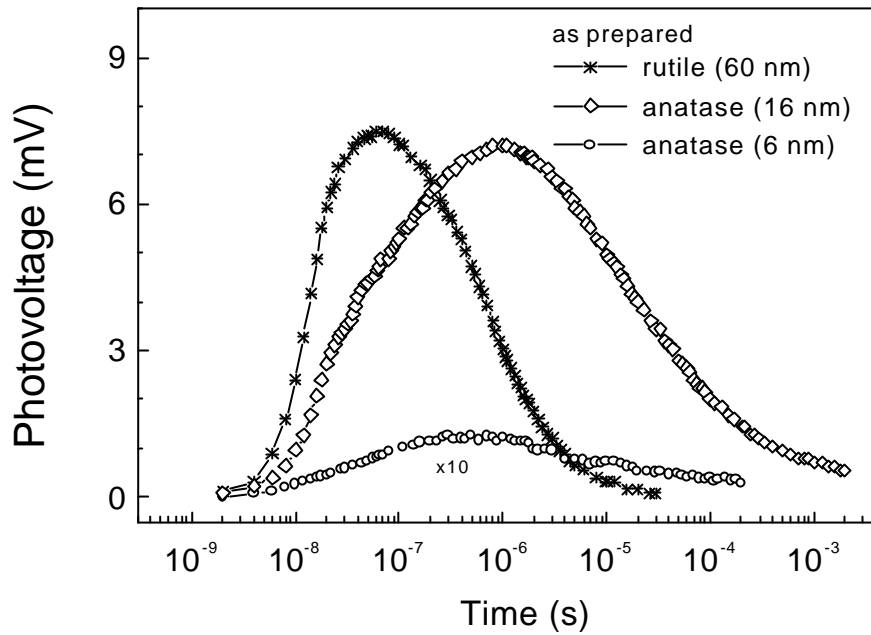


FIG. 6.2: Photovoltage transients for as prepared porous TiO₂ layers of rutile (60 nm), anatase (16 nm) and anatase (6 nm) in air. The excess carriers are excited with photons of $h\nu > E_G$

6.1 Transient photovoltage in well-passivated porous TiO₂ layers

Figure 6.2 shows PV transients for nanoporous TiO₂ layers of rutile (60 nm), anatase (16 nm) and anatase (6 nm) in air. The excess carriers are excited with photons of $h\nu > E_G$. The sign of the PV transients is positive. The positive sign of the PV implies that the photoexcited electrons move faster than holes towards the nanoporous TiO₂/SnO₂:F interface. No PV signal could be detected for $h\nu < E_G$. The PV transients are retarded in time, i.e. the transient PV signal is roughly zero just after the laser pulse and develops within the following 0.1 μ s (rutile) or 1 μ s (anatase). The observed retardation of the transient PV is typical for the diffusion PV in materials with low conductivity. According to our measurements of transmittance in the nanoporous TiO₂ layer of anatase (16 nm) (see below) the adsorption coefficient of the light with $h\nu = 3.75$ eV is in the order of $3.3 \cdot 10^4$ cm⁻¹, i.e the most part of the light is absorbed in the nanoporous TiO₂ layer of $L = 4$ μ m depth. Therefore, the gradient of excess electron and hole concentrations is caused by non-homogeneous absorption of light with photons of $h\nu > E_G$. The spatial separation of the excess electrons and holes with different diffusion

coefficients takes place. The built-in electric field induced by the discontinuity of the material at the top of the layer is very weak in nanoporous TiO₂ due to its high porosity, enormous surface area and negligible concentration of equilibrium charge carriers.

The velocity of the PV (first derivative of the PV in time) can be analyzed from the slope of the experimental PV transients. The photovoltage in the plate capacitor approximation can be written as

$$U = Q/c = e N / (\epsilon \epsilon_0 S / x) \sim N x_c \quad (6.1.1)$$

where Q , c , S are the charge, capacitance and area of the plate capacitor, respectively; N , x_c are the number of non-compensated excess charge carriers and average distance between “center of mass” of electron and hole clouds in the material with the dielectric constant ϵ . The constants e , ϵ_0 have their usual meaning.

The rate of the PV change is:

$$dU/dt \sim d(N x_c)/dt \sim x_c dN/dt + N dx_c/dt \quad (6.1.2)$$

Since there are no reasons to assume a smaller excess charge carrier concentration or its slower decay with time in TiO₂ with smaller particle size, the rate of the PV change describes the velocity of the “center of mass” dx_c/dt and therefore, the transport of the excess charge carriers. Additionally, the mobility of holes is below the experimental possibilities of Time-of-Flight measurements, which supposes at least 2-3 orders of magnitude smaller value in comparison to the mobility of electrons in nanoporous TiO₂.¹²⁷ Therefore, the velocity of the PV can be associated with the transport properties of excess electrons in this case. The higher velocity of the PV in rutile in comparison to the anatase (16 and 6 nm) or anatase (16 nm) in comparison to the anatase (6 nm) shows a larger diffusion coefficient of electrons of first material in respective pairs and can be understood if taking into account the larger mobility of electrons in crystalline rutile in comparison to crystalline anatase^{124,108} and the enlarged amount of slower inter-particle transport. No correlation of the PV peak position with the size of nanoparticles was observed. The time of the PV peak is shorter for anatase (6 nm) than for anatase (16 nm). The reason for the PV maximum in nanoporous TiO₂ will be discussed later.

The intensity dependence of the PV signal in the maximum of the

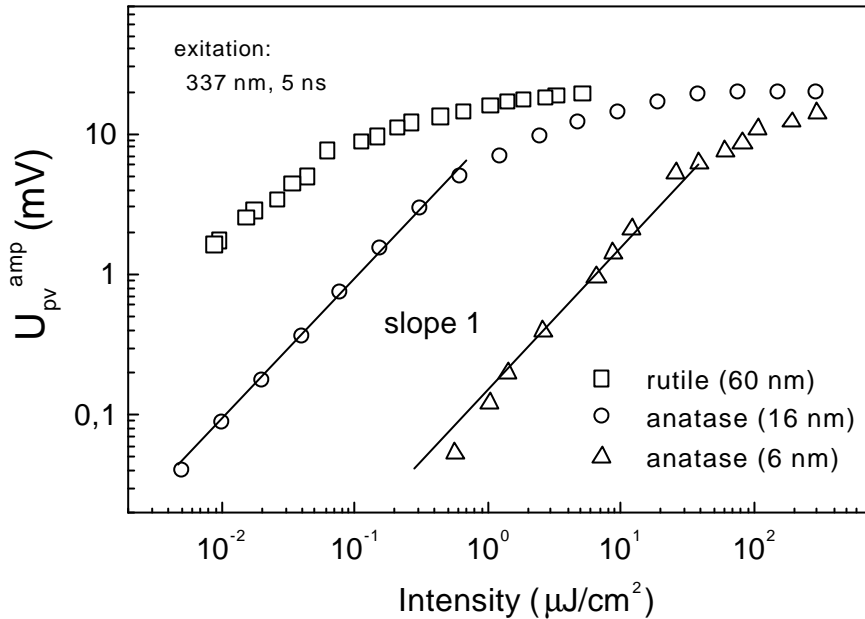


FIG. 6.3: Intensity dependence of the PV maximum for as prepared porous TiO₂ layers of rutile (60 nm), anatase (16 nm) and anatase (6 nm) in air.

transients (U_{PV}^{max}) is given in Figure 6.3. This dependence is linear for smaller excitation intensities and tends to saturate at higher intensities.

The saturation of U_{PV}^{max} at high excitation intensity can be explained by a non-linear increase of recombination losses (Auger recombination and bimolecular radiative recombination) with increasing excess carrier concentration. The saturation of U_{PV}^{max} is reached at smaller intensity for TiO₂ with larger nanoparticle size, while the saturation level is similar. A linear dependence of U_{PV}^{max} on the intensity of the exciting laser pulse is expected for diffusion PV whereas for the Dember PV a logarithmic dependence would be expected. We remark that a linear intensity dependence takes also place for SPV in crystalline semiconductors at very low intensity when the excess carrier concentration is much smaller than the equilibrium carrier concentration. This is not the case in our pulsed PV experiments.

6.2 Spectral photovoltage in well passivated nanoporous TiO₂

Spectra of the PV for as prepared nanoporous TiO₂ layers of rutile (60 nm) and anatase (16 nm) in air are shown in a semi-log scale in Figure 6.4. The spectra are normalized to the photon flux. The PV signals

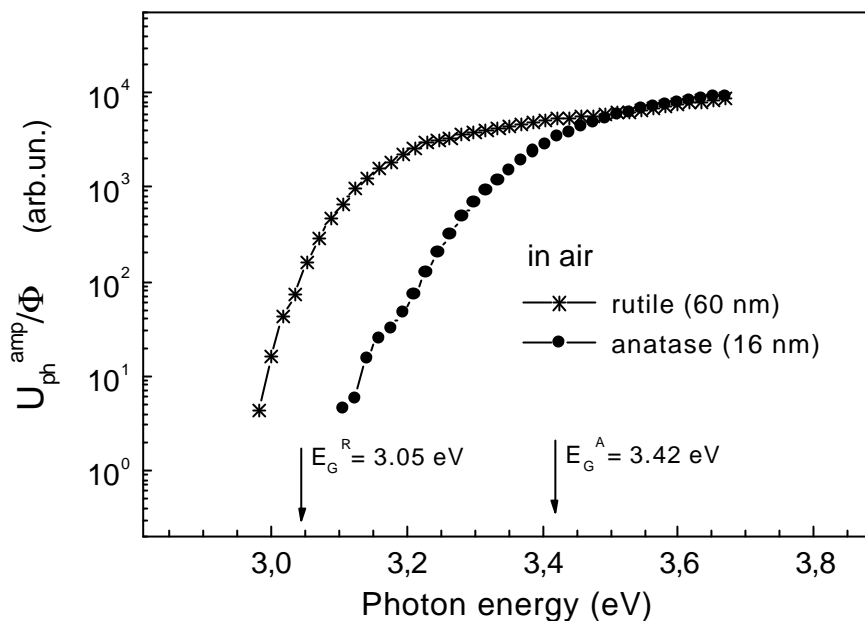


FIG. 6.4: Spectra of the photovoltage amplitude normalized to the photon flux (U_{ph}^{amp}/Φ) for as prepared porous TiO₂ layers of rutile (60 nm) and anatase (16 nm) shown in a semi-log scale.

increase strongly in the regions of the forbidden gap. The value of the optical gap for rutile and anatase single crystals (3.05¹²⁸ and 3.42 eV¹²⁹, respectively) are in good agreement with the position of the kink on the spectral PV dependence. The PV spectrum of the porous anatase contains a pronounced exponential tail below the band gap which is essentially smaller for the porous rutile. The energy of the exponential tail of the PV spectrum of the porous anatase is about 50 meV what is larger than the Urbach-energy of the exponential absorption tails in anatase single crystals (about 40 meV at room temperature¹²⁹). For comparison, the width of Urbach tails is in the order of 78 meV for size of nanoparticles of 4-8 nm in dense layers of anatase (photoconductivity measurements)¹¹⁶ and 65 meV for hydrogenated amorphous silicon at room temperature (absorption measurements).¹³⁰ Therefore, disorder is more important in anatase nanocrystals.

Two processes are responsible for the formation of PV: generation of excess charge carriers and their spatial separation. Therefore, the spectral change of the PV amplitude can be attributed to the spectral dependence of light absorption and/or of transport properties. Figure 6.5 compares the spectral dependence of $(\alpha \times h\nu)^2$, where α and $h\nu$ are the absorption

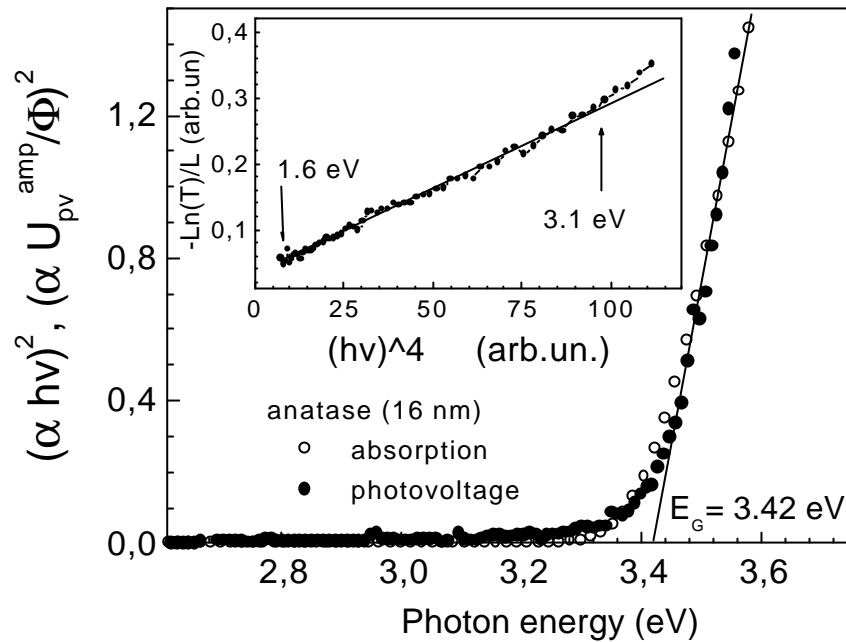


FIG. 6.5: Comparison of the spectra of $(\alpha h\nu \times U_{ph}^{amp}/F)^2$ and of $(\alpha h\nu \times a)^2$ for an as prepared porous TiO₂ layer of anatase (16 nm). The inset shows the interpolation of the $-\ln(T)/L$ (where T , L are the transmittance and thickness of the sample, respectively) by Rayleigh formula (see in text, the size of scattering objects 50 nm) below the band gap of anatase (16 nm).

coefficient and the photon energy, respectively, with $(U_{ph}^{amp}/F \sim h\nu)^2$ for the anatase (16 nm). The absorption coefficient was obtained from the measurements of the optical transmittance (T) of the nanoporous TiO₂ layer on the thin sapphire substrate. The PV data shown in a linear scale were superposed with the absorption coefficient in semi-logarithmic scale by multiplication with a constant. The both curves can be approximated by a linear dependence above the band gap of anatase what is typical for direct band gap semiconductor. The value of the band gap E_G obtained from the intersection of the lines with abscise axis is about 3.42 eV.

We remark that a plot of $(\alpha h\nu)^{1/2}$ (indirect transitions) would give a value of E_G close to 3.2 eV which was also some times reported as the band gap of anatase.² However, the conclusion that nanoporous anatase has direct or indirect gap can not be strictly drawn since the approach of the plot of $(\alpha h\nu)^2$ is also conventional for amorphous semiconductors for which the momentum conservation rule does not strongly held.¹³¹ The plot of $(\alpha h\nu)^2$ vs $h\nu$ was also used successfully for the analysis of

the optical absorption of thin anatase layers prepared by spray pyrolysis for which E_G ranges between 3.56 and 3.75 eV.¹³²

As shown above, in the spectral range from 3.3 to 3.6 eV the amplitude of the PV signal of as prepared nanoporous TiO₂ layers follows the absorption coefficient. Taking into account the linear dependence of the PV signal on the excitation light intensity, this fact, can be explained by a mechanism of the PV formation depending on the concentration gradient of excess carriers. Therefore, the PV signal arises due to the concentration gradient of excess carriers in the porous layer. This makes the spectral PV suitable for the investigation of optical absorption in the case when only one mechanism of the formation of the PV signal is involved.

An essential difference between the value of $-(\ln T)/L$ and U_{PV}^{amp}/F exists below the band gap of nanoporous TiO₂. While the PV signal is zero (below our experimental possibilities of registration), the transmittance is not one in this spectral range. The inset of figure 6.5 compares the spectral dependence of $-(\ln T)/L$ with scattering coefficient (g) calculated by Rayleigh formula. The Rayleigh scattering is a characteristic one for objects with the size smaller than the wavelength of the incident light. The scattering coefficient of Rayleigh scattering can be written as¹³³

$$g = 24 p^3 e_0^2 (e - e_0)^2 / (e + 2e_0)^2 N V^2 / I^4 \quad (6.3)$$

where N , V , e , e_0 , and I are the concentration of scattering objects, volume of one object, permittivity of the scattering medium, permittivity of the ambience and wavelength of incident light in vacuum, respectively. Both spectral curves $-1/L \ln T(h\nu)$ and $g(h\nu)$ are linear in this scale in the spectral range below 3.1 eV. The idea of scattering additionally supports by a “milky” color of the sample at day light illumination. The simulation of the experimental curve produces the diameter of the scattering object $a = (6V/p)^{1/3} = 50$ nm, the agglomeration of the nanoparticles with diameter 16 nm is responsible for the scattering.

6.3 Formation of gap states in nanoporous TiO₂ in vacuum

Figure 6.6 compares spectra of the U_x - and U_y - signals for anatase (16 nm) in air (a) or under vacuum condition at 0.05 (b) and 0.001 (c) mbar.

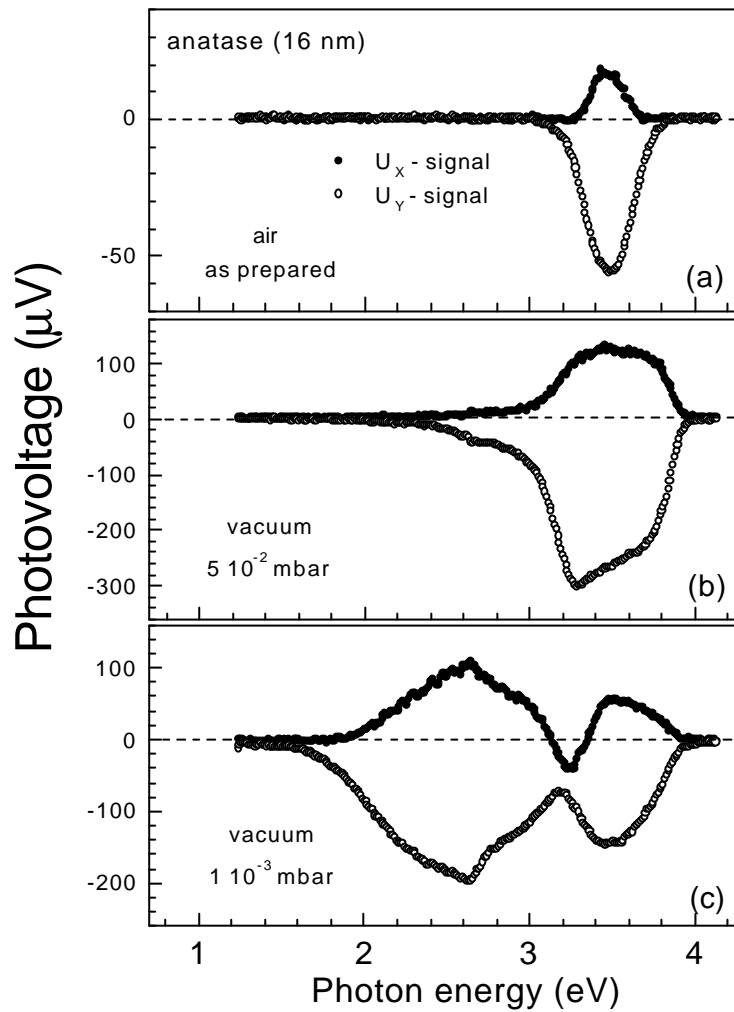


FIG. 6.6: Photovoltage spectra for an as prepared porous TiO₂ layer of anatase (16 nm) in air (a) and in vacuum at 0.05 (b) and 0.001 (c) mbar. The spectra are measured for the x- and y-signals at the lock-in amplifier.

The appearance of the U_x - signal (Fig. 6.6a) at 3.3 eV is consistent with the band gap of anatase and the presence of tail states below the band gap. The disappearance of the U_x -signal at 3.7 eV is caused not only by the spectrum of the lamp but also by the more efficient recombination of excess charge carriers due to decrease of the absorption length of the light and, therefore, the area of excess carrier generation toward the UV range. The tails below E_G are much more pronounced for the U_y - than for the U_x - signal showing that trapping of charge into electronic states in the forbidden gap contributes mostly to the retardation of the PV.

The U_x - signal at $h\nu = 3.5$ eV increases by about 6 times after keeping the sample in vacuum at $p = 5 \cdot 10^{-2}$ mbar (Fig. 6.6b). Further, the spectral range of the U_x - signal for the sample kept at $p = 5 \cdot 10^{-2}$ mbar is extended

to lower and higher photon energies giving evidence, respectively, for generation of defect states in the forbidden gap and for more efficient charge separation in the case of strong absorption (the PV signal is more and more extended to the UV range for higher vacuum pressures). Hence, the generation of electronic states below E_G can sufficiently enhance the charge separation.

The U_x -signal for the layer of anatase (16 nm) at $h\nu = 3.5$ eV decreases twice in comparison to $p = 5 \cdot 10^{-2}$ mbar after keeping the sample at $p = 10^{-3}$ mbar (Fig. 6.6c) and the PV spectrum is dominated by a huge defect peak with maximum at 2.7 eV. Therefore, the concentration of electronic states below E_G increases strongly and the distribution of defect states broadens out with decreasing pressure. The U_x - signal drops sharply and changes in the spectral range from 3 to 3.5 eV. The U_y - signal arises at 1.5 eV and follows mainly the mirrored shape of the U_x - signal but without changing the sign. We remark that the PV spectra are further changing during prolonged storage in vacuum showing that a long time is necessary to reach a chemical equilibrium between formation and annihilation of defect states at the surface of TiO₂.

A change of the sign of the PV signal for the whole range of $h\nu < E_G$ could be realized for the layers of nanoporous TiO₂ (rutile) and nanoporous TiO₂ (anatase, 6 nm) under vacuum condition. Figure 6.7 and Figure 6.8 show the spectra of U_{ph}^{amp}/F and of the phase for the layer of nanoporous TiO₂ (rutile (60 nm)) and nanoporous TiO₂ (anatase (6 nm)), respectively, in vacuum (0.001 mbar). The defect formation in the porous anatase is stronger than for the porous rutile and this process is even accompanied by formation of well defined defect band in the spectral range from 3 to 3.4 eV (Fig.6.8 (a)). The more efficient defect formation in the porous anatase is probably related to the smaller size of nanocrystals (larger internal surface area). Another possible reason for the defect formation in porous anatase is weaker bonding of oxygen in an elementary octahedron of that phase of TiO₂.⁵²

The discontinuity of the phase is located at the position of the band gap for the nanoporous TiO₂ layer of rutile (60 nm) in vacuum. This means that electrons or holes are accelerated toward the back electrode for $h\nu > E_G$ or for $h\nu < E_G$, respectively. The sign of the PV transient (not shown) was also negative for excitation with $h\nu < E_G$. This means that electron traps are preferentially generated in nanoporous TiO₂ (rutile, anatase) under vacuum condition (see inset of Fig.6.7 and Fig.6.8). It can be further concluded, with respect to the PV amplitudes, that the diffusion

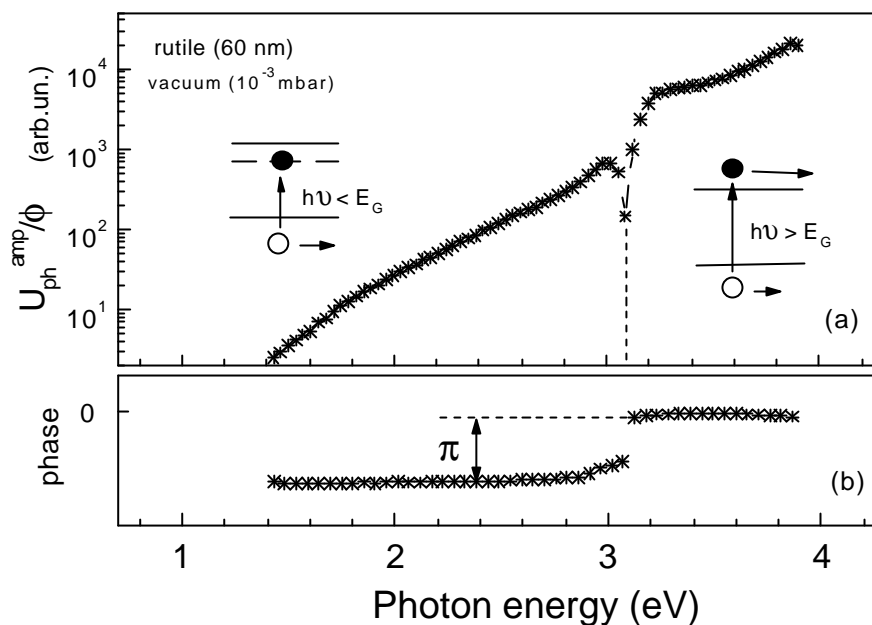


FIG. 6.7: Spectra of the photovoltage amplitude normalized to the photon flux in a semi-log scale (a) and of the phase of the photovoltage signal (b) for porous TiO₂ layers of rutile (60 nm) under vacuum condition (0.001 mbar).

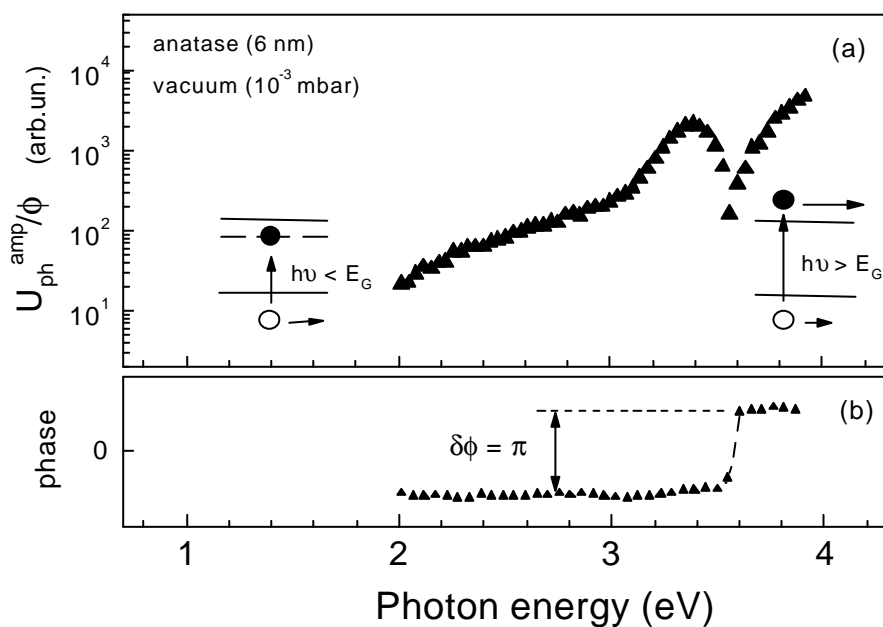


FIG. 6.8: Spectra of the photovoltage amplitude normalized to the photon flux in a semi-log scale (a) and of the phase of the photovoltage signal (b) for porous TiO₂ layers of anatase (6 nm) under vacuum condition (0.001 mbar).

coefficient of excess holes moving in the valence band is lower but not much lower than that for excess electrons moving in the conduction band. The phase is shifted by π at 3.6 eV for the nanoporous TiO₂ layer of anatase (6 nm) (Fig.6.8a). This blue shift of E_G by about 150 meV in comparison to E_G for anatase (16 nm) is caused by the quantum confinement effect⁸ and was also observed by absorption and photoluminescence measurements on TiO₂ nanoparticles used for catalytic reactions.¹²¹ We remark that the photon energy at which the sign of the PV signal changes marks the mobility gap for the electrons.

Further heavily reduced TiO₂ crystals are dark.¹³⁴ The loss of oxygen leads to the formation of donor states in reduced TiO₂.¹³⁵ For rutile single crystals a peak with maximum position of about 0.7 eV below the conduction band edge was measured by photo-electron-spectroscopy on reduced rutile and assigned to oxygen vacancies.¹³⁶ The position of the energy levels of the corresponding defect states in nanoporous TiO₂ stored in vacuum is expected to be in the same order of magnitude (some 100 meV below the conduction band). These states should be considered, in our opinion, as electron traps leading to a change of PV for $h\nu < E_G$.

6.4 Screening of gap states in nanoporous TiO₂ by water

The sub-band gap tails of the PV spectra in nanoporous TiO₂ in vacuum show the electronic transitions under excitation with photon energies below the bandgap. However, the creation of oxygen vacancies at the surface of nanoporous TiO₂ in vacuum due to the desorption of oxygen can not be derived directly from the appearance of the sub-band gap tails. The role of water should be considered in transition from air to vacuum ambiances. Figure 6.9 shows the PV spectra after desorption of water ($p = 13$ mbar) on the nanoporous TiO₂ (anatase 16nm) sample, which was kept in vacuum ($p = 0.001$ mbar) prior to the water desorption. The PV spectrum of the as prepared sample is also shown for comparison. The formation of the extended sub-band gap tail in the PV spectrum in vacuum is analogous to the already described situation in Fig.6.6. The PV signal at $h\nu < E_G$ practically vanished after adsorption of water molecules. This demonstrates the screening of electron surface traps by the polar water molecules or dissociated radicals. The shape of the PV curve at $h\nu > E_G$ repeats the shape of the PV spectra for as prepared sample.

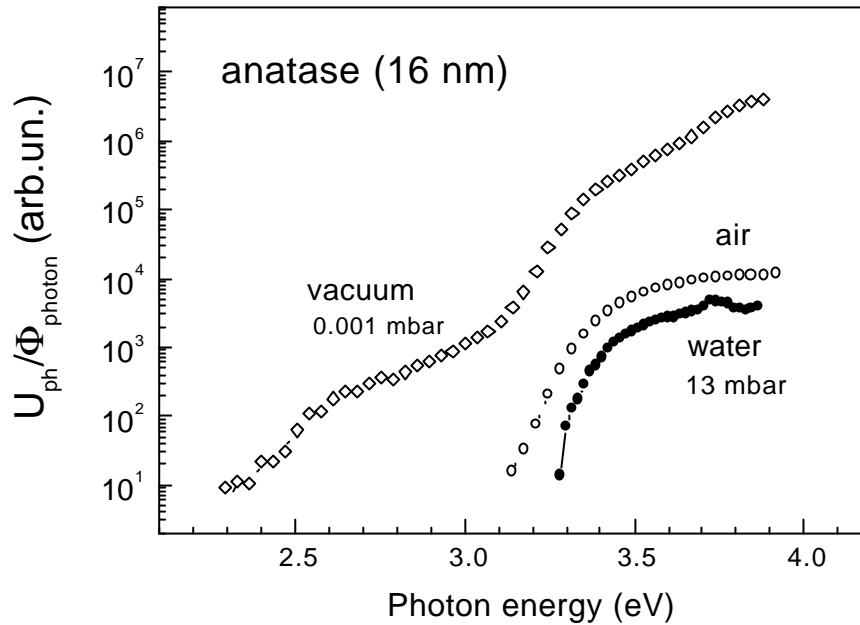


FIG. 6.9: Spectra of the photovoltage amplitude normalized to the photon flux in a semi-log scale for porous TiO₂ layers of anatase (16 nm) in air, vacuum (0.001 mbar) or water (13 mbar) ambiances.

The amplitude of the PV is slightly larger in latter case, what can be explained by the larger partial pressure of water vapors in the used experimental condition (13 mbar) in comparison to the content of water in room air ambience. Therefore, the adsorbed water at the surface of nanoporous TiO₂ screens the surface states, which are, probably, created by oxygen vacancies.

However, the PV spectra in vacuum prior to the water adsorption and after desorption of the adsorbed water are not equivalent. This shows the chemical nature of the interaction of the nanoporous TiO₂ surface and water. Chemical adsorption of water molecules on the surface of TiO₂ was also shown by thermal effusion measurements. Desorption of water at 393 K and OH group at 623 - 673 K was observed¹²¹ from the crystalline rutile surface and from the nanoporous anatase surface.⁵⁷ Dissociation of water under UV illumination¹³⁷ should be also discussed in this case. The discussed changes can be removed only by thermal annealing of the nanoporous TiO₂ in air at temperatures higher than 400 °C. Additionally, the shape and amplitude of the PV spectra as well as the time and amplitude of the PV transients slightly differs after different

annealing procedures. The humidity of the ambient air during the annealing procedure (or cooling) should be taken into account.

6.5 Transient photovoltage in nanoporous TiO₂ with gap states

Photovoltage transients for nanoporous TiO₂ layers of rutile (60 nm), anatase (16 nm) and anatase (6 nm) in vacuum ($p = 0.001$ mbar), oxygen ($p = 1000$ mbar) or water ($p = 14$ mbar) ambiances are shown in Figure 6.10. The excitation of excess carriers of charge is performed with $h\nu > E_G$ ($h\nu = 3.7$ eV). The PV transients of all samples in vacuum show pronounced shoulders at shorter times ($\leq 10^{-7}$ s for rutile and $\leq 10^{-6}$ s for anatase) which exactly coincide with the PV increase in the as prepared samples (compare corresponding curves in Fig.6.2 and Fig.6.10). It means that the PV increase in the sub-microsecond scale is not sensitive to the formation of surface traps by changing the ambience and is caused by charge separation within one nanoparticle. At longer times, the behavior of the PV transients in vacuum changes dramatically in comparison to that in air. The time of the PV maximum of the stored in vacuum samples increases by about 3 orders of magnitude in comparison to that of the as prepared samples in air independent of the size of nanoparticles. Whereas, an increase of the PV amplitude U_{PV}^{max} is only 2 times for rutile (60 nm), and 3.5 times for anatase (16 nm), the essential difference of about 300 times for anatase (6 nm) shows the role of the larger surface area for the PV in the nanoparticles of smaller size. The retarded increase of the PV at longer times is caused by the inter-particle transport. An increase of the PV at the expense of the increase of the excess carrier concentration for a fixed distance of a nanoparticle size between separated charge is unlikely, while it implements the large dispersion of the charge carrier mobility (range of mobility should be comparable with the time range of the PV increase – 4 - 5 orders of magnitude) inside the nanoparticle.

As was shown by spectral PV measurements, the adsorption of water leads to the disappearance of the sub-band gap tail in nanoporous TiO₂. Similar PV transients are observed for the as prepared samples and for the sample after adsorption of water (and stored in vacuum prior to absorption). The amplitude of the PV decreases and the time of the PV maximum becomes shorter with water adsorption. A comparison of the PV amplitude for as prepared and after water adsorption anatase (16 nm sample), for example, shows the difference in the amplitudes of 7 mV

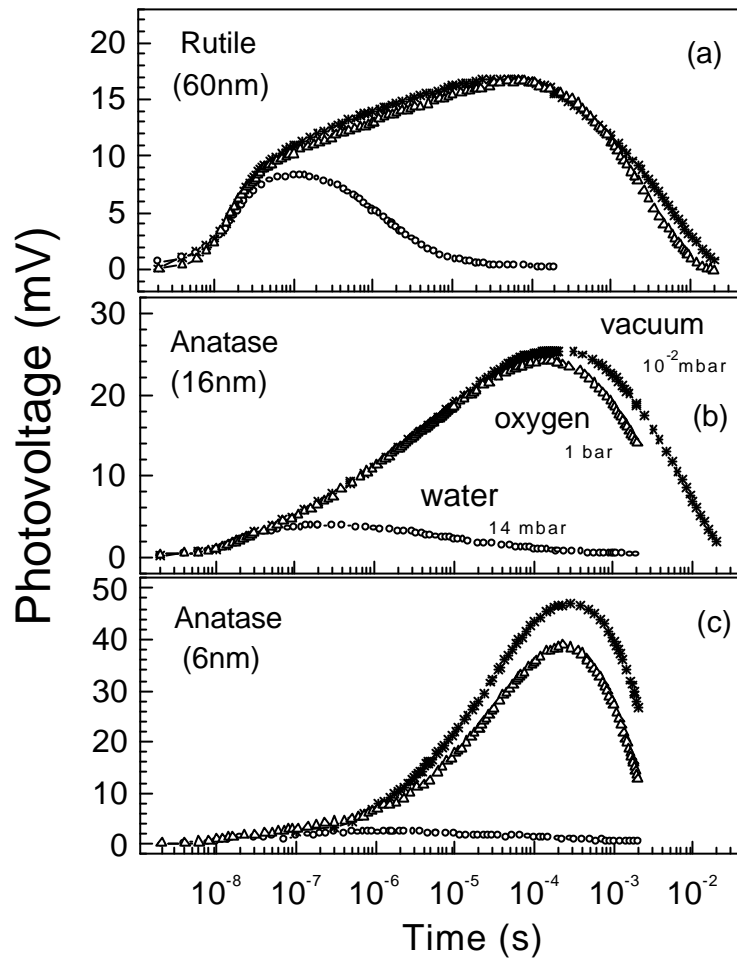


FIG. 6.10: Photovoltage transients for nanoporous TiO₂ layers of rutile (60 nm) (a), anatase (16 nm) (b) and anatase (6 nm) (c) in vacuum ($p = 0.001$ mbar) (stars), oxygen ($p = 1000$ mbar, triangles) or water ($p = 14$ mbar, circles) ambiances.

and 4 mV, respectively. This difference in amplitudes as well as shorter time of the PV maximum explain the smaller value of the spectral PV for anatase (16 nm) in water vapors (Fig.6.9).

No essential change of the PV transient for the rutile is observed after adsorption of oxygen. The amplitude of the PV becomes smaller and the time of the PV maximum becomes shorter for anatase in oxygen ambience. This difference becomes larger for smaller nanoparticle size. This supports the idea that not only water desorption but also creation of oxygen vacancies take place during the storage of sample in the vacuum. However, the adsorbed at room temperature oxygen is not able to create the chemical bonds with Ti atoms and higher temperatures (for, example, during the annealing procedure) are necessary to complete the lattice stoichiometry.

The PV transients of nanoporous TiO₂ in water and vacuum coincide as well as in air and vacuum at shorter times. But the range of the coincidence is shorter in the first case with a larger amount of water on the nanoparticle surface. The screening of the PV by the orientation of the dipole of water molecules and displacement of water radicals (H⁺, OH⁻) in the electric field of the separated excess charge carriers takes place for the cases of air or water ambiances. An increase of the PV due to the inter-particle transport is not screened by water in vacuum due to the deficiency of the water radicals in this atmosphere. The reason for the PV decay in vacuum will be discussed later.

6.6 Nature of the PV maximum in nanoporous TiO₂

The time of the PV maximum can be correlated with the conductivity of the nanoporous TiO₂ in different media. Impedance spectra of nanoporous TiO₂ (anatase (16nm)) in air (a), vacuum ($p = 1.2$ mbar) (b) or water ($p = 5.5$ mbar) (a) atmospheres are shown in Figure 6.11. The bias voltage of 0 V and alternative δU of 50 mV are used in the frequency range of 100 mHz – 1 MHz. Graphite and SnO₂:F contacts are used in the “sandwich” geometry with area of 0.1 cm² and sample thickness of 5 μ m. For the equivalent circuit which consists of the parallel connection of resistor and capacitor, the intersection of the semi-

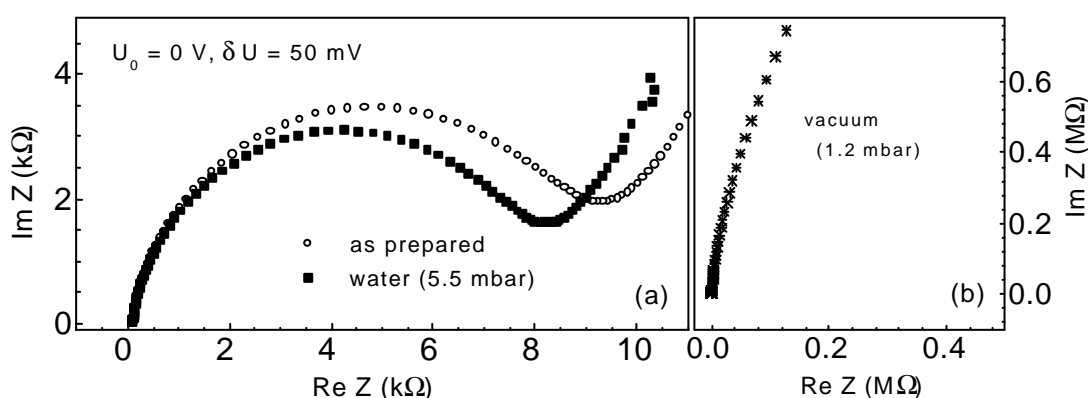


FIG. 6.11: Impedance spectra of nanoporous TiO₂ (anatase (16nm)) in air (a), vacuum ($p = 1.2$ mbar) (b) or water ($p = 5.5$ mbar) (a) atmospheres. The bias voltage of 0 V and alternative δU of 50 mV are used in frequency range of 100 mHz – 1 MHz.

arc with abscise axis of Cole-Cole plot produces the conductivity (σ) of nanoporous TiO₂.¹³⁸ The obtained value of σ in air of $6 \cdot 10^{-7} \Omega^{-1} \text{ cm}^{-1}$ produces the Maxwell relaxation time $t_M = 1.5 \mu\text{s}$ which is in good agreement with the time of the PV maximum $t_{max} = 1.1 \mu\text{s}$. The dielectric constant of nanoporous TiO₂ was taken as $\epsilon = 9$.¹⁹ A decrease of the conductivity was observed for the sample stored in vacuum (Fig.6.11(b)). The value of σ is out of the range of measurements in this case and can be only roughly estimated as $\sigma < 2.5 \cdot 10^{-9} \Omega^{-1} \text{ cm}^{-1}$. The respective value of the Maxwell relaxation time increases above 0.4 ms what is close to $t_{max} = 0.3 \text{ ms}$ in vacuum (Fig.6.10b). As remark, the conductivity of anatase (16 nm) obtained from the current-voltage measurements also decreases by 2 - 3 orders of magnitude after keeping the sample in vacuum. Water vapors shift the conductivity toward the larger values (Fig.6.11a). This tendency correlates with the shift of t_{max} toward the shorter times. The direct comparison of the t_M and t_{max} in water is difficult while the increased dielectric constant of the nanoporous TiO₂ covered by water should be considered.

The reaching of the back contact by excess charge carriers was discussed in the thin films of low conductivity materials as a possible reason for the maximum of the diffusion PV signal. The time of the PV maximum in air did not increase with increasing thickness of the nanoporous TiO₂ layers from 0.5 to 4 μm . The shapes of PV transients were also independent on the used substrates (SnO₂:F, p⁺-Si, ITO in the usual case of illumination from the nanoporous TiO₂ (front) side. As remark, the PV transients showed two negative extrema in the case of illumination through the semitransparent SnO₂:F back electrode (see Fig.1.3). The first extremum at about 10 ns was related to separation of charge at the nanoporous TiO₂/SnO₂:F interface (injection of excess electrons from nanoporous TiO₂ into SnO₂:F while the second one (in the μs range) belonged to the diffusion PV. The diffusion length of electrons is much smaller than 1 μm , the excess charge carriers do not reach the back contact in nanoporous TiO₂.

The screening of the separated charge by water determines the time of the PV maximum in nanoporous TiO₂ in wet atmosphere.

The PV transients do not decay purely by exponent or logarithmic law. A life time of charge carriers could be introduced for an exponential decay while the recombination of spatially separated charge could be used to describe a logarithmic decay.³⁹ Therefore, one we can describe the relaxation of the diffusion PV after Maxwell relaxation time is

reached by recombination of spatially separated charge carriers with taking into account the decrease of the separation distance in transport process.

6.7 Conclusion of Chapter 6

The photovoltage in nanoporous TiO₂ is formed by the diffusion of excess electrons and holes with different diffusion coefficients under illumination with a photon energy above the band gap. This mechanism of the PV formation (diffusion PV concept) is typical for materials with a huge Maxwell relaxation time as porous semiconductors and dielectrics, semiconducting polymers or metal oxides. The concept of the diffusion photovoltage has been used to study the fundamental properties of optical absorption and transport of excess carriers of charge in porous TiO₂. The photovoltage transients are strongly retarded in time with respect to the exciting laser pulse. The diffusion coefficient is larger for electrons than for holes independent of the phase (rutile, anatase) and size of the TiO₂ nanoparticles. The PV spectra coincide with the absorption coefficient of light around the band gap of anatase (16 nm). No PV signal was observed below the band gap for as prepared nanoporous TiO₂ and the losses of transmittance in this spectral range were attributed to Rayleigh scattering.

The creation of extended sub-band gap tails was observed in nanoporous TiO₂ stored in vacuum. The diffusion of excess holes has been observed for TiO₂ in the case when under vacuum storage the electron trap states are preferentially created and electrons are excited from the valence band into the localized electron trap states by illumination with a photon energy below E_G . The change of the PV sign from negative to positive around the mobility gap shows that despite of the electron trap generation the diffusion coefficient of electrons is still larger than the diffusion coefficient of holes under excitation of excess charge carriers with photon energy above the band gap. The retardation of the PV transients in time with respect to the exciting laser pulse becomes more pronounced with decreasing size of the interconnected TiO₂ nanoparticles and generation of defect states in vacuum.

The PV transients as well as the PV spectra are quite similar for as prepared nanoporous TiO₂ and for nanoporous TiO₂ after absorption of water. The PV transients become shorter in comparison to the ones in vacuum, screening by dipole water molecules and dissociated ions is

responsible for the decay of the PV in air and water ambiances. The time of the PV maximum correlates with the value of Maxwell relaxation time, which was measured by impedance spectroscopy measurements. The extended sub-band gap tails which appeared under storage of the samples in vacuum disappear after water absorption. Removal of water by vacuum leads to the further increase of the PV due to inter-particle charge carrier separation till the recombination decreases the concentrations of excess charge carriers.

Our results demonstrate the importance of the concept of diffusion photovoltage for the investigation of electronic states and carrier transport in nanocrystalline and porous semiconductors.

Summary

The mechanisms of a spatial separation of light induced charge carriers in nanoscale materials were studied in this work. Several nanoscale materials (porous Si, PPV, ultrathin TiO₂ (Cu₂O, ZnO) layers and nanoporous TiO₂) which have a size of basic units in the nanometer range were used for the demonstration of different mechanisms of the PV formation.

Separation of light induced charge carriers takes place in the electric field of the surface SCR in mesoporous Si of low porosity. The surface potential and the built-in electric field decrease with increasing porosity. The free charge carrier concentration is estimated as $1.6 \cdot 10^{17} \text{ cm}^{-3}$ in mesoporous Si from the shift of the intensity dependence of the PV or by the free carrier absorption measurements. Comparing to the typical PV transients in crystalline p-type Si, an additional retarded component of the same negative sign appears in the PV transients in mesoporous Si. The inter-particle separation of excess charge carriers in the material with smaller intrinsic carrier concentration is responsible for the further increase of the PV. The surface potential and the charge carrier concentration changes in porous Si with time due to the native or thermal oxidation. The SiO₂ bonds introduce acceptor - like electronic states on the surface of porous Si, trapping of electrons on the surface states of geometrical

surface changes the downward band bending to the upward. The decrease of the electric field of the surface SCR and the decrease of the size of nanoparticles with increasing porosity leads to the retardation of the charge carrier separation. The kinetics of the PV retardation is independent on the H-terminated or oxidized porous Si surface and depends on the size of nanoparticles and on the surface morphology. The potential difference between the surface and the bulk can be neglected in nanoporous Si of large porosity. The gradients of excess charge carrier concentration under light absorption lead to the PV formation. The PV appears due to the separation of excess electrons and holes in diffusion process with different diffusion coefficients. The PV transients are retarded in time and characterized by a maximum in this case. The time of peak of the PV transients coincides with the Maxwell (dielectric) relaxation time. This opens new opportunities to the contactless electrical characterization of porous semiconductors and its application.

The Maxwell relaxation time is huge in organic polymer PPV and compensation of the diffusion fluxes by drift (internal electric field between separated electrons and holes) is not possible before the Maxwell relaxation time is reached. The shapes of the PV transients in thick PPV layers are in good agreement with the typical simulated shape of the PV transient obtained from the diffusion PV model. The peak time of the PV depends on the thickness of the layers at a given intensity of illumination and points to the diffusion of charge carriers over the thickness of the PPV layers. The estimated values of diffusion coefficients of holes and electrons are of the order of 10^{-6} cm^2/s and 10^{-7} .. 10^{-8} cm^2/s , respectively. The diffusion coefficient of holes increases with increasing illumination intensity. This can be related to the filling of bandgap states by excess charge carriers in the material with dispersive transport. The diffusion PV is thermally activated with activation energy E_A for the amplitude of the PV amplitude of 0.42 eV. The diffusion PV method is a powerful tool for the investigation of charge carriers diffusion in materials with large Maxwell relaxation time.

The separation of excess charge carriers in nanoscale materials is possible over the nanometer scale and on the macroscopic range. The much insight into the details of electronic state distribution and its role for intra-particle transport can be obtained by considering the ultrathin

metal oxide layers as a model of a nanoparticle. Photovoltage signals were observed at ultrathin metal oxide (TiO_2 , Cu_2O , ZnO)/metal structures. The PV is shown to be a general phenomenon for ultrathin metal oxides. The sign, the spectral behavior and the time - dependent relaxation of the PV are determined by the nature of the traps in the metal oxide layers. The time of formation of the PV signal is comparable with the duration of the laser pulse in the ultrathin anodic TiO_2 layers which gives the upper estimation for the mobility of electrons $\mu_n > 4 \cdot 10^{-3} \text{ cm}^2/\text{Vs}$. After illumination with a photon energy larger than the band gap, the PV signal caused by injection of excess electrons into the metal substrate and by preferential trapping of excess holes inside the TiO_2 layer. At lower temperatures, the decay of the PV is determined by the overlap of the wave functions for electrons and holes resulting in the recombination of spatially separated excess carriers due to tunneling. At higher temperatures, thermal emission accelerates the relaxation of the PV signal. The Bohr radius of trapped holes, the tail of the exponential approximation of electronic states distribution above the valence band, the density of states at the valence band edge were obtained for TiO_2 layers by using the proposed model of trap limited PV.

The concept of the diffusion photovoltage has been used to study the fundamental properties of optical absorption and transport of excess carriers of charge in porous TiO_2 . The diffusion coefficient is larger for electrons than for holes independent and depends on the crystalline phase and size of nanoparticles in the nanoporous TiO_2 . The PV spectra coincide with the absorption coefficient of light around the band gap of anatase. No PV signal was observed below the band gap for as prepared nanoporous TiO_2 and the losses of transmittance in this spectral range were attributed to Rayleigh scattering. The creation of extended sub-band gap tails was observed in nanoporous TiO_2 stored in vacuum. The diffusion of excess holes has been observed for TiO_2 in the case of sub-band gap illumination when under vacuum storage the electron trap states are preferentially created and electrons are excited from the valence band into the localized electron trap. Despite of the electron trap generation by storage in vacuum, the diffusion coefficient of electrons is still larger than the diffusion coefficient of holes under excitation of excess charge carriers with photon energy above the band gap. The retardation of the PV transients in time with

respect to the exciting laser pulse becomes more pronounced with decreasing size of the interconnected TiO₂ nanoparticles and generation of defect states in vacuum. The maximum of the PV transient in wet atmosphere is determined by the dipoles of water molecules and dissociated ions which screen the electric field between separated charge carriers. The time of the PV maximum correlates with the Maxwell relaxation time for the network of the porous material covered by a water. The sub-band gap tails which appeared under storage of the samples in vacuum disappear after water absorption. Removal of water by vacuum leads to the further increase of the PV due to the inter-particle charge carrier separation till the recombination decreases the concentrations of excess charge carriers.

Our results demonstrate the importance of the concepts of diffusion and trap-limited photovoltage for the investigation of electronic states in nanoporous semiconductors and in ultrathin layers as metal oxides or organic molecules at metal surfaces.

Appendix A

During the simulation of the PV transients an integration appears:

$$U_{pv}(t) = \frac{e}{\epsilon \epsilon_0} \int_0^d dx \int_0^x p_0(y) \exp\left(-\frac{t}{\tau} \exp\left(-\frac{2y}{a}\right)\right) dy \quad (\text{A.1})$$

where y, t are the spatial co-ordinate directed from the free surface toward the interface and time, respectively. Zero point of y is taken at the free surface of the layer and

$$p_0(y) = \begin{cases} p_0, & 0 < y < d \\ 0, & y > d \end{cases} \quad (\text{A.2})$$

Direct analytical integration of this expression is not possible, while the double exponential function appears as integrand:

$$P(y, t) = p_0(y) \exp\left(-\frac{t}{\tau} \exp\left(-\frac{2y}{a}\right)\right) \quad (\text{A.3})$$

Despite of the numerical calculation of (A.1) we resort to the help of the „sharp-front approximation“ which elucidates the physical picture and was numerously discussed before.³⁸ The shape of the charge front $P(y, t)$ for the time moments $t_1 < t_2 < t_3$ is schematically shown in Fig.A.1 (the exact numerical simulation can be found elsewhere³⁸). The receding charge front becomes sharp after times of several τ . At times t all carriers of lifetime $t + \tau$ are assumed to have recombined. Thus the front is at y_0 , where $\tau \exp(-2(x_0 - d)/a) = t + \tau$, and

$$x_0(t) = d - a/2 \ln(1 + t/\tau) \quad (\text{A.4})$$

and the integral in (A.1) can be changed to

$$\int_0^x p_0(y) \exp\left(-\frac{t}{\tau} \exp\left(-\frac{2y}{a}\right)\right) dy = \begin{cases} p_0 \times x, & 0 \leq x \leq x_0 = d - \frac{a}{2} \ln\left(1 + \frac{t}{\tau}\right) \\ p_0 \times x_0, & 0 \leq x \leq d \end{cases} \quad (\text{A.5})$$

This approximation is valid for times $t \gg \tau$.

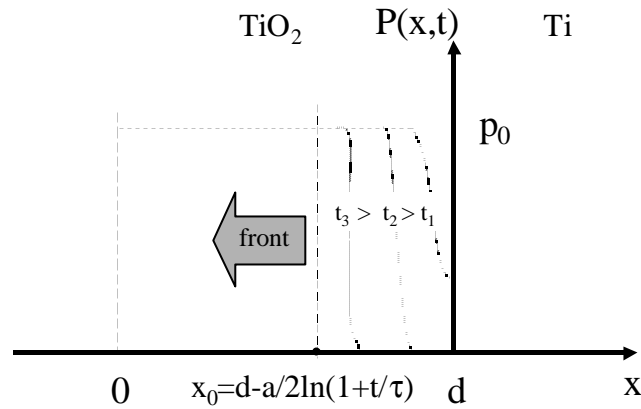


FIG. A.1: Time evolution of the trapped hole concentration due to spatially dependent recombination, sharp - front approximation changes the “real” concentration profile (dot lines) to the vertical line (dash line) with $x_0 = d - a/2 \ln(1 + t/\tau)$ for times $t \gg \tau$

Therefore, the next integration should be taken for two different interval $0 < x < x_0$ and $0 < x < x_0$ with different integrands (A.5):

$$U_{pv}(t) = \frac{e}{e\epsilon_0} \left(\int_0^{x_0} p_0 \cdot x dx + \int_{x_0}^d p_0 \cdot x_0 dx \right) = \frac{ep_0}{e\epsilon_0} \left(\frac{x_0^2}{2} + x_0 \cdot (d - x_0) \right) = \frac{ep_0}{e\epsilon_0} x_0 \left(d - \frac{x_0}{2} \right) \quad (\text{A.6})$$

Taking into account (A.4), the PV transient is described by:

$$U_{pv}(t) = \frac{ep_0 d^2}{2e\epsilon_0} \left(1 - \left(\frac{a}{2d} \right)^2 \ln^2 \left(1 + \frac{t}{\tau} \right) \right) \quad (\text{A.7})$$

References:

- ¹ J.H. Burroughes, D.D.C. Bradley, A.R. Brown, R.N. Marks, K.Mackay, R.H. Friend, P.L. Burn, A.B. Holmes, *Nature* **347**, 539 (1990).
- ² B. O'Regan and M. Grätzel, *Nature* **353**, 737 (1991).
- ³ E. Lebedev, Th. Dittrich, V. Petrova-Koch, S. Karg, and W.Brütting, *Appl. Phys. Lett.* **71**, 2686 (1997).
- ⁴ M.K. Nazeeruddin, A. Kay, I. Rodicio, R. Humphry-Baber, E. Müller, P. Liska, N. Vlachopoulos, and M. Grätzel, *J. Am. Chem. Soc.* **115**, 6382 (1993).
- ⁵ K.K. Tiong, P.M. Amirtharaj, F.H. Pollak, D.E. Aspnes, *Appl. Phys. Lett.* **44**, 122 (1984).
- ⁶ Th. Dittrich, E.A. Lebedev, J. Weidmann, *Phys. Stat. Sol. (a)* **165**, R5 (1998).
- ⁷ E. A. Lebedev, E. A. Smorgonskaya, G. Polisski, *Phys. Rev. B* **57**, 14607 (1998).
- ⁸ L.E. Brus, *J. Chem. Phys.* **80**, 4403 (1984).
- ⁹ L. Kronik, Y. Shapira, *Surf. Sci. Rep.* **37**, 1 (1999).
- ¹⁰ E.O. Johnson, *Phys. Rev.* **111**, 153 (1958).
- ¹¹ E.O. Johnson, *J. Appl. Phys.* **28**, 1349 (1957).
- ¹² A. Goodman, *J. Appl. Phys.* **32**, 2550 (1961).
- ¹³ C.L.Balestra, J.Lagowski, and H.C.Gatos, *Surf. Sci.* **26**, 317 (1971).
- ¹⁴ J.Lagowski, C.L.Balestra and H.C.Gatos, *Surf. Sci.* **27**, 547 (1971).
- ¹⁵ J.Lagowski, C.L.Balestra and H.C.Gatos, *Surf. Sci.* **29**, 203 (1972).
- ¹⁶ J.Lagowski, and H.C. Gatos, *Surf. Sci.* **38**, 252 (1973).
- ¹⁷ A.Morawski, R.Banisch, and J.Lagovski, *Surf. Sci* **69**, 444 (1977).
- ¹⁸ M.Ben-Chorin in *Properties of Porous Silicon*, edited by L.Canham (INSPEC, London, 1997) p.165.
- ¹⁹ Th. Dittrich, J. Weidmann, F. Koch, I. Uhlendorf, and I. Lauermann, *Appl. Phys. Lett.* **75**, 3980 (1999).
- ²⁰ C.G.B. Garrett and W.H. Brattain, *Phys. Rev.* **99**, 376 (1955)
- ²¹ O.B.Aphek, L.Kronik, M.Leibovitch, Y.Shapira, *Surf. Sci.* **409**, 485 (1998).
- ²² R.S.Nakhmanson, *Solid State Electron.* **18**, 617 (1975).
- ²³ C.Munakata, *Jpn. J. Appl. Phys.* **27**, 759 (1988).

-
- ²⁴ K. Heilig, Surf.Sci **44**, 421 (1974).
- ²⁵ A.R. Moore and Hong-Sheng Lin, J.Appl.Phys. **61**, 4816 (1987).
- ²⁶ L. Szaro, Appl. Phys. A **29**, 201 (1982).
- ²⁷ C.L.Balestra, J.Lagowski, H.C.Gatos, Surf.Sci. **64**, 457 (1977).
- ²⁸ K.G.Germanova, L.L.Konstantinov, V.L.Strashilov, Surf.Sci. **128**, 447 (1983).
- ²⁹ L.Szaro, Surf.Sci. **137**, 311 (1984).
- ³⁰ L.J.Brillson, Phys.Rev.B **18**, 2431 (1978).
- ³¹ L.J.Brillson, Surf.Sci.Rep. **2**, 195 (1982).
- ³² Th.Dittrich, P.K.Kashkarov, E.A.Konstantinova, V.Yu.Timoshenko, Thin Solid Films **255**, 74 (1995).
- ³³ V.Yu. Timoshenko, P.K.Kashkarov, A.B. Matweeva, E.A.Konstantinova, H.Flietner, Th.Dittrich, Thin Solid Films **276**, 216 (1996).
- ³⁴ R.A.Smith, *Semiconductors*, Cambridge University Press, London, 1959.
- ³⁵ J. Rappich and Th. Dittrich, *Electrochemical Passivation of Si and SiGe Surfaces* in Thin Film Handbook, edited by H.S.Nalva, Academic Press, 2000.
- ³⁶ R. Kohlrausch, Poggendorff's Ann. Phys. (Leipzig) **72**, 393 (1847).
- ³⁷ R.G. Palmer, D.L. Stein, E. Abrahams, and P.W.Anderson, Phys.Rev.Lett. **53**, 958 (1984).
- ³⁸ H.J.Queisser and D.E.Theodorou, Phys.Rev.B **33**, 4027 (1986).
- ³⁹ D.G. Thomas, J.J.Hopfield, and W.M.Augustyniak, Phys.Rev. **140**, 202 (1965).
- ⁴⁰ E.F. Schubert, A.Fischer, and K. Ploog, Phys.Rev.B **31**, 7937 (1985).
- ⁴¹ D.M.Hanson, R.Stockbauer, and T.E.Madey, Phys.Rev.B **24**, 5513 (1981).
- ⁴² W. Thomson, Phil. Mag. **46**, 82 (1898).
- ⁴³ F. Steinrisser and R.E.Hetrick, Surface Sci. **28**, 607 (1971).
- ⁴⁴ J. Clabes and M. Henzler, Phys. Rev. B **21**, 625 (1980).
- ⁴⁵ J.Merz, M.Hipp, J.Mlynek, O.Marti, Appl. Phys. Lett. **64**, 2338 (1994).
- ⁴⁶ R.J.Hamers, K.Markert, Phys. Rev. Lett. **64**, 1051 (1990).
- ⁴⁷ Y. Kuk, R.S.Becker, P.J.Silverman, G.P.kochanski, Phys.Rev.Lett. **65**, 456 (1990).

- ⁴⁸ A.Halimaoui, in *Properties of Porous Silicon*, edited by L.Canham (INSPEC, London, 1997) p.12.
- ⁴⁹ M.Herold, J.Gmeiner, and M.Schwoerer, *Acta Polym.* **47**, 436 (1996).
- ⁵⁰ J. Rappich, unpublished.
- ⁵¹ R.J.Blattner, C.A.Evans, and A.J.Braundmeier, *J.Vac.Sci.Technol.* **14**, 1132 (1977).
- ⁵² H. Tang, K. Prasad, R. Sanjines, P. E. Schmid, and F. Levy, *J. Appl. Phys.* **75**, 2042 (1994).
- ⁵³ S. P. S. Porto, P. A. Fleury, and T. C. Damen, *Phys. Rev.* **154**, 522 (1967).
- ⁵⁴ H. Berger, H. Tang, and F. Levy, *J. Crystal Growth* **130**, 108 (1993).
- ⁵⁵ J. Rappich, Dissertation A (Freie Universität Berlin, 1989).
- ⁵⁶ A. Guinier, "X-ray diffraction", W. H. Freeman and Company (San Francisco, London, 1963), chapter 5.
- ⁵⁷ J.Weidmann, Dissertation A, TU München, 1998.
- ⁵⁸ A.G.Cullis, in *Properties of Porous Silicon*, edited by L.Canham (INSPEC, London, 1997), p.99.
- ⁵⁹ A.L.Efros, B.I.Shklovskii "Electronic properties of Doped Semiconductors", Springer-Verlag, 1984, ch.13.
- ⁶⁰ M. Ben-Chorin, in "Properties of Porous Silicon" edited by L. Canham, INSPEC, London, 1997, p. 165.
- ⁶¹ V. Yu. Timoshenko, Th. Dittrich, V. Lysenko, M.G. Lisachenko, and F. Koch, *Phys.Rev.B* **64**, 085314 (2001) and references therein.
- ⁶² L.T. Canham in "Properties of Porous Silicon" edited by L. Canham, INSPEC, London, 1997, p. 83; R. Herino in "Properties of Porous Silicon" edited by L. Canham, INSPEC, London, 1997, p. 89; L.T. Canham in "Properties of Porous Silicon" edited by L. Canham, INSPEC, London, 1997, p. 106.
- ⁶³ J.-N. Chazalviel and F. Ozanam, in "Properties of Porous Silicon" edited by L. Canham, INSPEC, London, 1997, p. 59.
- ⁶⁴ M.I.J.Beale, J.D.Benjamin, M.J.Uren, N.G. Chew, A.G.Cullis, *J. Cryst. Growth* **73**, 622 (1985).
- ⁶⁵ L.A.Balagurov et al., *J. Appl.Phys.* **80**, 574 (1996).
- ⁶⁶ F.P. Romstad, E. Veje, *Phys.Rev.B* **55**, 5220 (1997).
- ⁶⁷ L. Kronik, N. Ashkenasy, M. Leibovitch, E. Fefer, Y. Shapira, S. Gorer, and G. Hodes, *J. Electrochem. Soc.* **145**, 1748 (1998).

-
- ⁶⁸ O.B. Aphek, L. Kronik, M. Leibovitch, Y. Shapira, *Sur.Sci.* **409**, 485 (1998).
- ⁶⁹ See, for example, K. Seeger, *Semiconductor Physics* (Springer-Verlag, Wien, 1973).
- ⁷⁰ K.H. Beckmann, *Surf. Sci.* **3**, 314 (1965).
- ⁷¹ P. Gupta, V. L. Colvin, and S.M. George, *Phys. Rev. B* **37**, 8234 (1988).
- ⁷² P.B.Harwood, and G.P.Thomas, in *Materials Issues in Silicon Integrated Circuit Processing*, Vol.71 of *Materials Research Society Symposium Proceedings*, edited by M. Wittmer, J. Stimmell, and M. Strathman (Materials Research Society, Pittsburg, 1986).
- ⁷³ G.Lucovsky, P.D.Richard, D.V.Tsu, and R.J. Markunas, *J. Vac. Sci. Technol.* **4**, 681 (1986).
- ⁷⁴ J. C. Knights, R.A.Street, and G.Lucovsky, *J.Non-Cryst.Solids* **35/36**, 279 (1980).
- ⁷⁵ G. Lucovsky, J.Yang, S.S.Chao, J.E.Tyler, and W. Czubytyj, *Phys.Rev. B* **28**, 3225 (1983).
- ⁷⁶ W. Theiß, *Thin Solid Films* **276**, 7 (1996).
- ⁷⁷ M. Niwano, J. Kageyama, K. Kurita, K. Kinashi, I. Takahashi, and N. Miyamoto, *J. Appl. Phys.* **76**, 2157 (1994).
- ⁷⁸ R.A.Nyquist, and R.O.Kagel, *Infrared Spectra of Inorganic Compounds*, Academic Press, New York, 1971;
G.M. Begun and A.C. Rutenberg, *Inorg. Chem.* **6**, 2212 (1967);
R.B. Badachhape, G. Hunter, L.D. McCory and J.L. Margrave, *Inorg. Chem.* **5**, 929 (1966).
- ⁷⁹ J. A. Schmidt and F. A. Rubinelli, *J. Appl. Phys.* **83**, 339 (1998) and references therein.
- ⁸⁰ R. Schwarz, F. Wang, M. Ben-Chorin, S. Grebner, A. Nikolov, F. Koch, *Thin Solid Films* **255**, 23 (1995).
- ⁸¹ G. Bomchil, A. Halimaoui, and R. Herino, *Appl. Surf. Sci.* **41/42**, 604 (1989).
- ⁸² E. Yablonovitch, D. L. Allara, C.C.Tsang, T. Gmitter, T.B. Bright, *Phys. Rev. Lett.* **57**, 249 (1991).
- ⁸³ S. M. Prokes and W. E. Carlos, *J.Appl.Phys.* **78**,2671 (1995).
- ⁸⁴ L. Burstein, Y. Shapira, J. Partee, J. Shinar, Y. Lubianiker, I. Balberg, *Phys. Rev. B* **55**, R1930 (1997).
- ⁸⁵ U. Neuwald, A. Feltz, U. Memmert, and R.J. Behm, *J. Appl. Phys.* **78**, 4131 (1995)

- ⁸⁶ H.P.Maruska, F.Namavar, and N.M.Kalhoran, *Appl.Phys.Lett.* **61**, 1338 (1992);
V. Pacebutas, A. Krotkus, I. Simkiene, and R. Viselga, *J. Appl. Phys.* **77**, 2501 (1995).
- ⁸⁷ M. Ben-Chorin, F. Möller, F. Koch, *Phys.Rev. B* **49**, 2981 (1994).
- ⁸⁸ D. Gagnon, J. D. Capistran, F.E. Karasz, R.W. Lenz, and S. Antoun, *Polymer* **28**, 567 (1987).
- ⁸⁹ A.J. Campbell, D.D.C. Bradley, and D.G.Lidzey, *J. Appl. Phys.* **82**, 6326 (1997).
- ⁹⁰ P.W. M. Blom, M.J. M.de Jong, and J.J. M. Vleddaar, *Appl. Phys. Lett.* **68**, 3308 (1996).
- ⁹¹ A.J. Campbell, M.S. Weaver, D.G. Lidzey, and D.D.C. Bradley, *J. Appl. Phys.* **84**, 6737 (1998).
- ⁹² S. Karg, Dissertation A, Bayreuth (1995).
- ⁹³ G.Paasch, W. Rieß, S.Karg, M. Meier, and M. Schwoerer, *Synth.Met.* **67**, 177 (1994).
- ⁹⁴ M. Meier, S. Karg, K. Zuleeg, W. Brütting, and M. Schwoerer, *J. Appl. Phys.* **84**, 87 (1998).
- ⁹⁵ O. Gaudin, R. B. Jackman, T.-P. Nguyen and P. Le Rendu, *J. Appl. Phys.* **90**, 4196 (2001).
- ⁹⁶ N.F.Colaneri, D.D.C.Bradley, R.H.Friend, P.L.Burn, A.B.Holmes, and C.W.Spangler, *Phys.Rev.B.* **42**, 11670 (1990).
- ⁹⁷ J.Gmeiner, S.Karg, M.Meier, W.Riess, P.Strohriegl, and M. Schwoerer, *Acta Polymer.* **44**, 201 (1993).
- ⁹⁸ M. Meier, S. Karg, and W. Riess, *J.Appl.Phys.* **82**, 1961 (1997).
- ⁹⁹ M. Meier, S. Karg, and W. Riess, *J. Appl. Phys.* **83**, 5045 (1998).
- ¹⁰⁰ M.S. Weaver, Ph.D. thesis, University of Sheffield, U.K. (1997).
- ¹⁰¹ H.C. Gatos, J. Lagowski, *J. Vac. Sci. Technol.* **10**, 130 (1973).
- ¹⁰² O.Gaudin, R. B. Jackman, T.-P. Nguyen, P. Le Rendu, *J. Appl. Phys.* **90**, 4196 (2001).
- ¹⁰³ J. Scherbel, P.H. Nguyen, G. Paasch, W. Brütting, and M. Schwörer, *J. Appl. Phys.* **83**, 5045 (1998).
- ¹⁰⁴ R. Breckenridge, W. Hosler, *Phys. Rev.* **91**, 793 (1953)
- ¹⁰⁵ J. Nelson, S. Haque, D. Klug, J. Durrant, *Phys. Rev. B* **63**, 205321.
- ¹⁰⁶ R. Fleming, D. Lang, C. Jones, M. Steigerwald, D. Murphy, G. Alers, Y. Wong, R. van Dover, J. Kwo, A. Sergent, *J. Appl. Phys.* **88**, 850 (2000).

-
- ¹⁰⁷ W.Göpel and G. Reinhardt, in *Sensors Update*, Eds. H.Baltes, W.Göpel, and J.Hesse, (VCH, Weinheim, 1996), pp.47-119.
- ¹⁰⁸ L.Forro, O.Chauvet, D.Emin, and L.Zuppiroli, *J.Appl.Phys.* **75**, 633 (1994).
- ¹⁰⁹ see, for example, D. Eastman, J. Freeauf, *Phys. Rev. Lett.* **34**, 395 (1975)
- ¹¹⁰ V. Afanas'ev, M. Houssa, A. Stesmans, M. Heyns, *Appl. Phys. Lett.* **78**, 3073 (2001)
- ¹¹¹ H. Tang, F. Levy, H. Berger, and P. E. Schmidt, *Phys. Rev. B* **52**, 7771 (1995)
- ¹¹² A. Rakhshani, *J. Appl. Phys.* **69**, 2365 (1991).
- ¹¹³ V. Srikant, D. Clarke, *J. Appl. Phys.* **81**, 6357 (1997)
V. Srikant, D. Clarke, *J. Appl. Phys.* **83**, 5447 (1998)
- ¹¹⁴ V. Duzhko, V. Yu. Timoshenko, F. Koch and Th. Dittrich, *Phys. Rev. B* **64**, 075204 (2001).
- ¹¹⁵ see for example, Th. Dittrich, *phys. stat. sol. (a)* **182**, 447 (2000) and refs. therein.
- ¹¹⁶ R. Könenkamp, *Phys. Rev. B* **61**, 11 057 (2000).
- ¹¹⁷ B.L. Bonch-Bruevich, and S.G.Kalashnikov, *Phisika Poluprovodnikov*, Nauka, Moscow, 1977.
- ¹¹⁸ T.K.Däubler, I.Glowacki, U.Scherf, J.Ulanski, H.-H.Hörhold, D.Neher, *J.Appl.Phys.* **86**, 6915 (1999).
- ¹¹⁹ N. Serpone, R. Khairutdinov, "Application of Nanoparticles in the Photocatalytic Degradation of Water Pollutants" (Elsevier, Amsterdam, 1996), Vol. 103, p. 417.
- ¹²⁰ V.E. Henrich, *Rep. Prog. Phys.* **48**, 1481 (1985).
- ¹²¹ M.Anpo, T.Shima, S.Kodama, Y.Kubokawa, *J.Phys.Chem.* **91**, 4305 (1987).
- ¹²² V.Henrich, G. Dresselhaus, and H.J. Zeiger, *Sol.St.Com.* **24**, 623 (1977).
- ¹²³ S.P.Bates, G.Kresse, M.J.Gillan, *Surf. Sci.* **409**, 336 (1998).
- ¹²⁴ R.G.Breckenridge and W.Hosler, *Phys.Rev.* **91**, 793 (1953).
- ¹²⁵ E. Konstantinova, J. Weidmann, and Th. Dittrich, *J. of Porous Materials* **7**, 389 (2000).
- ¹²⁶ V.Kytin and Th.Dittrich, *phys.stat.sol. (a)* **185**, 461 (2001).
- ¹²⁷ V.Kytin, private communication.
- ¹²⁸ D. C. Cronmeyer, *Phys. Rev.* **87**, 876 (1952).

- ¹²⁹ H. Tang, F. Levy, H. Berger, and P. E. Schmid, *Phys. Rev. B* **52**, 7771 (1995).
- ¹³⁰ G. D. Cody, T. Tiedje, B. Abeles, B. Brooks, and Y. Goldstein, *Phys. Rev. Lett.* **47**, 1480 (1981).
- ¹³¹ this question has been discussed for anodic layers of TiO₂ by K. Leitner, J. W. Schultze, and U. Stimming, *J. Electrochem. Soc.: Electrochem. Science and Technology* **133**, 1561 (1986).
- ¹³² S. Zhang, Y. F. Zhu, and D. E. Brodie, *Thin Solid Films* **213**, 265 (1992).
- ¹³³ D. Sivuchin, *Obshchiy kurs phisiki: Optika*, Nauka, Moscow, 1980.
- ¹³⁴ S. Zerfoss, R. G. Stokes, and C. H. Moore, *J. Phys. Chem.* **16**, 1166 (1948).
- ¹³⁵ A. von Hippel, J. Kalnajs, and W. B. Westphal, *J. Phys. Chem. Solids* **23**, 779 (1962).
- ¹³⁶ R. L. Kurtz, R. Stockbauer, T. E. Madey, E. Roman, and J. L. de Segovia, *Surface Science* **218**, 178 (1989).
- ¹³⁷ A. Fujishima, K. Honda, *Nature* **238**, 37 (1972).
- ¹³⁸ J. R. Macdonald, *Impedance Spectroscopy*, John Wiley & Sons, New York, 1987.

Acknowledgements

First of all, I would like to acknowledge *Prof.Ph.D.F.Koch* for the possibility to make a Ph.D. at the Physics Department E16 of Technical University of Munich. Under his wise management which combined guidance, constant interest, and some degree of freedom throughout the course of my Ph.D., the work became effective and pleasant.

My hearty thanks for the guidance, many useful discussions, tremendous patience, and, finally, for the correction of the manuscript, to *Dr.Th.Dittrich*. His amazing organizational possibilities allowed to join people from different fields and make this work possible.

Special thanks for the useful discussions which clarified many ideas and for the shearing of a great experience with experimental methods and interpretation methodology to *Dr.V.Yu.Timoshenko* (Moscow Lomonosov University), *Dr. V.Kytin* (Moscow Lomonosov University), and *Prof. E.Lebedev* (Saint-Petersburg Ioffe Institute), who invaluable extended my mental outlook and physical education during the Ph.D. work. My thanks go also to *Dr.B.Kamenev* (Moscow Lomonosov University) for the support with programming and to *Prof.Y.Shapira* (Tel-Aviv University) for critical remarks concerning the PV in the metal oxides.

I would like to thank *Dr. Jörg Rappich* from Hahn-Meitner Institute (Berlin) for the preparation of anodic layers of TiO_2 and Raman measurements, *Dr. W.Britting*, and *Dr. J.Gmeiner* from Bayreuth University for the preparation of PPV samples, *I.Sieber* from Hahn-Meitner Institute (Berlin) for the help with SEM measurements and *H.Schneider* (XRD) (TUM) for the help with XRD measurements.

This work would be impossible without Technicians of E16: *Hans Märzcz, Johannes Seitz, Heinz Streit, Todor Canov, Ralf Filbry*. Thanks for their constant technical support and a great patience during the communication in “FremdSprache”.

My friendly thanks to all colleagues of our Department E16 (*Habil. Dr. D. Kovalev, Dr. J.Diener, Dr. H.-E.Porteanu, N.Künzner, E.Gross, O.Loginenko*) for a pleasant and friendly atmosphere in the department and to our secretary *L. Darabas* for the assistance in management of a never-ending paperwork.

This work was supported by Deutsche Forschungsgemeinschaft in the frame of project Di633/1-3.

Curriculum Vitae

- 9.04.1976** born in s.m.t. Yelanets´, Mykolayivs´ka obl., Ukraine
- 1983 - 1987** Ground school, Yelanets´, Ukraine
- 1987 - 1990** Secondary school, Yelanets´, Ukraine
- 1990 - 1993** Ukrainian physical - mathematical lyceum, attached to National Taras Shevchenko University, Kyiv, Ukraine
- 1993** diploma of secondary education, grade 105/105
- 1993 - 1997** undergraduate student at the Semiconductor Physics Department, Faculty of Radiophysics, National Taras Shevchenko University, Kyiv, Ukraine
- 1997** B. S. in Applied Physics (with honor, grade 4.98/5.00), BS diploma work: „*Magnetic p-n junction in Ge*“
- 1997 - 1999** pre-graduate student at the Semiconductor Physics Department, Radiophysics Faculty, National Taras Shevchenko University, Kyiv, Ukraine
- 1999** M. S. in Physics (with honor, grade 4.97/5.00), MS diploma work: „*Oscillations of extremely high density current in Silicon-on-Insulator structures*“
- 1999 - 2002** Ph.D. student, Semiconductor Physics, Department of Physics, Technical University of Munich, Munich, Germany
Ph. D. thesis: „*Photovoltage phenomena in nanoscale materials*“; supervised by Prof. F. Koch

List of publications in reviewed journals:

7. Th.Dittrich and V. Duzhko,
“Photovoltage in free-standing mesoporous silicon layers“
Phys.stat.sol. (a), to be published.
6. V. Duzhko, F.Koch and Th. Dittrich
“Transient photovoltage and dielectric relaxation time in porous Si“
J. Appl. Phys. **91**, xx (2002).
5. Th. Dittrich, V. Duzhko, F. Koch, V. Kytin, J. Rappich
“Trap limited photovoltage in ultrathin metal oxide layers“
Phys. Rev. B **65**, 155319 (2002).
4. V. Duzhko, V. Yu. Timoshenko, F. Koch and Th. Dittrich
“Photovoltage in nanocrystalline porous TiO₂“
Phys. Rev. B **64**, 075204, (2001).
3. V. Kytin, V. Duzhko, V. Yu. Timoshenko, J. Rappich and
Th.Dittrich
„Injection photovoltage in thin anodic TiO₂ layers“
Phys. stat. sol. (a) **185**, R1, (2001).
2. V. Duzhko, Th. Dittrich, B. Kamenev, V. Yu. Timoshenko,
W.Brütting
“Diffusion photovoltage in poly (p-phenylene vinylene)“
J. Appl. Phys. **89**, 4410 (2001).
1. V. Yu. Timoshenko, V. Duzhko, and Th. Dittrich
„Diffusion photovoltage in porous semiconductors and dielectrics“
Phys. stat. sol. (a) **182**, 227 (2000).

Conference participations:

5. Oral and poster presentations, Material Research Symposium, Boston, 26 - 30 November, 2001.
4. Poster presentation, DPG Fruehjahrstagung, Hamburg, 26 - 30 March, 2001.
3. Oral presentation, DPG Fruehjahrstagung, Regensburg, 27-31 March, 2000.
2. Poster presentation, NATO/EC ARWorkshop, Kyiv, Ukraine, 22-26 May, 2000.
1. Poster presentation, Porous Semiconductors - Science and Technology, Madrid, Spaine, 12 - 17 March, 2000.